POLITECNICO DI MILANO
PHYSICS DEPARTMENT
DOCTORAL PROGRAM IN PHYSICS

COLLECTIVE EXCITATIONS IN HIGH TEMPERATURE SUPERCONDUCTING CUPRATES STUDIED BY RESONANT INELASTIC SOFT X-RAY SCATTERING

Doctoral Dissertation of:
Greta Dellea

Supervisor and Tutor:
Prof. Giacomo Ghiringhelli

Chair of the Doctoral Program:
Prof. Paola Taroni

January 19, 2016 – XXVIII Cycle

Physics is what physicists do late at night.

Richard P. Feynman

Abstract

Since the discovery of high temperature superconductors (HTS), more than a quarter of century ago, increasing efforts have been devoted to the search of the basic mechanism leading to superconductivity, but a conclusive and generally agreed explanation is still missing. In this scenario, a better understanding of collective excitations in layered cuprates, either competing or coexisting with the superconducting state, has become a fundamental issue.

Cuprates are characterized by the presence of CuO_2 planes – Cu^{2+} ions alternated to O^{2-} ions – separated each other by blocking layers; much of the physics of cuprates takes place in these planes. The parent compounds have one hole per Cu site and the strong electron correlation, typical of transition-element oxides, leads to insulating behavior. These localized holes order antiferromagnetically (AF) and the resulting spin dynamics is well described in terms of spin wave, or magnon, excitations within the bidimensional spin ½ Heisenberg model. When the insulating parent compounds are doped, the additional dopant charges rapidly destroy the Néel ordering and trigger the superconducting transition in correspondence to a critical doping range. If the doping is further increased, the system reaches a non-superconducting metallic phase where low energy electronic excitations have Landau Fermi liquid-like properties.

A boost in the interest in collective spin excitation and their evolution with doping came from recent experimental results and theoretical calculations, suggesting a paring by exchange of magnetic excitations, in concomitance with the development of resonant inelastic x-ray scattering (RIXS) at Cu-L_3 edge, which has been proved to be the optimal technique to study magnetic, orbital and charge fluctuations in the CuO_2 planes.

RIXS in the soft x-ray regime is an energy loss spectroscopy, in which the incoming photons energy is tuned at an absorption edge. The signal enhancement at the resonance can be very large, making the measured inelastic signal strong enough to be detected. The choice of the absorption edge also provides chemical selectivity and stringent selection rules on the type of excited states created in the scattering process, mainly if the polarization of the photons is known and controlled. Finally, the sizable momentum carried by x-ray photons can be taken into account to measure the energy vs momentum dispersion relation of the excited states.

This thesis presents some of the results obtained with Cu-L_3 RIXS on superconducting and insulating cuprates during my activity in the group of Prof. G. Ghiringhelli and Prof. L. Braicovich at the Physics Department of Politecnico di Milano (Italy). The group has a well-established experience in synchrotron-based spectroscopies for the study of magnetic and electronic properties of transition-elements and rare-earth compounds. Recently they focused their activity on RIXS, contributing to the development of the technique, both from the point of view of science and instrumentation.

Starting from the experimental evidence that optimally doped high-T_c superconductors exhibit high-energy damped spin excitations (paramagnons) with dispersions and spectral weights closely similar to those of magnons in undoped cuprates, we extended our analysis to a large family of cuprates; spin excitations have been detected in a wide class of samples and dopings, from the well know bulk crystals and thin films, to more complex superconductors, obtained by superlattices and heterostructures, down to a few unit cells layers and nanopaterned structures, giving a further confirmation of the robustness of magnetic excitations and providing an ubiquitous ingredient for the superconductivity. We also used RIXS to measure the evolution of (para)magnons across the entire phase diagram of hole-doped cuprates, from the superconducting underdoped and optimally doped, to the non-superconducting highly overdoped samples. These results suggest a more complex explanation of the pairing mechanism, which could include the influence of the low-energy magnetic excitations, and other ordering phenomena.

Superconductivity could be achieved by doping with both holes and electrons. The e-doped region of the cuprates phase diagram has been less investigated so far, mainly due to technical limitations in sample growing and experimental techniques. Changing the sign of the doping carriers has strong implications for the shape of the corresponding phase diagram and some important physical proprieties, such as pseudogap, stripe order and maximum critical temperature (T_c), dramatically change. In that sense, the asymmetry between electron- and hole-doping in high-T_c cuprates is fundamental in understanding the processes at the basis of the superconducting transition. In this thesis we show RIXS spectra measured from the archetype e-doped $Nd_{2-x}Ce_xCuO_4$ (NCCO) crystal and from the more exotic $Sr_{1-x}La_xCuO_2/GdScO_3$ infinite layer cuprate heterostructure. Our data show a magnetic excitation hardening under e-doping in stark contrast with h-doping; this result is counterintuitive and interpreted in terms of a strongly itinerant character compared to the more localized spin dynamics found in h-doped cuprates.

It is also interesting to notice that both artificial h- and e-doped superconducting cuprates perfectly mimic the collective excitation behavior of the corresponding bulk crystals, envisaging the possibility to explore general properties of HTS physics on a broad range of conditions, by means of artificial compounds not constrained to the thermodynamic limitations governing chemical stability of bulk materials.

Our results suggest that any successful theory for HTS should require a detailed understanding not only of the magnetic excitation spectrum, but also of the combined effect of electron-phonon coupling and charge-order in the normal state from which superconductivity emerges. We found increasing general evidence that, in cuprates, spin excitations get coupled to both lattice modes and charge order. A better clarification of this three-actor scenario for the superconductivity pairing mechanisms will require further systematic use of high resolution resonant elastic and inelastic x-ray scattering.

All the results discussed so far have been acquired with two dedicated high resolution RIXS spectrometer, both designed and build by the group of Prof. G. Ghiringhelli and Prof. L. Braicovich: AXES (Advanced X-ray Emission Spectrometer) working since 1995 at the beamline ID08 of the European Synchrotron Radiation Facility (ESRF) and now dismissed, and SAXES (Super-AXES) which is the evolution of AXES, and has been installed in 2006 at the ADRESS beamline of the Swiss Light Source (SLS).

At present, the scientific output of soft-RIXS is reaching its limits due to technical limitations in terms of energy resolution, signal intensity, outgoing polariza-

tion analysis and sample orientation control. In order to overcome all these limitations, the new ERIXS (European-RIXS) instrument at the new ID32 beamline of the ESRF has been designed and commissioned and it is now ready for the first user experiments run.

The final part of my Ph.D. work has been mainly devoted to the commissioning and performances characterization of the new spectrometer, which now holds the world record of resolving power with a total instrumental resolution of 35 meV at Cu-L_3 edge (930 eV). This thesis reports a detailed instrumentation session, with preliminary experiments on antiferromagnetic and superconducting layered cuprates, and test measurements at different edges: Ni-L_3, Mn-L_3, Ti-L_3, Ce-M_5, Gd-M_5, Eu-M_5, extending the class of materials that can be investigated by RIXS, from the more studied cuprates, to a wide range of systems.

Contents

Introduction

Recent improvements in instrumentation and the development of new generation synchrotron radiation sources have established resonant inelastic x-ray scattering (RIXS hereafter) as the leading technique in the investigation of collective excitations in strongly correlated electron systems.

RIXS is a *photon in-photon out*, synchrotron-based spectroscopic technique well known since more than 40 years [1], but it has overcome a so called *Renaissance*, as defined by Kotani and Shin [2], only in the last decades, when it has been developed both in the soft and in the hard x-rays regime.

Photons having energies between 400 and 1000 eV are better suited for resonant x-ray spectroscopies, because this is the energy range in which the $L_{2,3}$ absorption edges of 3*d* transition-metals (3*d*TMs) are located. In this way it is possible to excite the dipole allowed $2p \rightarrow 3d$ transitions, which are strongly resonant and involve directly the 3*d* states, the most meaningful for the physical and chemical properties of materials.

When performed in the soft x-ray range, RIXS is thus ideal for the study of materials based on 3*d* transition-metals oxides, with a particular focus on high temperature superconducting (HTS) cuprates, where it has become a powerful alternative to more established techniques based on neutrons or low energy photons

for the study of low- and medium-energy excitations.

Cuprates are nowadays considered a hot topic in the fields of solid state physics and material science. During the last decades an increasing number of researchers investigated these systems in the search of the basic mechanism leading to high temperature superconductivity, but a clear explanation is still unknown. Even though the way to an extensive technological implementation might be long, experiments that explore the properties and the ordering phenomena that characterize the normal state form which superconductivity occurs are currently needed. In particular, understanding the basic physical mechanism of superconductivity in cuprates and the conditions under which it can be realized are of fundamental importance for any future application.

When studied with RIXS tuned at the Cu-L_3 absorption edge, cuprates give intense and richly featured spectra, allowing to contemporary access magnetic, orbital, charge and lattice excitation. In particular, thanks to the exceptionally large superexchange interaction of these systems ($J \sim 140$ meV for parent compounds), magnetic excitations do not require a sub-meV experimental resolution to be detected, while the Cu-L_3 resonance is so strong that RIXS cross sections allow to perform experiments on very small sample volumes (down to nanopatterned systems and single unit cell thin films), incompatible with inelastic neutron scattering (INS). Finally, the photon momentum available at Cu-L_3 is sufficiently large to cover almost completely the first Brillouin zone (BZ) in the two-dimensional reciprocal space of the CuO_2 square lattice.

All the reasons mentioned above, together with a strong interest in the subject *per se*, support our choice of cuprates as the perfect system in which exploring the new opportunities brought by soft-RIXS.

The unique RIXS features have indeed led to several important scientific results obtained over the last 15 years, using both the AXES (Advanced X-ray Emission Spectrometer), and the SAXES (Super-AXES) spectrometers. This initial success also boosted several new projects for high-resolution soft x-ray RIXS in numerous facilities worldwide, among them we cite the ERIXS (European-RIXS) spectrometer at the ESRF, which is at the moment the only already operative new generation RIXS instrument.

The main aim of this thesis is thus to describe the recent experimental progresses in soft x-rays RIXS studies of collective excitation in HTS cuprates. Some of the most interesting results obtained during the last three years are presented, including unpublished materials, and future trends allowed by the instrumentation development are anticipated.

In more details, the work presented in the following is divided in two main parts: (i) Chapters from 1 to 3 provide the required theoretical and instrumental background needed for the understanding of the experimental datasets; (ii) while Chapters from 4 to 6 present some of the insights gained in the last years by our group into the physics of cuprates by soft-RIXS measurements.

In Chapter 1 a brief overview to the properties of strongly correlated electron systems is offered, together with an historical introduction to the fascinating world of high temperature superconductivity. Copper oxides electronic states are shown, and the evolution of cuprates phase diagram with doping is discussed.

Chapter 2 is dedicated to a very general introduction to the RIXS scattering process, with special emphasis on all the characteristics that together make this technique unique. Excitations probed by RIXS are classified, with a particular focus on the energy range and samples families studied throughout the thesis. In the last section of the Chapter, the theoretical background required for understanding the RIXS cross-section is derived and discussed with the help of recent theoretical findings.

Chapter 3 provides an introductory description of the instrumental setup required for soft-RIXS, the layout of new ID32 beamline of the ESRF is shown as an example of a soft x-ray synchrotron beamline, and the main features of the new ERIXS spectrometer are introduced together with a comparison with the previous AXES and SAXES spectrometers. Data from ERIXS commissioning are presented in order to show the performances and potentialities of the new instrument. The final part of the Chapter is devoted to the description of a polarimetric device, that provides for the first time the possibility to detect the polarization state of the scattered beam in energy resolved soft x-ray scattering experiments. The effects of single photon counting (SPC) algorithm for the reconstruction of CCD detected images on the final RIXS experimental resolution are also briefly reviewed.

In Chapter 4, x-ray spectroscopy studies of hole-doped cuprates are shown, with focus on the magnetic excitations and their evolution with doping, from undoped samples up to the highly overdoped case. Recent experimental probe of the collective nature of the so called *paramagnons* are also discussed, together with the generalization of magnetic excitations to all the classes of hole-doped cuprates, from millimetric size single crystals, down to nanomentric samples, and in more exotic systems, such as superlattices and heterostructures.

Chapter 5 brings the attention form the hole- to the electron-doping region of the cuprates phase diagram. Differences and similarities in the evolution of charge

and magnetic excitations depending on the doping type are discussed by studying both archetype single crystals and more exotic cuprates-based samples. The substantial equivalence of the results provided from the two different classes of materials is stressed. In the second part of the Chapter, a direct comparison between electron- and hole-doping is also discussed for the simplest case of infinite layer cuprates.

Chapters 6 concludes the thesis summarizing recent results from charge and lattice excitations studies and suggesting a more complex explanation for superconductivity in cuprates, not only linked to magnetic excitations, as argued since a few years ago, but more likely related to an interplay between three or more different actors: spin, charge and lattice excitations.

Finally, in Conclusions and Outlook the most important achievements of the thesis are summarized together with ideas for new experiments complementing the present work and exploring the potentialities of the recent progresses in instrumentation.

Chapter 1

High temperature superconductivity in cuprates: an open question

Since their discovery in late 1986 [3], cuprates superconductors have attracted an increasing interest among the scientific community, boosted by both their unexpected physical properties and possible technological applications, allowed by their high critical temperature (T_c).

In this Chapter, we briefly provide an introductory overview to general aspects of high temperature superconductors, focusing on insulating and superconducting layered cuprates and their properties as strongly correlated electrons systems.

Our choice to investigate these systems was driven by both the scientific interest in the complex electronic structure of these materials, which is still to be completely understood, and the possibility to fruitfully exploit the potentialities of resonant inelastic x-ray scattering (RIXS).

The *K* edge of O and the $L_{2,3}$ edges of 3*d* transition-metal (TM) compounds lie in the soft x-ray energy range, thus RIXS in the soft x-ray regime is an extremely suitable technique for the investigation of cuprates, providing crucial information on collective excitations taking place in CuO_2 planes, which constitute the framework in which superconductivity emerges.

1.1 Strongly correlated electrons systems

Cuprates superconductors belong to the class of 3*d* transition-metal oxides and are classified as strongly correlated electron systems because of the unexpected physical properties that they display.

The expression *strongly correlated electrons systems* refers to those materials whose description in terms of one-electron theories fails. In such systems, electrons are deeply influenced by each other, and their collective motion is so strongly correlated that they cannot be described by models based on a single electron approach. These so-called mean-field theories are indeed based on the idea of an electron propagating in a periodic field generated by the atoms nuclei and an average Coulomb field due to the presence of the other electrons in the solid.

The failure of these theories in the description of some classes of materials was already pointed out by De Boer and Verwey in 1937 [4]. A good example of systems that cannot be described by mean-field theories is constituted by materials based on 3*d* transition-metal oxides: one-electron theory predicts a metallic behavior for many of them, but they actually are insulators with large band gaps. Ceramic high-temperature superconductors, based on CuO_2 layers, displaying an insulating antiferromagnetic phase at room temperature and a superconducting state below a certain critical temperature T_c, are certainly another famous example of systems in which the assumption that the electrons move in an average field created by the other electrons is not reliable.

In order to properly reconcile the complexity of strongly correlated electrons systems, such as cuprates, it is necessary to introduce many-body calculations. The main drawback of such calculations in solids is the difficulty in handling because of the large number of electrons involved. In order to overcome this problem, model Hamiltonians should be properly developed, taking into account the essential phenomena, while neglecting some of the interactions between the electrons. Among these model Hamiltonians, one of the simplest was proposed by Hubbard in 1963 [5]: it only deals with one band of electrons that only feel a Coulomb repulsion (U) when they occupy the same lattice site.

A detailed theoretical description of the origin of band gaps and the character of valence and conduction states in 3*d* transition-metal oxides is beyond the purpose of this introductory Chapter. For a discussion of the electronic structure of transition-metal oxides and their classification according to the well know Zaanen-Sawatzky-Allen scheme, we refer to Ref. [6].

1.2 High-T_c superconductors

The 30 years old story of high temperature superconductivity (HTS) started in late 1986 [3], when Bednorz and Müller discovered that cuprates present a superconducting transition at critical temperatures that could exceed the limits imposed by the BCS theory for traditional phonon-mediated superconductivity [7].

Since their finding, thousands of experiments and published results have been produced in the search of the basic mechanism governing high-T_c superconductivity. Although many progresses have been obtained in the understanding of these extremely complex systems, a conclusive explanation is still missing and possible scenarios are continuously evolving with the discovery of new experimental evidences and the development of new theoretical models.

Efforts were pushed not only by the intellectual interest in these systems, but also by the potential technological applications allowed by the high-T_c that exceeds the boiling temperature of liquid N_2. In Fig. 1.1 a summary of the critical temperatures of several superconducting compounds discovered during the last century is presented.

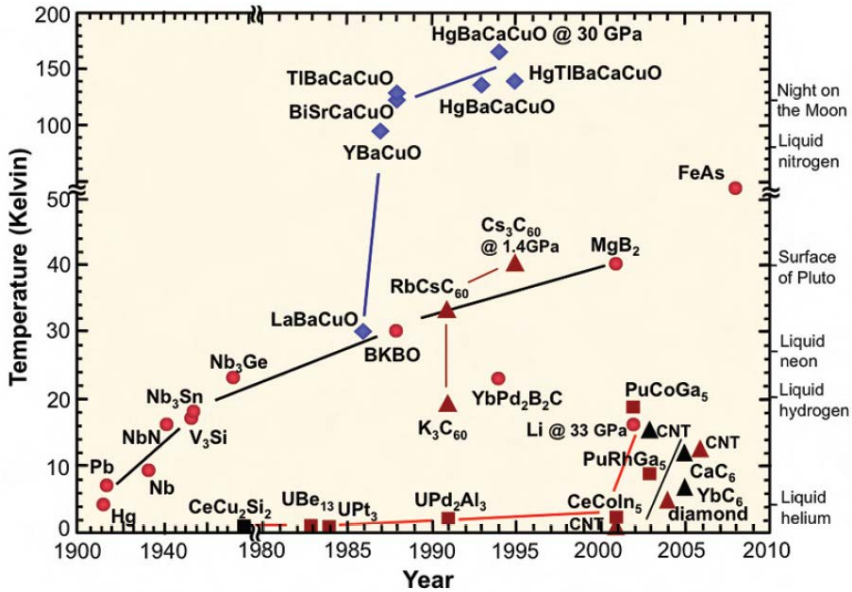

Fig. 1.1: Summary of the transition temperatures for several superconducting compounds. Fig. reproduced from Ref. [8].

Cuprates clearly represented a breakthrough in the physics of superconductivity with a maximum T_c of 138 K in the Hg-based compound $Hg_{0.2}Tl_{0.8}Ca_2Ba_2Cu_3O_{8+\delta}$ [9]. More recently, in 2006, high-temperature superconductivity has been found in a new family of layered iron-based compounds [10,11], but the record for the highest critical temperatures still belongs to cuprates.

1.3 Superconductivity in cuprates

The unicity of copper oxides superconductors is evident when comparing them with other 3*d* transition-element oxides: cuprates differs from a chemical, electronic and structural point of view.

From a direct comparison between cuprates and conducting TM oxides [12], two main differences are evident: (i) the character of the electronic bands involved in conductivity and (ii) the electronic configuration of the 3*d* TM element.

In most of the conducting TM oxides, electrons motion takes place in energy bands based on the 3*d* orbitals of the transition-element present in the compound. In cuprates instead, conductivity involves both Cu and O. The energy difference between oxygen and copper orbitals is indeed very small, providing a contribution from bands with oxygen character to the highest occupied electronic states.

The basis of every superconducting cuprate is constituted by the CuO_2 planes. The electronic configuration of the Cu^{2+} ions in these planes is $3d^9$, nine of the ten available *d* orbitals are filled. These orbitals are non-degenerate in energy and the splitting of the associated electronic states is given by the crystal field generated by the presence of the oxygen ligands surrounding each copper atom.

The geometrical coordination of ligands lowers the spherical symmetry of the isolated ion and removes the initial degeneracy of the *d* orbitals. In the CuO_2 planes, every Cu^{2+} ion has four in-plane near neighbors oxygens that form a square plaquette, this corresponds to the simplest configuration, called *infinite layer*. Adding one or two apical oxygens to this plaquette, it is possible to obtain Cu-O polyhedral with correspondingly pyramid or octahedron symmetry, where the Cu-O in-plane distance is usually shorter compared to the out-of-plane one.

A schematic representation of Cu *d* orbitals and oxygen ligands is shown in Fig. 1.2, for sake of clarity ligands are presented in an octahedral coordination, pyramid and infinite layer structure can be easily derived.

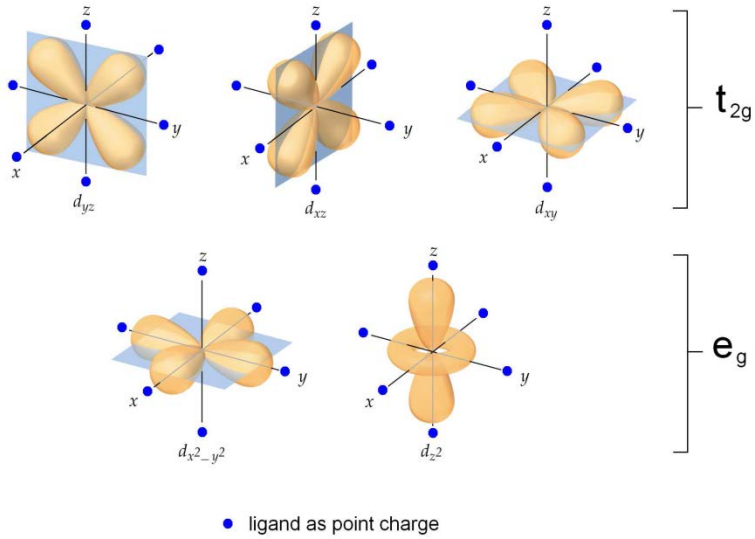

Fig. 1.2: Schematic representation of Cu *d* orbitals. Oxygen ligands are shown as point charge in an octahedral configuration. Fig. reproduced from Ref. [13].

The t_{2g} orbitals are the lowest in energy, because they are not directed towards oxygen ligands, and therefore they are completely filled. Due to the elongated shape of the Cu-O polyhedral, the e_g orbital pointing to the out-of-plane oxygens feels a lower repulsion from the ligands and it is filled as well. These results in a $3d^9$ electronic configuration with one unpaired electron and one hole in the d_{x2-y2} orbital, which points toward the in-plane oxygens. For this reason, it is common to describe the electronic states of cuprates in terms of the single $3d^9$ hole.

The standard one-electron picture for the electronic properties of solids would predict a metallic behavior for a compound with the outermost electron shells not completely filled, as in the electronic configuration described above; instead copper oxides are electrical insulators. The latter is due to the strongly correlated nature of electrons in cuprates, the addition of a second electron to the d_{x2-y2} orbital requires a significant amount of extra energy, given by the on-site Coulomb repulsion energy *U*, due to the electron already present, making the conduction process unfavorable.

Considering the magnetic properties, the insulating layer cuprates, that constitute the parent compounds of high-T_c superconductors, have one spin ½ for each Cu^{2+} ions in the CuO_2 planes. These spins order antiferromagnetically at low temperatures via super-exchange interaction, i.e. oxygen mediated exchange, and can be described in terms of a 2D Heisenberg antiferromagnet. The magnetic coupling

is extremely strong, with Néel ordering temperatures (T_N) of ~ 300 K and common super-exchange constants (J) of the order of ~ 140 meV.

Perturbations of this collective magnetic order have been widely studied in the last years, mainly by inelastic neutron scattering (INS) and, more recently, by resonant inelastic x-ray scattering (RIXS), as detailed discussed in the following Chapters.

These techniques are actually probing spin waves, namely magnons, which are eigenstates of the bidimensional antiferromagnetically ordered CuO_2 planes of layered cuprates, and can be described in terms of coherent collective magnetic excitations, which involve more than one site in the same CuO_2 plane. There can also be modes propagating perpendicularly to the CuO_2 planes, due to the weak (but finite) coupling among them. However, these out-of-plane magnons have attracted less interest in recent experimental studies, due to their weaker coupling.

The quasi-2D layered cuprates have indeed a strong bidimensional character; this allows probing the collective nature of magnetic excitations restricting the study to their 2D first Brillouin Zone (BZ). The corresponding direct and reciprocal 2D lattice units are described in Fig. 1.3.

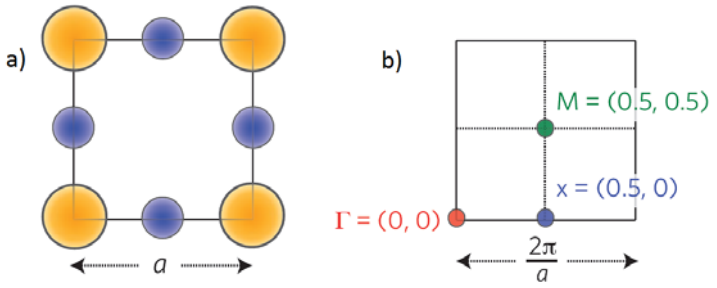

Fig. 1.3: (a) The basic structural unit of cuprates: a CuO_2 plaquette with Cu atoms in orange and O atoms in blue, with a lattice spacing of a ~ 3.8 Å. (b) The reciprocal lattice with high-symmetry points marked and labelled in reciprocal lattice units (r.l.u.). M denotes the antiferromagnetic scattering vector, while Γ gives the center of the 2DZB [14].

Before the advent of RIXS, the magnetic properties of cuprates have been studied primarily, if not exclusively, with inelastic neutron scattering (INS), providing a huge amount of experimental information [15]. INS measurements works mainly in the region close to the antiferromagnetic ordering wavevector $\mathbf{q}_{AFM}$ = (0.5, 0.5),

where a magnetic Bragg peaks and well-defined high-energy magnetic excitations have been probed. In superconducting samples an *hour-glass-shaped* dispersion of magnetic excitations has also been found.

When insulating parent compounds are doped, the long-range spin order is indeed destroyed and superconductivity emerges above a certain critical doping. Magnetic fluctuations do not necessarily completely suppress upon doping, despite the absence of a strict long-range order. Spins in the superconducting state can retain a correlation length large enough to promote a local arrangement of magnetic moments whose behavior mimic what observe in the undoped regime.

Due to their persistence up to the superconducting state, magnetic excitations in cuprates have attracted a lot of interest [16] and recent experimental evidences also suggest the hypothesis of a spin mediated paring mechanism in HTS cuprates [17]. A more detailed discussion of this topic will be provided in Chapters 4 and 5, which are almost completely devoted to the description of recent results concerning magnetic excitation in a wide range of dopings and materials.

The next step consists in the understanding of what happens when cuprates parent compounds are doped. In cuprates, CuO_2 planes are intercalated by other layers, usually named *charge reservoir* or *blocking* layers, as shown in Fig. 1.4.

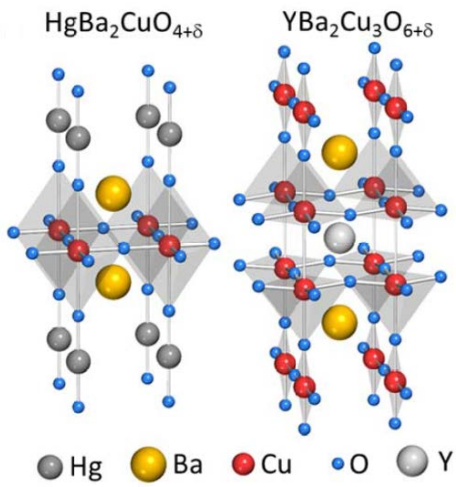

Fig. 1.4: Crystal structures of $HgBa_2CuO_{4+\delta}$ and $YBa_2Cu_3O_{6+\delta}$. $HgBa_2CuO_{4+\delta}$ presents a tetragonal symmetry and one CuO_2 plane per primitive cell, while $YBa_2Cu_3O_{6+\delta}$ has and octahedral symmetry and two CuO_2 planes per primitive cell. In both compounds the charge carrier in CuO_2 planes is controlled by the variation of the interstitial oxygen concentration [18].

These layers control, through chemistry, the number of electrons in the available electronic states in the CuO_2 planes and electronically connect or isolate the CuO_2 planes with each other. When the net charge is changed, forcing the formal valence of Cu^{2+} ions to become higher or lower, the system is doped and superconductivity can occur. This is accomplished through the manipulation of the charge reservoir layer, either by partial substitution of one atom of higher or lower valence or by adding oxygen, like in the examples of Fig. 1.4.

In Fig. 1.5 a schematic layout of cuprates phase diagram is shown as a function of doping.

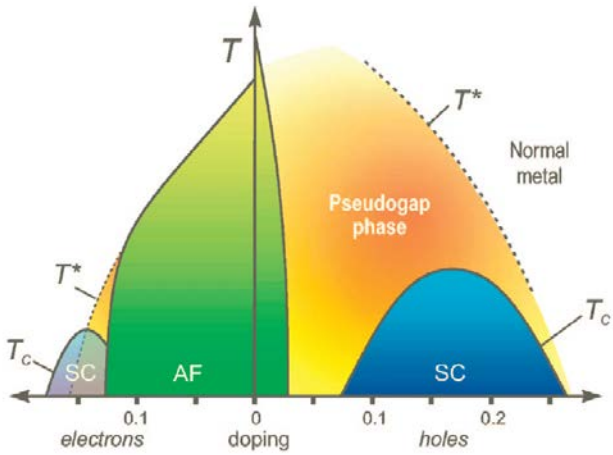

Fig. 1.5: Schematic doping phase diagram of electron- and hole-doped cuprates superconductors. Antiferromagnetic (AF) and superconducting (SC) phases are shown. Fig. reproduced from Ref. [19].

Adding either holes or electrons in the CuO_2 planes of an insulating cuprate parent compound, the system becomes superconductor and T_c increases to reach a maximum in correspondence of the so called *optimal doping*. For a further increase of the doping concentration, T_c goes to zero and the system behaves in first approximation as a metal. The expression *underdoped* and *overdoped* refers to regions with a doping level correspondingly lower or higher than optimal.

Beyond antiferromagnetism (AF) and superconductivity (SC), cuprates phase diagram is exceptionally rich. Different phases and ordering phenomena coexist and compete in a way that has not been totally understood so far [20].

Above the superconducting dome, for example, we note the so called pseudogap phase, which is associated with a partial reduction of the electronic

density of states, as the sample is cooled from high temperature through the pseudogap temperature [21]. The pseudogap exhibits many exotic properties and it is not even a well-defined phase, indeed his characteristic temperature largely depends on the probe used, thus physicists often refers to this region of the phase diagram as a *pseudogap regime*.

Other ordering phenomena occur in cuprates, such as uniaxially modulated antiferromagnetism, spin and charge order, or bidimensional charge density waves, which are briefly discussed in Chapter 6.

Chapter 2

Soft resonant inelastic x-ray scattering

Resonant inelastic x-ray scattering (RIXS) is an extremely powerful spectroscopic technique for probing the low energy excitations in strongly correlated electron systems, such as cuprates. RIXS can indeed access charge, magnetic, orbital and lattice excitations with both energy and momentum resolution. It also provides element and orbital selectivity and bulk sensitivity, while being compatible with small samples measurements.

In this Chapter RIXS is briefly reviewed with a particular focus on the case of Cu-L_3 edge excitation energy, i.e. the energy of the incoming photon is tuned at an absorption edge of the system, corresponding to the $2p_{3/2} \rightarrow 3d$ transition resonance for the Cu $3d^9$ ions present in the CuO_2 cuprates planes. An explanation of the scattering process and its main characteristics is given, together with a detailed description of the accessible excitations.

The last part of the Chapter is dedicated to the derivation of the Kramers-Heisenberg expression for the double differential RIXS cross-section in the electric dipole approximation. Possible computational estimations of the RIXS cross-section are also introduced and discussed.

A more exhaustive description of RIXS and its cross-section could be found in Refs. [22,23].

2.1 The scattering process in RIXS

RIXS is a *photon in-photon out* synchrotron based spectroscopic technique. Despite being well known since a few decades, its fame in the study of elementary excitations in solids has been recently boosted by both the development of dedicated high resolution spectrometers and new generation synchrotron radiation facilities. In the following we mainly focus on the theoretical and physical properties of the RIXS process, while a detailed description of the instrumental aspects and the experimental apparatus needed is provided in Chapter 3.

When an incoming photon hits the sample, the radiation-matter interaction can cause the emission of a scattered photon in an arbitrary direction and with a given energy, momentum and polarization state. Due to this interaction, the system itself is usually left in an excited state different from the ground state.

Since the energy of the incoming photon is known, by accurately measuring the energy of the emitted photons in a given direction, it is possible to determine the energy transferred to the sample in the scattering event and to generate the spectrum of the excitations corresponding to different energy losses. Moreover, the momentum transfer from the incoming photon to the sample depends on the scattering geometry. By properly varying the measurement geometry it is possible to obtain different excitation spectra and generate dispersion maps. Energy, momentum-dependence, symmetry and physical origin of the excitations occurred in the sample can be inferred from the study of the RIXS spectral features.

The RIXS spectra are thus obtained by the accurate measurement of the change in energy and momentum of x-rays that are scattered from the material, leaving the sample itself in an excited state as a result of the scattering process. This can be formalized considering the conservation laws for energy and momentum of the whole system made by photon and sample, before and after the scattering event. Assuming that the sample lies in its ground state before the interaction with x-ray takes place, we can impose:

$$\hbar w_i = \hbar w_o + E^{exc} \tag{2.1}$$

$$\hbar \mathbf{k}_i = \hbar \mathbf{k}_o + \hbar \mathbf{q}^{exc} \tag{2.2}$$

where E^{exc} and $\hbar\mathbf{q}^{exc}$ are the energy and the momentum of any arbitrary excitation occurred in the sample, while $\hbar w_i$ ($\hbar w_o$) is the energy of the ingoing (out-

going) photon and $\hbar\mathbf{k}_i$ ($\hbar\mathbf{k}_o$) is the corresponding momentum.

A third conservation law applies to the total angular momentum of the system (photon plus sample) and regards the polarization state of the ingoing (ε_i) and outgoing (ε_o) photons.

In order to retrieve a complete knowledge of the excitation that has taken place in the system, incident and scattered photons have to be fully characterize in terms of energy ($\hbar w_i$ and $\hbar w_o$), momentum ($\hbar\mathbf{k}_i$ and $\hbar\mathbf{k}_o$) and polarization state (ε_i and ε_o).

In real experiments the parameters describing the ingoing photons are usually well-known and subjected to strong constrains dictated by the choice of the resonance at which the measurements is performed (i.e. Cu-L_3 = 931 eV for cuprates), while a well-defined incident polarization is guaranteed by the use of a synchrotron radiation source. On the other hand, the parameters describing the outgoing radiation can be determined by a properly designed spectrometer.

In first approximation, the whole RIXS process has been described as the inelastic scattering of a photon from a sample, so that RIXS could be defined as an *energy loss spectroscopy.* More precisely, RIXS is based on a two-step process, as explained with the help of the energy diagram of Fig. 2.1, in which we have chosen to illustrate the particular case of the L_3 resonance in the Cu $3d^9$ ions present in cuprates.

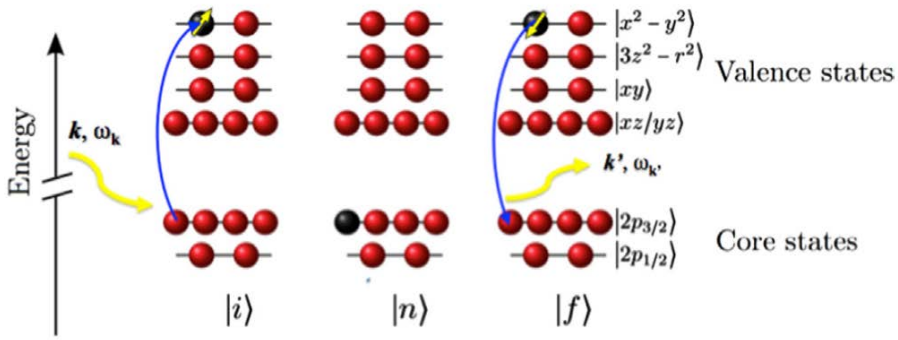

Fig. 2.1: Schematic layout of the RIXS process showing the case of the Cu-L_3 edge resonance. From left to right, the initial |i⟩, intermediate |n⟩, and final |f⟩ states are shown. Red spheres denote states filled by electrons and black spheres by holes. Incoming and outgoing photons are represented as wavy yellow lines and the blue arrows depict transitions. Fig. reproduced from Ref. [24].

The system in the initial ground state |i⟩ has one hole in the Cu 3*d* valence band, which is filled by the incident x-ray exciting a $2p^{3/2}$ core electron to form a highly energetic intermediate state |n⟩.

Due to the strong spin-orbit coupling of the core hole, the orbital angular momentum of the photon can be exchanged with the spin angular momentum of the valence hole, in order to create a spin-flip excitation while conserving total (spin and orbital) angular momentum, as schematized in Fig. 2.1 [22]. This magnetic excitation is particularly important for understanding the data shown in Chapters 4 and 5, although this is not the only possible excitation.

The intermediate state |n⟩ is extremely unstable and within its lifetime (~ 1 fs) the system rapidly decays back into a final state |f⟩ by emitting another x-ray photon when the core hole is filled from a valence electron. In general, the final state |f⟩ does not coincide with the ground state of the system. This means that |f⟩ is an excited state which can contain magnetic, charge, orbital and/or lattice excitations. It is also possible to have an elastic scattering, i.e. $\hbar w_i = \hbar w_o$, where no excitations are left in the system, which is brought back into its ground state.

2.2 RIXS peculiarities

Despite holding analogies and complementarities with numerous techniques used in the last years for the study of elementary excitations in solid and in particular in cuprates, such as inelastic neutron scattering (INS) and Raman spectroscopy for probing magnetic excitations, or electron energy loss spectroscopy (EELS), scanning tunneling microscopy (STM) and angle resolved photoemission (ARPES) for probing electronic structure, a number of characteristics makes RIXS an unequalled technique for condensed matter physics studies. In the following we try to review the most important ones.

First of all, RIXS preserved the overall *neutrality* of the system during the scattering process. It is a *photon in-photon out* technique and no charge is added or removed from the sample under investigation. This is particularly important when working with insulating samples, like several correlated systems and cuprates parent compounds, in order to avoid possible unwanted charging problems.

As anticipated before, RIXS is a resonant technique, i.e. the system is excited resonantly with an absorption edge. This provides *element (and chemical) selectiv-*

ity. An absorption edge can indeed be considered as a signature of a specific element. In resonant-IXS the scattering process from the chosen element is thus predominant allowing studying element specific elementary excitations.

Moreover, energy and shape of the absorption edges are influenced by the chemical environment. As long as their energy separation is wide enough, compared to the experimental energy resolution, atomic species with different oxidation states or coordination symmetries can be distinguished and selectivity excited. The latter is better explained in Fig. 2.2, where the Cu-$L_{2,3}$ edge absorption spectra measured in three different compounds are shown. The oxidation state of Cu ions differs in each of them: copper metal, Cu_2O (Cu^{1+}) and CuO (Cu^{2+}), giving a sizable variation in energy and shape for the corresponding edges [25].

By properly tuning the incoming photon energy, it is thus possible not only to choose the element under investigation, but also the fraction of ions with a certain chemical environment. RIXS is also a site-selective technique.

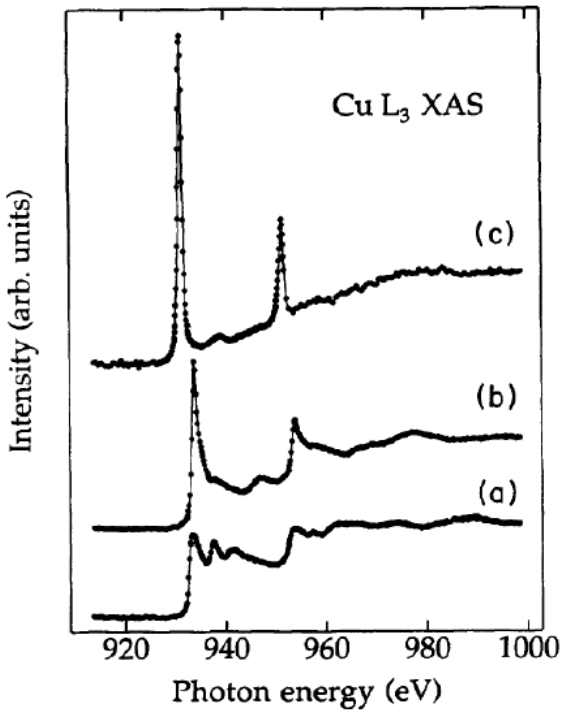

Fig. 2.2: Cu-$L_{2,3}$ edge x-ray absorption spectroscopy (XAS) of (a) copper metal, (b) Cu^2O (Cu^{1+}) and (c) CuO (Cu^{2+}). Fig. reproduced form Ref. [25].

Another important aspect of RIXS is its *bulk sensitivity*. Given that the penetration depth of photons depends on their energy, for x-rays this distance varies from tens of nm in the soft x-ray regime, to few μm in the hard x-ray energy range, as shown in the simulation of Fig. 2.3. This means that RIXS allows studying bulk excitations without dramatic artifacts due to surface effects or contaminations.

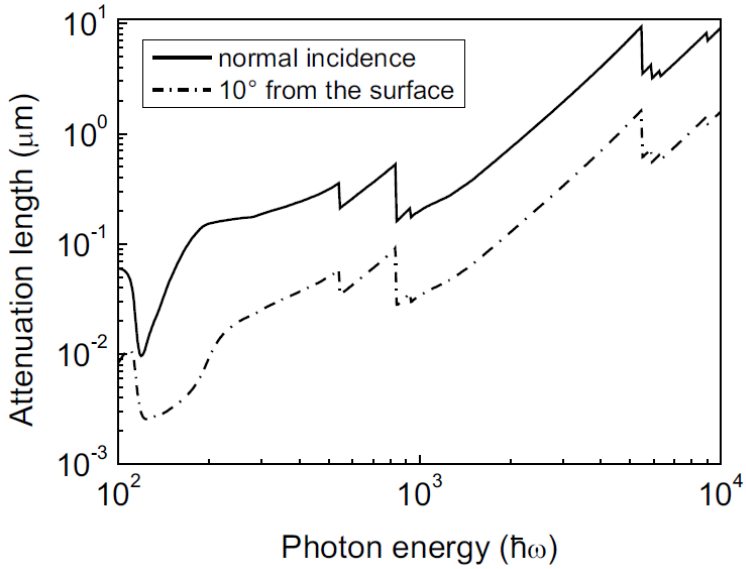

Fig. 2.3: Simulated x-rays attenuation length in cuprates as a function of the photon energy, ranging from 100 eV to 10 keV. La_2CuO_4 has been chosen as a model material. The simulations were carried out from the CXRO online simulator of the Lawrence Berkeley National Laboratory [26].

Bulk sensitivity does not mean that RIXS studies are restricted to massive crystalline samples. Combining the chemical selectivity to bulk sensitivity it is indeed possible to safely investigate surface states, buried interfaces, multilayers and very thin films down to a few unite cells of materials making RIXS an extremely flexible technique.

To enhance the surface sensitivity or to avoid self-absorption effects, it is also possible to play with the experimental geometry, for example by working in grazing incidence conditions, where the attenuation length is estimated to decrease by roughly an order of magnitude over the whole x-rays energy range at an angle of 10° from the sample surface [26].

Penetration depth of soft x-rays is long enough to guarantee bulk measure-

ments with RIXS, but it is also far shorter than that of thermal neutrons. This is mainly due to the weak interaction between neutrons and matter, especially when compared to the resonant RIXS process. Neutrons travel several cm through the sample before scattering and large single crystals (several cm^3 in volume) are required for most INS experiments on cuprates [27]. This explains why INS is now challenged by RIXS in the measurements of magnetic excitations in solids, despite the high energy resolution (below 1 meV) and the relatively simple and well understood cross-section, that allows to directly determine the magnetic dynamical structure factor $S(\mathbf{Q},\omega)$. State-of-the-art RIXS [28] count rate normalized to the probed sample volume is 10^{11} higher than the INS [29] one. This enhanced RIXS sensitivity is particularly important when investigating small samples, down to nanopatterned samples, as the ones shown in Chapter 4, for which INS is not an option.

Finally, RIXS has ***q**-resolution*. Photons carry a momentum inversely proportional to their wavelength (λ). This momentum is usually negligible for visible light, but it becomes not-negligible for x-rays where $\lambda \sim 1$ Å, compatible with the interatomic distances in solids. A sizable fraction of the first Brillouin Zone (BZ) can thus be probed, contrarily to experiments using optical photons, which are restricted to a region very close to the Γ point. This is the case, for example, of Raman scattering [30].

2.3 Excitations accessible to RIXS

RIXS can probe excitations linked to the charge, spin, and orbital degrees of freedom of the studied system, and to its lattice dynamics. In particular, high resolution RIXS is widely used nowadays to measure both ligand field (*dd*) and magnetic excitations in cuprates, as have been recently demonstrated both theoretically and experimentally [31-34]. The recent improvements in resolution and the consequently capability to deeper investigate the so called quasi-elastic features [35] have more recently expanded the panoply of investigable phenomena, definitely setting RIXS has the leading technique in HTC cuprates studies.

In general terms, the different excitations accessible by RIXS can be recognized and classified by exploiting their energy, momentum, and polarization dependence.

The energy dependence of RIXS features allows discriminating Raman from not-Raman (or fluorescence) excitations. This can be done slightly varying the energy of the incoming photon across a given absorption peak. Raman-like excitations are found at constant energy loss in the RIXS spectrum; on the contrary, non-Raman-like features are emitted at constant outgoing energy independently on the incident one. This discerning technique has been recently used to experimentally probe the nature of magnetic excitation in HTC cuprates, as better explained in Chapter 4.

The intensity of both Raman and non-Raman features also changes when the incident photon energy is varied across an absorption edge, because of absorption cross-section effects; this provides information regarding the energies at which the different features resonate.

The evolution of Raman-like features while changing the momentum transfer provides a way to discriminate between local and collective excitations. In general, collective modes can be described with an assigned wave-vector $\mathbf{q}^{exc}$ and they show dispersion, usually symmetric to the $\mathbf{q} \rightarrow -\mathbf{q}$ inversion, which can be mapped in the reciprocal space. For localized excitations, $\mathbf{q}^{exc}$ is not a good quantum number and no dispersion is found. For example, in cuprates the so called *dd*-excitations are expected to have a local character, magnons have a dispersive nature and charge-transfer excitation presents a hybrid character. The latter are excitations associated to an electron transfer from an ion to its ligand, in that way they involve more than one site, but they do not show any clear dispersion.

In principle it is finally possible to use the polarization-dependence of RIXS features to gain further information about them. This requires the capability to measure the outgoing polarization having fixed the incident one. Unfortunately, while in the hard x-ray regime the measurement of the polarization of the scattered photons is nowadays feasible, thanks to the intrinsic polarization selectivity of the Bragg optics, in the soft x-ray energy range this is much more complicated. Our group has recently implemented a solution for soft x-rays, based on a multilayered mirror, whose prototype has been installed and successfully tested on the AXES spectrometer at the ESRF. Its finalized version is now available on the ERIXS spectrometer. For a more detailed description of these *polarimeters* and the interpretation of the spectra resolved in outgoing polarization we refer to Chapter 3.

We now focus on Cu-L_3 edge RIXS, and we describe the most important excitations, among the ones probed by RIXS, with respect to the experimental results shown in this thesis. An analogous discussion can be developed for other excitation edges.

A typical RIXS spectrum is presented in Fig. 2.4; the RIXS intensity is plotted as a function of the energy transferred during the scattering process.

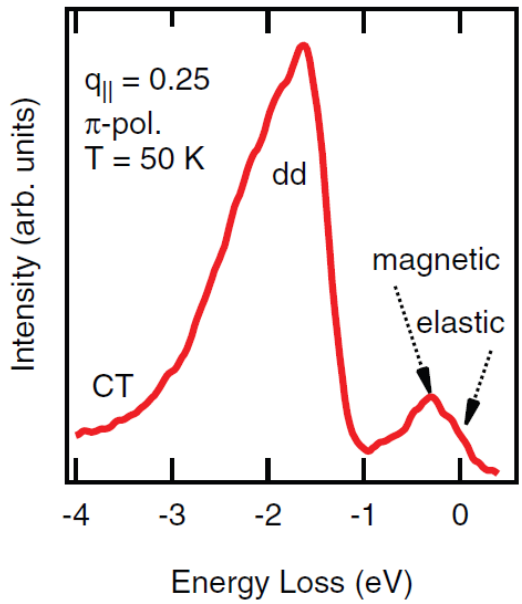

Fig. 2.4: Resonant soft x-ray scattering from optimally doped Bi2212. Quasi-elastic peak, phonons (~ −0.07 eV), magnetic excitations (< −0.35 eV), *dd*-excitations around −2 eV and charge transfer continuum are indicated [36].

From Chapter 1 we know that the Cu 3*d* states split in energy as a consequence of the symmetry breaking introduced by the presence of the ligand atoms. Ligand field (*dd*) excitations takes place when the initial $|i\rangle$ and the final $|f\rangle$ *d* states are not the same. This happens when the core hole created during the absorption of the incident photon moves back to a different *d* state after the decays of the intermediate state $|n\rangle$. The energy difference between the final and initial *d* states gives the energy of the so-called *dd* (or ligand field) excitation, which is usually around 2 eV. In principle this transition is not allowed by electric dipole selection rules (since $\Delta l = 0$), however RIXS makes it possible by decomposing it in two dipole-allowed transitions having $\Delta l = \pm 1$ (*d*-to-*p* and *p*-to-*d*).

As anticipated before, Cu-L_3 RIXS also gives access to magnetic excitations, such as single and multiple magnons in undoped cuprates. A magnon is a wave-like collective excitation of the electrons spin structure in a crystal lattice. As mentioned in Chapter 1, the ground state of undoped cuprates is always characterized by an

antiferromagnetic order of the spin ½ Cu^{2+} sites in the CuO_2 planes. In this framework the RIXS process can excite a single magnon, due to the strong spin-orbit interaction in the 2*p* core hole present in the intermediate state. A multiple magnon can also be formed as the combination of a few single magnons propagating simultaneously in different directions. If the multiple magnon is made by an even number of spin-waves, the total spin moment of the system is conserved, while it is not conserved if the number of spin-waves is odd. In any case, finite energy and momentum have been transferred from the scattered photon to the system itself as a net result of the process.

So far we did not discuss the elastic peak. In a first order approximation, its intensity can be directly related to the specular reflection from the sample surface, and it usually decreases while moving away from the specular scattering geometry. A deeper investigation of the quasi-elastic region of the spectrum can actually reveal the presence of many other excitations, such as phonons and charge or spin ordering phenomena, not clearly distinguishable since a few years ago, due to the intrinsic width of the elastic peak given by the instrumental resolution. We will return on this point in Chapter 6.

In conclusion, in Fig. 2.5 the RIXS process is summarized and a typical RIXS spectrum from cuprates is shown.

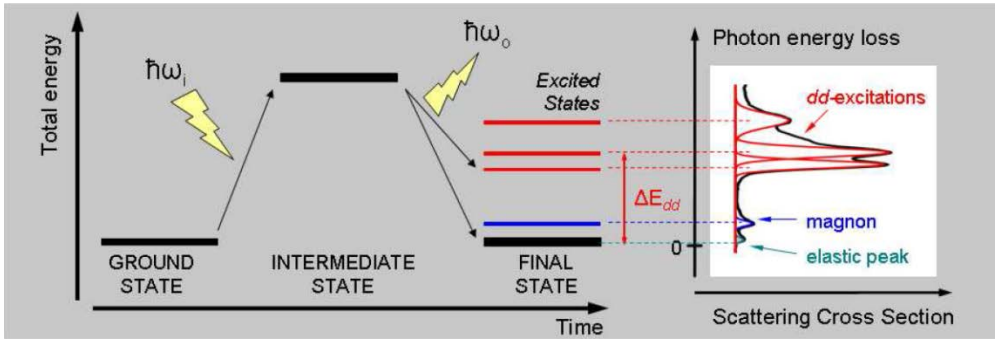

Fig. 2.5: Energy scheme of Cu-L_3 RIXS illustrated as a two-step process. The associated typical RIXS spectrum of a cuprate is shown in the insert on the left. The most important excitations are evidenced and connected to the transition from which they are generated. Fig. reproduced from Ref. [13].

2.4 RIXS cross-section

In this section the expression for the RIXS cross-section is derived along the lines of Ref. [22].

The first step is to write the Hamiltonian of the system. The incident x-rays are described by an electromagnetic field with wave-vector potential $\mathbf{A}(\mathbf{r},t)$, coupled with electrons accordingly to the theory of quantum electrodynamics. In the non-relativistic case and in the limit that both the potentials related to photons and electrons in the system are small compared to twice the mass of the electron, the Hamiltonian for a system with *N* electrons interacting with an electromagnetic field is written in SI units as:

$$H = \sum_j^N \frac{\left[\mathbf{p}_j + e\mathbf{A}(\mathbf{r}_j)\right]^2}{2m} - \sum_j^N e\varphi(\mathbf{r}_j) + \sum_j^N \frac{e\hbar}{2m}\boldsymbol{\sigma}_j \cdot \mathbf{B}(\mathbf{r}_j) + \sum_j^N \frac{e\hbar}{2(2mc)^2}\boldsymbol{\sigma}_j \cdot \left\{\mathbf{E}(\mathbf{r}_j) \times \left[\mathbf{p}_j + e\mathbf{A}(\mathbf{r}_j)\right] - \left[\mathbf{p}_j + e\mathbf{A}(\mathbf{r}_j)\right] \times \mathbf{E}(\mathbf{r}_j)\right\} + \sum_j^N \frac{e\hbar^2\rho(\mathbf{r}_j)}{8\varepsilon_0(mc)^2} + \int d\mathbf{k} \sum_\varepsilon \hbar\omega_\mathbf{k}\left(c_{\varepsilon,\mathbf{k}}^\dagger c_{\varepsilon,\mathbf{k}} + \frac{1}{2}\right) \quad (2.3)$$

where $\mathbf{p}_j$, $\mathbf{r}_j$ and $\boldsymbol{\sigma}_j$ are the momentum and the position operators, and the Pauli matrices acting on the *j* electron. $\mathbf{A}(\mathbf{r}_j)$ is the vector potential, $\mathbf{E}(\mathbf{r}_j)$ the electric field and $\mathbf{B}(\mathbf{r}_j)$ the magnetic field. $c_{\varepsilon,\mathbf{k}}^\dagger$ and $c_{\varepsilon,\mathbf{k}}$ respectively creates and annihilates a photon in the mode with wavevector $\mathbf{k}$, energy $\hbar\omega_\mathbf{k} = c|\mathbf{k}|$ and polarization vector $\boldsymbol{\varepsilon}$.

The first two terms of the Hamiltonian are the electrons kinetic and potential energy in the presence of an electromagnetic field, the third term gives the Zeeman splitting and the fourth takes into account the spin-orbit coupling. The fifth term is called the Darwin term and it changes the effective potential at the nucleus, smearing out the electrostatic interaction between electron and nucleus due to the rapid quantum oscillations of the electron. The *s* orbitals are the only affected by this term, since they overlap with the charge density of the nucleus, on the contrary, they are the only ones not influenced by the spin-orbit term. Finally, the last term gives the energy of the radiation as the sum of all the modes. The electrons interaction with other electrons and the nuclei is omitted.

For our purposes, it is convenient to separate the Hamiltonian H into an electron-photon interaction part (H^1), and in two remaining terms, which describe the

electron (H_{el}) and photon (H_{em}) dynamics in the absence of electron-photon interaction. H^1 can be treated as a perturbation to $H_0 = H_{el} + H_{em}$.

H_0 does not contain electron-photon interactions, its eigenfunctions can thus be written as the product of the eigenstates of H_{el} and the eigenstates of H_{em}. We build the photon-field wavefunction by using the creation operator $c^{\dagger}_{\varepsilon,\mathbf{k}}$ on the vacuum state $|0\rangle$, so that: $c^{\dagger}_{\varepsilon,\mathbf{k}} \equiv 0\ , \forall\ \varepsilon, \mathbf{k}$.

To calculate the RIXS cross-section, we assume that there is a single photon in the initial state with momentum $\hbar\mathbf{k}_{\boldsymbol{i}}$, energy $\hbar\omega_{\mathbf{k}_{\boldsymbol{i}}}$ and polarization $\boldsymbol{\varepsilon}_i$, that is scattered to $\hbar\mathbf{k}_{\boldsymbol{o}}$, $\hbar\omega_{\mathbf{k}_{\boldsymbol{o}}}$ and $\boldsymbol{\varepsilon}_o$. The ground state wavefunction $|\mathrm{g}\rangle$, is given by the product of the ground state wavefunction of the material $|g\rangle$ and the one-photon wavefunction, while the final state wavefunction is equivalently denoted by $|\mathrm{f}\rangle$. The states $|\mathrm{g}\rangle$ and $|\mathrm{f}\rangle$ are eigenstates of H_0 with energies $E_{\mathrm{g}} = E_g + \hbar\omega_{\mathbf{k}_{\boldsymbol{i}}}$ and $E_{\mathrm{f}} = E_f + \hbar\omega_{\mathbf{k}_{\boldsymbol{o}}}$, respectively.

The Fermi golden rule to the second order gives the transition rate for the scattering process as:

$$w = \frac{2\pi}{\hbar}\sum_{\mathrm{f}}\left|\langle \mathrm{f}|H^1|\mathrm{g}\rangle + \sum_n \frac{\langle \mathrm{f}|H^1|n\rangle\langle n|H^1|\mathrm{g}\rangle}{E_g+\hbar\omega_{\mathbf{k}_{\boldsymbol{i}}}-E_n}\right|^2 \delta\left[\left(E_f + \hbar\omega_{\mathbf{k}_{\boldsymbol{o}}}\right) - \left(E_g + \hbar\omega_{\mathbf{k}_{\boldsymbol{i}}}\right)\right] \qquad (2.4)$$

where *n* runs over the intermediate states $|n\rangle$, eigenstates of the unperturbed Hamiltonian H_0 with energies E_n.

The first order amplitude generally dominates the second order, but when the incoming photon energy matches an absorption edge of the studied material, the denominator of the second term gets very small and the second term becomes large. As a consequence, in first approximation the first term yields only non-resonant scattering while the second term contains resonant scattering.

By classifying the terms of the expression for the Hamiltonian of the system as powers of $\mathbf{A}(\mathbf{r}_j)$ and separating the contributions to the first order scattering from the ones to the second order resonant scattering, it can be demonstrated that actually the resonant scattering can occur both via a magnetic and a non-magnetic term. An estimate shows that the non-magnetic term dominates so that we can consider just this for the sake of simplicity.

In particular it can be shown that the resonant part of the second order amplitude is given by:

$$\frac{e^2\hbar}{2m^2V\varepsilon_0\sqrt{\omega_{\mathbf{k}_i}\omega_{\mathbf{k}_o}}}\sum_n\sum_{j,j^1}^{N}\frac{\left\langle f\left|\varepsilon_0^*\cdot\mathbf{p}_{j^1}e^{-i\mathbf{k}_o\cdot\mathbf{r}_{j^1}}\right|n\right\rangle\left\langle n\left|\varepsilon_0\cdot\mathbf{p}_j\,e^{-i\mathbf{k}_i\cdot\mathbf{r}_j}\right|g\right\rangle}{E_g+\hbar\omega_{\mathbf{k}_i}-E_n+i\Gamma_n} \tag{2.5}$$

where V is the volume of the system and Γ_n is a lifetime broadening for the intermediate states introduced in order to account for the usually short lifetime of the core hole. It is reasonable to assume that all Γ_n at a certain edge are equal, so that it can be taken $\Gamma_n = \Gamma$.

Substituting the last equation into the previous gives the so called Kramers-Heisenberg expression for the RIXS cross-section.

In the following we use the dipole approximation, so that the scattering amplitude becomes:

$$\frac{e^2\hbar}{2m^2V\varepsilon_0\sqrt{\omega_{\mathbf{k}_i}\omega_{\mathbf{k}_o}}}\sum_n\sum_{j,j^1}^{N}\frac{\left\langle f\left|\varepsilon_0^*\cdot\mathbf{p}_{j^1}\right|n\right\rangle\left\langle n\left|\varepsilon_0\cdot\mathbf{p}_j\right|g\right\rangle}{E_g+\hbar\omega_{\mathbf{k}_i}-E_n+i\Gamma_n}\approx$$
$$\frac{e^2\hbar}{2m^2V\varepsilon_0}\sqrt{\omega_{\mathbf{k}_i}\omega_{\mathbf{k}_o}}\sum_n\sum_{j,j^1}^{N}\frac{\left\langle f\left|\varepsilon_0^*\cdot\mathbf{r}_{j^1}\right|n\right\rangle\left\langle n\left|\varepsilon_0\cdot\mathbf{r}_j\right|g\right\rangle}{E_g+\hbar\omega_{\mathbf{k}_i}-E_n+i\Gamma_n} \tag{2.6}$$

The double differential RIXS cross-section is finally obtained by multiplying w by the density of photon states in the solid angle, and dividing by the photon flux:

$$\frac{d^2\sigma}{d\hbar\omega d\Omega}=r_e^2m^2\omega_{\mathbf{k}_i}{\omega_{\mathbf{k}_o}}^3\sum_f\left|\sum_n\sum_{j,j^1}^{N}\frac{\left\langle f\left|\varepsilon_0^*\cdot\mathbf{r}_{j^1}\right|n\right\rangle\left\langle n\left|\varepsilon_0\cdot\mathbf{r}_j\right|g\right\rangle}{E_g+\hbar\omega_{\mathbf{k}_i}-E_n+i\Gamma_n}\right|^2\delta\left(E_g-E_f+\hbar\omega\right) \tag{2.7}$$

It has to be stressed that the equation obtained in this way holds in the dipole approximation only. This condition is easily fulfilled in the case of soft x-rays and so for all the measurements presented in this thesis. On the other hand, for hard x-ray photons also electric quadrupole transitions has to be taken into account in the study of the RIXS process.

2.4.1 RIXS cross-section discussion

In the previous section we have mathematically derived the so called Kramers-Heisenberg (KH) equation for the RIXS cross-section. We now try to briefly discuss it, pointing out its most important implications.

For a generic RIXS process both the incoming and the outgoing radiative transitions are necessary, so that the two dipole operators need to be multiplied. This product is divided by a factor which goes close to zero in case of resonance; this explains why the process cross-section increases for resonating transitions. We note that the division by zero is forbidden by the presence of the imaginary term, due to the finite linewidth of each intermediate state.

The KH equation assures the respect of the energy conservation law, indeed the difference in photon energies equals the excitation energy of the system. Consequently, any spectral peak due to a well-defined excitation of the sample is found at constant transferred energy.

We also notice that energy loss peaks disperse linearly with incoming photon energies, providing a simple criterion to distinguish them from any other spectral feature, such as fluorescence emission peaks. The energy of the last in fact is fixed by the atomic species in the sample and does not depend on the excitation energy. Fluorescence features are generally less important than the Raman ones, because they correspond to the decay of an electron that has already relaxed, losing the information about the RIXS intermediate state of the system.

In general, the intermediate states have a crucial role in RIXS. The presence of an intermediate state between two consecutive dipole transitions provides for instance the possibility to follow a path from the ground to the final state which in direct way is forbidden by dipole selection rules, *dd*-excitation (i.e. an excitation in the same valence shell) is a typical example. Moreover, this path introduces also sensitivity to polarization, so that the knowledge of incoming and outgoing polarizations can allow unraveling the local symmetry of the excitations, as better discussed in Chapter 3, where polarimetric measurements and apparatus are presented.

In a realistic description of a generic RIXS process, sets of degenerate intermediate and final states can be present. In particular when we consider the intermediate states, which are not observed directly, we must do a coherent sum and superimpose amplitudes taking into account relative phases. Only after this operation the total amplitude must be squared. In the case of final states instead, since they are actually observed, there is no need of these considerations.

In the particular case of layered cuprates, Cu ions are known to be mostly in the Cu^{2+} oxidation state, corresponding to a $3d^9$ electronic configuration. In the crudest approximation, the RIXS process can be modeled in two steps, by considering only atomic states of a Cu^{2+} ion. First of all, one $2p_{3/2}$ electron is resonantly promoted into the 3*d* intermediate states by absorption of a photon. Because of the large 2*p*

spin-orbit splitting (~ 20 eV), interference effects with the $2p_{1/2}$ states can be neglected. The second step constitute in the radiative decay of a 3*d* electron into the $2p_{3/2}$ levels. The only available intermediate state is given by a fully occupied 3*d* shell and one hole in the four-fold degenerate $2p_{3/2}$ core level. This makes the calculations of Cu-L_3 RIXS cross-section much easier than in the presence of a manifold of intermediate states, as it happens in general, for more details on these single ion calculations we refer to Ref. [31].

Unfortunately this single ion model is strictly valid only in the case of insulating parent compounds. When considering superconducting cuprates, calculations become much more complex preventing the possibility to directly solve the KH equation. Only in the last years, theoretical estimations of the RIXS cross-section for doped cuprates have been provided [37,38], whose main findings will be discussed in the next Chapters in connection with our experimental results.

We would like to finally stress that the resonance acts as a real amplifier increasing remarkably the cross section of the process and improving the sensitivity of the measurements. Due to the small matrix elements of the second order process in fact the intensity of RIXS signal is quite weak. This is the main reason behind the necessity to use high sensitive ad hoc instrumentation and sources with very high brilliance, such as the ones described in the following Chapter.

Chapter 3

Advances in instrumentation

Resonant inelastic x-ray scattering success has rapidly grown in the last decades, sustained by both the construction of third generation radiation sources and the design of dedicated RIXS spectrometers. These progresses have allowed overcoming the limitations due to the poor energy resolution and to the low photon flux provided by old generation synchrotrons; RIXS is indeed an extremely *photon-hungry* technique, being base on a second order process.

The remarkable results obtained by physicists in the study of elementary excitations with RIXS, have boosted a continuous effort in the development of improved instrumentation. And nowadays a new generation of advanced high resolution RIXS end stations is under construction in many facilities around the world. Among these facilities, there are big expectations also for x-ray free electrons lasers (XFEL) and their possible cross-fertilization with RIXS.

The physics underneath hard and soft x-ray RIXS is similar, but they require very different experimental set-ups. This thesis mostly deals with soft x-ray RIXS performed at Cu-L_3 edge. We thus focus only on the instrumentation required for this energy range.

In particular, we briefly present the main features of a soft x-ray beamline, us-

ing as a reference the new ID32 beamline of the European Synchrotron Radiation Facility (ESRF) in Grenoble. The data shown in Chapter 3, 4 and 5 have been all acquired with two dedicated RIXS spectrometers: SAXES [39] located at the ADRESS [40] beamline of the Swiss Light Source (SLS), at Paul Scherrer Institut (PSI) in Villigen (CH), and AXES [41,42] at the ID08 beamline of the ESRF. The latter has been now dismissed and substituted with the new ERIXS (European-RIXS) spectrometer settled at ID32 [43].

ERIXS is at the moment the only fully operative new generation soft-RIXS spectrometer. Its layout is introduced in general terms, together with a comparison with the AXES and SAXES spectrometers. Similarities and differences are underlined; while a selection of data from ERIXS commissioning and first users experiments are used to show the improvements in performances. The typical experimental geometry is also introduced.

The last session of the Chapter is devoted to the description of the *polarimeter* prototype that we mounted and successfully tested on AXES, providing for the first time the possibility to detect the polarization of the scattered beam in energy resolved soft x-ray scattering. Some references to the new polarimetric setup installed on ERIXS are also provided.

3.1 A typical soft synchrotron beamline: ID32 at ESRF

A detailed discussion of the three beamlines where the experiments presented in this thesis have been performed goes far beyond our purposes. In the following ID32 soft x-ray beamline is just briefly introduced underling the aspects that make it unique and the features that are instead common to soft x-ray beamlines.

ID32 is freshly new, it has replaced the former soft ID08 beamline and it was inaugurated only one year ago, in the framework of a major ESRF upgrade program (ESRF Upgrade Phase I) which has started in 2009.

The European Synchrotron Radiation facility (ESRF) is a synchrotron light source funded and operated by 19 countries since 1994 in Grenoble, France [44]. With its 41 experimental stations and more than 6000 visiting scientists every year, it is one of the three biggest synchrotron facilities in the world. The storage ring has a circumference of 844 m, and the current in the ring can reach 200 mA, with a value of 6 GeV for the electron energy. It is thus conceived to work mostly in the hard x-

ray regime and it holds one of the highest brightness in this energy range, in order to increase which, the ring itself will undergo a complete upgrade in the years to come (ESRF Upgrade Phase II).

ID32 is the only soft x-ray beamline of the ESRF, and it operates in the photon energy range from 400 to 1600 eV. It is mainly devoted to the study of magnetism and electronic structures of materials, covering in particular the *K* edges of O, the $L_{2,3}$ edges of 3*d* transition-elements compounds and the $M_{4,5}$ edges of rare earths. The principle techniques available are: x-ray magnetic circular dichroic (XMCD), x-ray absorption spectroscopy (XAS), resonant inelastic x-ray scattering (RIXS), soft x-ray diffraction and coherence measurements.

It is an extremely long beamline, i.e. 120 m long, and features two branches with different optical schemes. One branch provides very high energy resolution for RIXS experiments, aiming at a resolving power of ~ 42,000. The second branch specializes in XMCD experiments with a moderate resolving power of ~ 5,000 and adjustable beam sizes. A third experimental area dedicated to non-routine experiments is available on this second branch. At top view of the beamline is shown in Fig. 3.1.

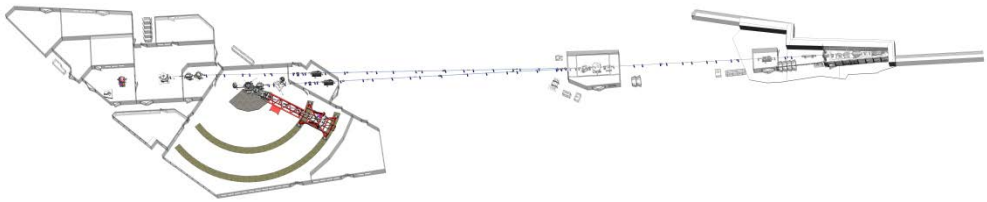

Fig. 3.1: The 120 m long ID32 beamline at the ESRF, top view. ERIXS spectrometer is drawn in red. Fig. reproduced from Ref. [45].

The beam source is constituted by three APPLE II undulators [46], two of them are 1.6 m long and the central one is 2.5 m long, having the same period and providing an effective length of 5.7 m. They adopt the so called Apple-type scheme in which the polarization as well as the energy can be changed by the variation of 4 moveable permanent magnet arrays. Such undulators provide 100% controllable polarization, both linear and circular, of the emitted radiation.

The beam spot size at the sample has been characterized and it can be focalized down to 4×60 microns (FWHM, vertical ×horizontal) for the RIXS branch, while it ranges from 10×100 microns up to several mm^2 (FWHM) for the XMCD branch.

A series of optical elements, mainly based on properly machined mirrors operating at grazing incidence, deflect, shape and monochromatize the beam. Their description is beyond our purposes and we refer to a more detailed related literature. For completeness we just show a scheme of the optical layout for the two branches in Fig. 3.2.

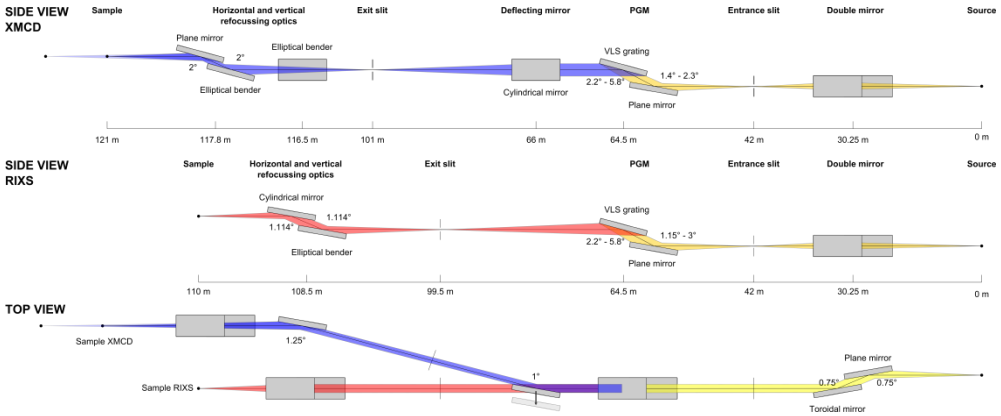

Fig. 3.2: Schematic of ID32 optical layout. Along the XMCD branch, the 300 lines/mm blazed VLS grating creates a virtual focus of the source at the entrance slit independent of the included angle of the monochromator. This virtual image is focused by the cylindrical deflecting mirror onto the exit slit. Bending refocusing optics allow to horizontally and vertically refocus the beam from the exit slit to any point between 2.5 m and infinite along the beamline. Along the RIXS branch, the entrance slit is focused by the VLS gratings (800 lines/mm or 1600 lines/mm) onto the exit slit. A cylindrical sagittal refocusing mirror and an elliptical bender are used. Fig. reproduced from Ref. [45].

3.2 A typical RIXS spectrometer

Two spectrometers have been used to perform the experiments described in Chapter 4, 5 and 6: AXES, which stands for Advanced X-ray Emission Spectrometer, working at the ID08 beamline since 1995, and now dismissed, and its evolution SAXES, i.e. Super AXES, at the ADRESS beamline since 2006.

Both of them have been entirely designed and built in Milan, by the group headed by prof. G. Ghiringhelli and prof. L. Braicovich, in which I performed my

doctorate. In the last year, a new instrument has replaced AXES: ERIXS, European-RIXS, created by collaboration between our group in Milan and the ID32 beamline staff in Grenoble; it now holds the record for energy resolution.

As we can see from Fig. 3.3, the dimensions of the RIXS spectrometers have progressively increased during the years with a corresponding increase in the resolving power, as better clarified later on.

Fig. 3.3: Pictorial view of the historical evolution of soft x-rays RIXS spectrometers. Corresponding dimensions and resolving power at Cu-L_3 are indicated.

The three spectrometers follow the same basic principles for the optical layout. So we first provide a generic description that holds for the three of them. Finally, we highlight the main improvements brought by ERIXS, to whom commissioning was mostly dedicated the last part of my Ph.D. project.

In general, we can simply schematize a RIXS spectrometer with three main elements: a source, an analyzer and a detector. The source of the spectrometer is given by the light spot on the sample, whose size depends on the height of the beam footprint. The scattered radiation emitted by the sample enters the spectrometer and hits at grazing incidence a concave diffraction grating. In the simplest spectrometers, such as AXES and SAXES, this grating is the only optical element. The concave grating has the double function: (i) to focus the scattered beam onto the detector and (ii) to disperse it, spatially separating the different scattered energies. The use of variable line spacing (VLS) gratings with fixed radius of curvature also allows to minimize the linewidth broadening due to the high order optical aberrations, by displacing the grating itself.

Secondly, the grating disperses and focuses the scattered radiation onto a 2D position sensitive charge coupled device (CCD) detector, so that photons position on the CCD surface is directly related to their energies.

In first approximation, the CCD image is made by horizontal isoenergetic lines, parallel among each other. In particular, the lines due to high energy photons will be in the lower region of the image and the lines ascribable to low energy photons in the upper region. Integrating the CCD image along these isoenergetic lines, gives the total RIXS intensity as a function of the energy transferred during the scattering process, as shown in Fig. 3.4.

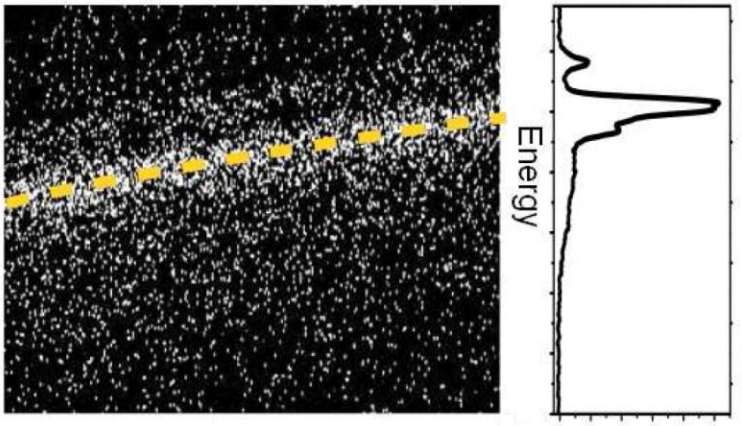

Fig. 3.4: On the left, typical image acquired by a CCD detector in a soft x-ray spectrometer (AXES, at ID08 of ESRF); on the right, integration along the direction indicated by the yellow line leads to the reconstruction of the RIXS spectrum [47].

The position in space of the CCD camera should thus be properly determined and adjusted in order to intercept the energy window of the impinging photons and to put the detector in their focal plane.

Moreover, the detector spatial resolution contributes to the total instrumental energy resolution, together with optical aberrations, grating shape errors and source size. Commercial soft x-ray CCDs have a spatial resolution of about 25 μm [39], independently on the physical pixel size [40]. In fact, when the incoming photon is absorbed in Si, it generates a number of charges proportional to its energy through and Auger cascade. Subsequently these electrons spread by diffusion over an area corresponding to several pixels [48], generating a so called *charge cloud*.

Without implementing any reconstruction algorithm, like the one discussed at the end of this Chapter, the only way to gain in spatial resolution is to mount the CCD at a certain angle with respect to the incoming photons, so to decrease the effective exit slit, as shown in Fig. 3.5.

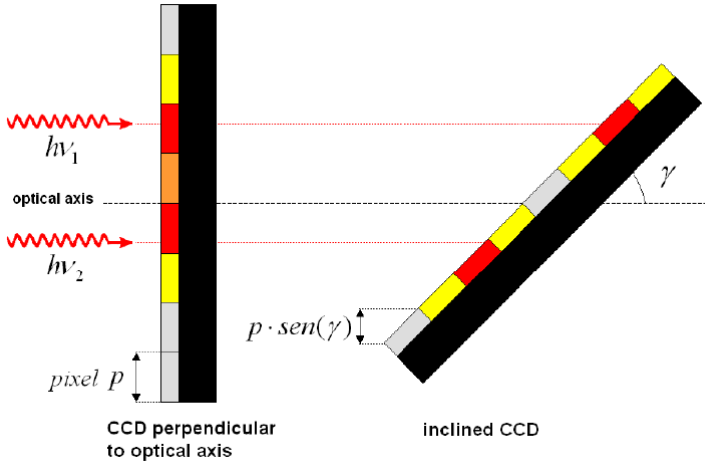

Fig. 3.5: Sketch of the improvement in the effective spatial resolution for an inclined CCD. The gain in spatial resolution is equal sen(*γ*), being *γ* the angle between the detector surface and the optical axis of the spectrometer. Fig. reproduced from Ref. [13].

Finally, the spectrometer length (*L*) and the horizontal dimension of the detector (*D*) determine the angular acceptance of the instrument and the uncertainty on the momentum transfer **q**, in the absence of any collimation of the scattered beam.

In the end, we note that the samples under investigation are mounted on a sample holder and inserted in the measurement chamber. Both, the sample chamber and the optics stay in ultra-high vacuum conditions (UHV, $\sim 10^{-9}$ mbar). This requirement comes from the use of soft x-rays and the need to protect beamline optical elements. The sample holder is traditionally mounted on a manipulator, which allows moving the sample with respect to the beam, changing the scattering geometry.

The higher the control of the sample orientation, the more extended the information retrieved during the experiment. This evidence has become increasingly important during the last years, with the exploitation of the capability to use RIXS for the investigation of ordering phenomena, which requires diffraction like experiments. We refer to session 3.2.3 for a detailed description of the technological solution implemented in ERIXS to achieve the required sample control.

3.2.1 The standard experimental geometry

In this Session we introduce the typical experimental layout used for AXES and SAXES spectrometers. The same basic principles and angles definition follow for ERIXS; however the advances in the spectrometer design also allow panoply of newly exploitable degrees of freedoms.

We stress that the scheme presented here is valid for all the RIXS measurements in Chapters 4, 5 and 6, so that it is described here once for all.

In the particular case of cuprates, it is helpful to remind the quasi-2D nature of these materials. In fact, most of the interesting physics takes place in the CuO_2 planes. This simplifies the experiments, allowing to keep the total moment transfer **q** fixed and to restrict the study of the evolution of elementary excitations to the 2D Brillouin Zone (BZ). The meaningful quantity in the experiments is thus the projection of the transferred momentum onto the cuprates *ab*-plane $\mathbf{q}_{\parallel}$.

In Fig. 3.6 the scattering geometry is presented in both the direct and the reciprocal space following the convention used in Ref. [31].

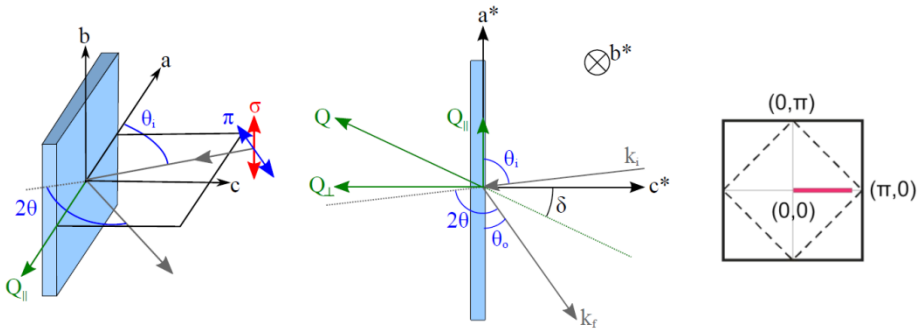

Fig. 3.6: Experimental scattering geometry. From left to right: (i-ii) 3D representation and top view; *a*, *b* and *c* (*a**, *b** and *c**) are the direct (reciprocal) lattice vectors; (iii) sketch of the 2D Brillouin Zone of Cuprates; by changing $\mathbf{q}_{\parallel}$ we can for example move along the purple line, probing the (0,0) → (π,0) direction of the reciprocal space. Dashed lines denote the antiferromagnetic zone boundaries (AFZB) [14].

In more details, $\boldsymbol{k}_i$ and $\boldsymbol{k}_f$ are the scattering vectors for the incoming and the outgoing photon beam respectively; the scattering angle between them is 2ϑ = 130° and is kept fixed in AXES and SAXES experiments. The angle between the sample surface and $\boldsymbol{k}_i$ is denoted with ϑ_i; in analogy ϑ_f is the angle between the

sample surface and $\boldsymbol{k}_f$. The momentum $\boldsymbol{k}_i$ is dictated by the energy of the resonant transition (i.e. Cu-L_3), and the maximum transferred momentum **q** is given by the scattering angle.

During the experiment, the sample is rotated around the vertical axis, changing the projection of **q** onto $\mathbf{q}_{\parallel}$, given by the equation $\mathbf{q}_{\parallel} = 2|\boldsymbol{k}_i|\sin(2\vartheta/2)\sin(\delta)$. This allows studying the evolution of a given excitation along a chosen direction of the square 2D-BZ of cuprates.

Finally, the incoming beam is linearly polarized, with π (electric vector **E** in the scattering plane) or σ polarization (**E** orthogonal to the scattering plane).

3.2.2 AXES versus SAXES, resolution performances

Since AXES and SAXES are the two spectrometers used in most of the experiments presented hereafter, we would like to stress their main difference in performances, which is given by their energy resolution.

In a RIXS spectrometer, the major contributions to resolution come from (i) the finite source size, (ii) the detector spatial resolution, (iii) the grating slope error and (iv) the coma aberrations. The latter can in general be neglected by using a VLS grating and properly adjusting its position according to the working conditions.

The total experimental resolution is given by the quadratic sum of the contributions coming from the spectrometer and the beamline (i.e. the linewidth of the monochromator).

In order to experimentally assess the combined resolving power, what we usually do is to acquire a RIXS spectrum from a sample of polycrystalline graphite. Since it does not show any inelastic features, the full width at half maximum (FWHM) of the elastic peak directly gives the total energy resolution. We note that these graphite spectra are also used during RIXS experiments, in order to calibrate the zero energy loss.

The combined resolution of AXES at Cu-L_3 edge (931 eV) is $\sim$ 235 meV, while SAXES at the same energy provides around 120 meV FWHM, i.e. roughly a factor 2 better, due primarily to the fact that the instrument is roughly twice longer than AXES. This is paid in terms of count rate, which is directly linked to the angular acceptance of the detector. Many other parameters influence the count rate, such as the brilliance of the x-ray source and the roughness of the optics, making it more complex to be estimated.

The need to further increase both the energy resolution and the count rate is

the main reason that pushed the design of a new generation of spectrometers, the first of those is ERIXS. In the next session we thus underline the characteristics that make ERIXS design so innovative compared to the standard RIXS spectrometers described so far.

3.2.3 ERIXS: a new concept of RIXS spectrometer

ERIXS is the evolution of AXES and SAXES. At present, the main limiting factors for the scientific output of soft-RIXS are energy resolution, sample orientation control and count rate, or beamtime availability. The new ERIXS instrument, located at the new ID32 beamline of the ESRF, is going to offer unprecedented and unique performances in all those fields.

We can classify the main novelties of the ERIXS project as: (i) *high energy resolution*, allowing to measure Cu-L_3 RIXS with a combined bandwidth (BW) of 35 meV, decisively better than anywhere else; (ii) *polarization analysis* of the scattered beam, providing a full control on the symmetry of excited states; (iii) diffractometer-quality control of the *sample orientation* and continuous regulation of the scattering angle, allowing energy-resolved elastic scattering experiments and an extended capability to investigate the reciprocal space; (iv) *high luminosity*, thanks to the insertion of an horizontally collimating mirror in the spectrometer optical layout, granting a reasonable count rate over the whole energy range.

The ERIXS structure is shown in Fig. 3.7.

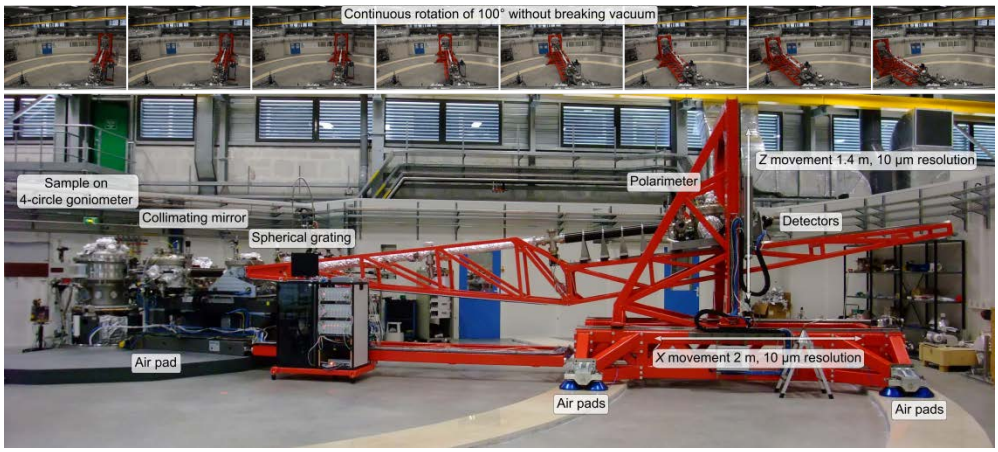

Fig. 3.7: The ERIXS spectrometer at the new ID32 beamline of the ESRF. The top panel shows a cartoon of the continuous 100° scattering arm rotation. Fig. reproduced from Ref. [49].

The spectrometer features an 11 m long scattering arm capable of a continuous rotation over 100° without breaking the vacuum. This was made possible thanks to the innovated design of the sample chamber developed by the Cinel Company [50]. The sample chamber is indeed equipped with a double-differentially pumped steel ribbon with a nozzle that allows 100° free rotation, shown in Fig. 3.8(b). In order to increase the motion stability, the rotation of the scattering arm takes place on air-pads floating on a marble guide with reduced surface roughness.

The full control of the sample orientation is provided by an in-vacuum 4-circle sample goniometer, Fig. 3.8(a). A loadlock and properly in house developed sample holders, Fig. 3.8(c), allow a fast in-vacuum sample transfer. Moreover, a liquid helium flow cryostat provides temperatures down to 20 K at the sample with all degrees of freedom preserved.

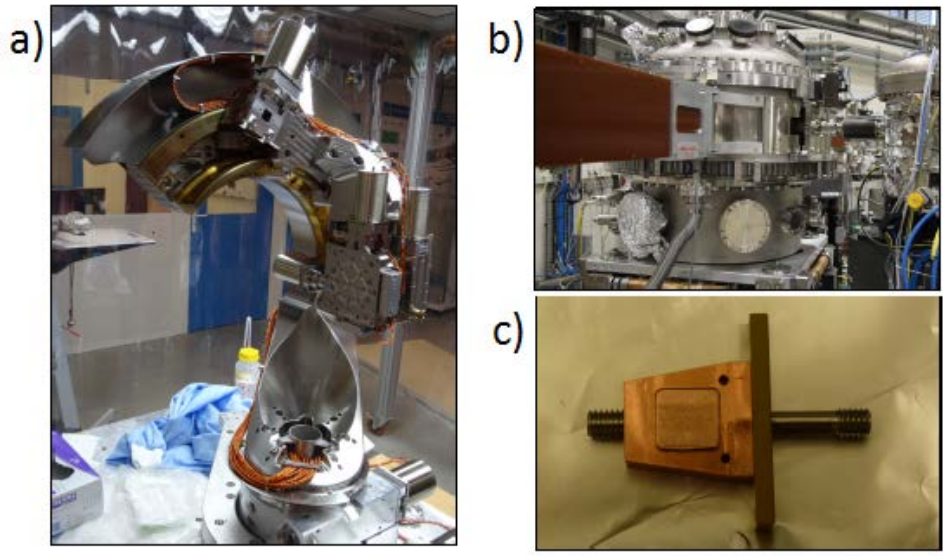

Fig. 3.8: ERIXS sample stage: (a) full 4-cycle goniometer for sample orientation; (b) double-differential pumped steel ribbon and nozzle; (c) sample holder. Fig. reproduced from Ref. [49].

Differently from AXES and SAXES, the ERIXS spectrometer has two optical elements: (i) a collimating mirror and (ii) two exchangeable spherical gratings.

The main difference, compared to previous setup, is given by the first element, as shown in Fig. 3.9. This is a parabolic mirror that can be inserted and removed

from the optical path by a lateral translation. In the absence of the collimating mirror, ERIXS behaves like a traditional spectrometer and the detector collects only a tiny fraction of the diffused scattered radiation solid angle (typically 10^{-6}).

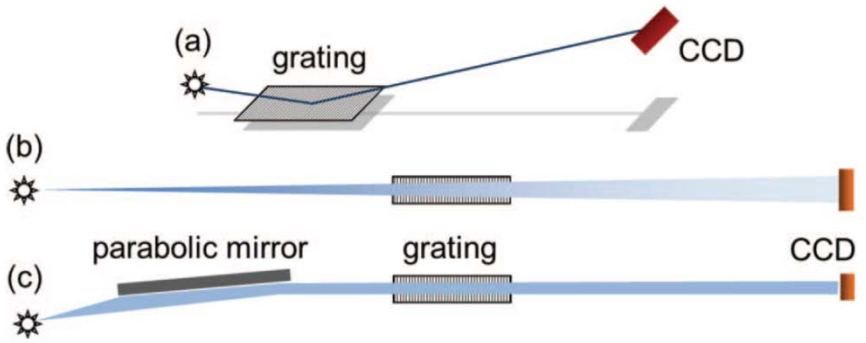

Fig. 3.9: Scheme of soft-RIXS grating spectrometer. (a) Perspective view. (b-c) Top view, in the absence of horizontal focusing (b) and in the case of horizontal collimation obtained with a parabolic mirror (c) [51].

In ERIXS the weakness of the detected signal is crucial, considering the increased length of the scattering arm. The parabolic mirror is thus used to collimate a 20 mrad horizontal fan onto the detector, providing a gain in the detection efficiency. The increased count rate, compared to the former AXES spectrometers, also follows from the optimized luminosity of the beamline and the use of three Apple II undulators in phase. Another source of efficiency gain is given by the long optical leverage of both the ID32 monochromator and the ERIXS spectrometer, allowing reducing the grating ruling density.

The second optical element is a spherical grating, similarly to what we have described for the traditional setup. In particular, the presence of two exchangeable gratings allows choosing between two measurements mode: *high efficiency* (HE) or *high resolution* (HR). The gratings used in the two modes have an average groove density of a_0(HE)= 1400 lines/mm and a_0(HR)= 2500 lines/mm, respectively. The HE grating have been used in the early stage of the commissioning, achieving from day-one the spectrometer target of having 50 meV combined BW at Cu-L_3 edge. This important result is shown in Fig. 3.10, where the energy resolution has been estimated as the FWHM of the elastic peak of polycrystalline graphite. The HR grating has been more recently tested, providing a 35 meV FWHM at Cu-L_3.

We can conclude that ERIXS has an energy resolution 2 to 3 times better than

SAXES already from day one, and further improvements are expected in the months to come with the introduction of a high resolution grating for the beamline monochromator.

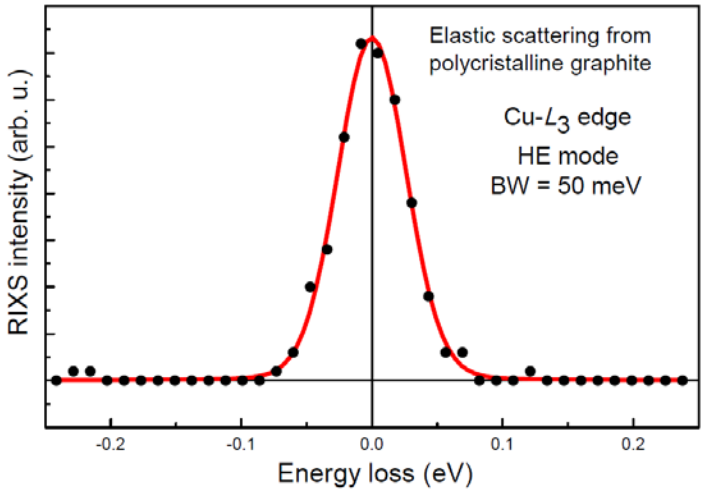

Fig. 3.10: Elastic peak from polycrystalline graphite at Cu-L_3 edge, in high efficiency mode. The day one goal, i.e. having the ERIXS spectrometer working with a combined (spectrometer plus beamline) resolving power of at least 20.000 at 931 eV, has been reached. Spectra have been extracted with the so called Single Photon Counting (see section 3.4).

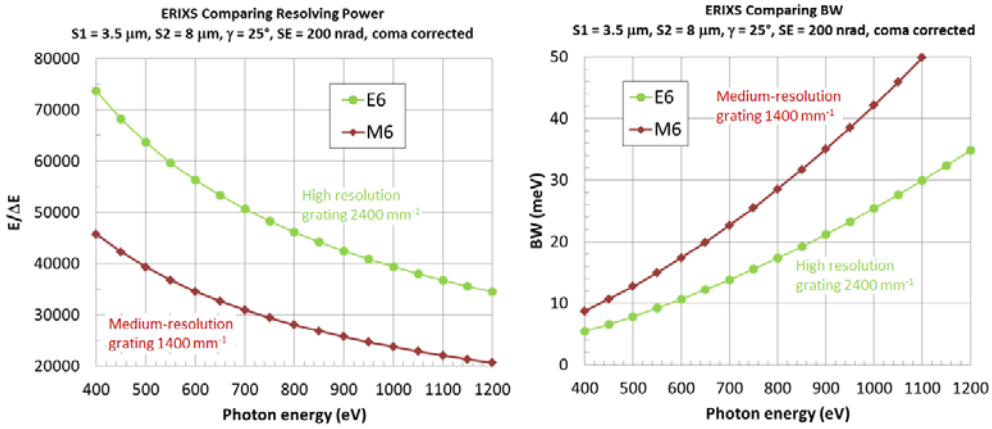

Fig. 3.11: ERIXS spectrometer performances as a function of the incoming photon energy, for the two configurations: HE (green) and HR (red). Resolving power is shown on the left, and energy resolution on the right.

In Fig. 3.11 we also show a comparison, both in terms of expected ERIXS spectrometer energy resolution and resolving power, for the two configurations HE and HR at different incident energies and in typical working conditions. We notice that spectrometer performances improve while moving toward lower energies.

We stress that, since we are dealing with photon energies much larger than that of the excited states, obtaining a good absolute energy resolution requires instrumentation (i.e. both monochromator and spectrometer) with very high resolving power.

Two identical CCD cameras are available for the signal detection. The primary one is positioned along the straight path of the scattered photons and it is used for standard operations, while the second one collects the signal coming from a multilayer mirror based polarimeter. The latter can be inserted in the beam intercepting a fraction of it. The parallel measurements of both the straight and the polarimetric signals allow an analysis of the scattered beam linear polarization. For a description of the first polarimeter prototype installed on AXES and the very first RIXS spectra acquired with the new ERIXS polarimeter, we refer to session 3.3.

The recent improvements in RIXS resolution and efficiency also brought to a growing need of high-resolution high-sensitivity 2D position sensitive detectors working in the soft x-ray regime. As anticipated before, the spatial resolution of CCD cameras is limited by the dimension of the so called charge cloud and gives a finite contribution to the total energy resolution of the spectrometer. In the new generation high resolution ERIXS, the contribution coming from the detector starts to be a limiting factor. This loss of resolution can be overcome with the use of centroid reconstruction methods, where the photon impact position onto the detector is estimated from the intensities accumulated in the different adjacent pixels interested by the charge cloud. This method can work only with isolated events, because overlapping spots can be easily misinterpreted, and it is therefore called Single Photon Counting (SPC) [47].

We performed laboratory tests showing that the spatial resolution achievable with the traditional CCD camera installed on ERIXS is $\sim$ 6 μm or even less. Due to this remarkable achievement, the SPC has become the new standard for the extraction of spectra from the CCD images in ERIXS. We refer to session 3.4 for a description of the SPC algorithm and its laboratory tests.

Finally, it should be noted that the CCD camera are equipped with three motions, along the three directions of space. By properly adjusting the CCD position along with the grating angle and entrance arm, it is possible to cover the entire energy range with no coma aberrations.

In the following, we present a selection of fascinating results coming from the spectrometer commissioning realized in April and May and our experiment in July-November 2015, which has been the very first RIXS experiment at the new ID32 beamline. We mainly provide a phenomenological description, while a more detailed discussion regarding the physical meaning and the implications related to the analysis of accessible spectral features is developed in Chapters 4, 5 and 6.

We started our investigation working in the HE configuration and measuring antiferromagnetic layered cuprates, whose RIXS spectra are characterized by sharp *dd*-excitations and resolution limited spin-waves, dispersing in momentum space from zero to 350 meV. Sample temperature was kept at 35 K during all measurements.

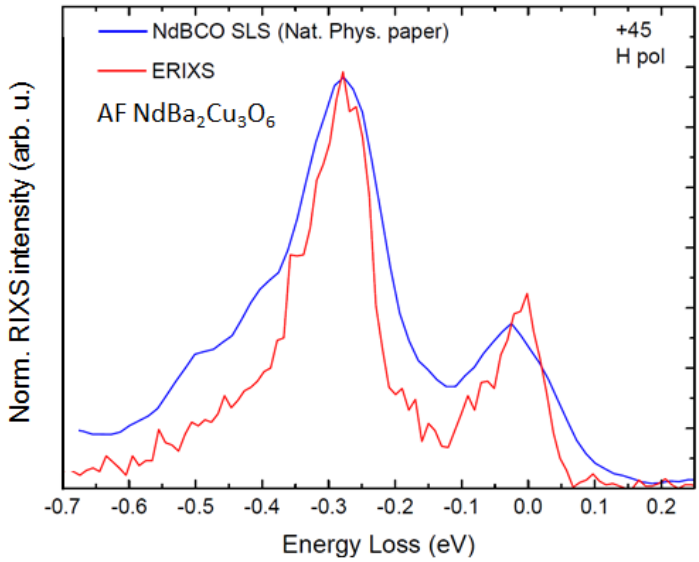

Fig. 3.12: Antiferromagnetic NBCO Cu-L_3 RIXS, at grazing incidence and with π incident polarization. The red spectrum measured at ID32 shows a sharp magnon peak and a phonon as a shoulder of the elastic peak. The blue spectrum was measured with SAXES at SLS in equivalent conditions [17].

In Fig. 3.12 and Fig. 3.13 we show spectra of $NdBa_2Cu_3O_6$ (NBCO), which is the parent compound of an YBCO-like high-T_c superconductor and presents an octahedral symmetry with two CuO_2 planes for each primitive cell. The superior quality of the ERIXS spectra, when compared to equivalent SAXES measure-

ments, is immediately visible in Fig. 3.12: the spin-excitation peak at ~ 0.3 eV is sharper, and next to the elastic peak a second peak becomes immediately visible around 60 meV. This can be assigned to a phonon excitation.

The high resolution also allowed the first observation by RIXS of the magnon optical branch (i.e. gapped at Γ point) of this bilayer compound; this means that a non-negligible interlayer magnetic coupling between the adjacent CuO_2 planes is present [17]. In Fig. 3.13 we show a systematic measurement of the magnon dispersion, obtained acquiring a set of spectra with different in-plane momentum transfer (i.e. by changing the scattering geometry with a sample rotation along the vertical axis). A preliminary fitting of the data according to the model used in Ref. [52] leads to an estimate of the in-plane $J_{//}$ = 136 meV and interlayer $J_{\perp}$ = 6 meV superexchange constants.

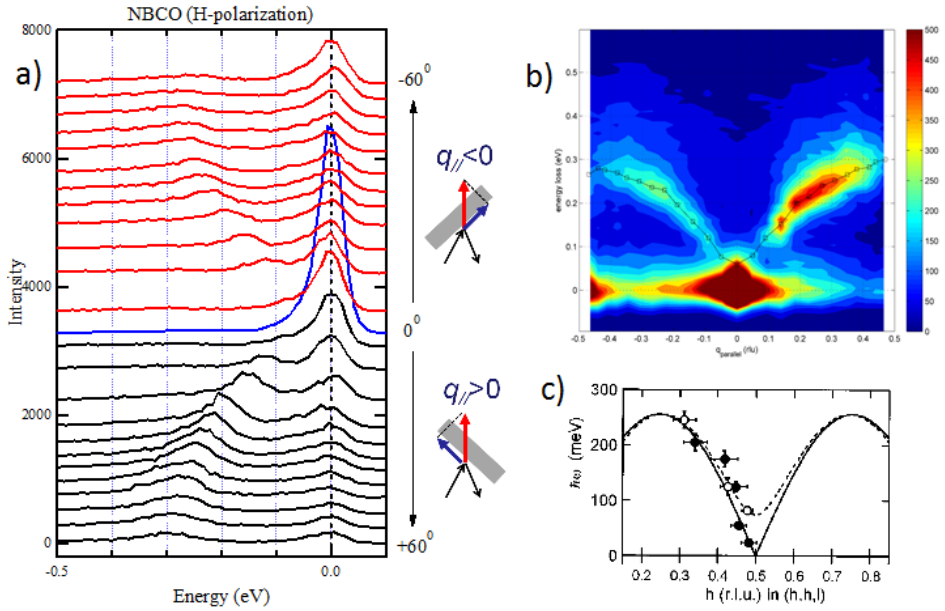

Fig. 3.13: Antiferromagnetic NBCO Cu-L_3 RIXS: (a) stack of RIXS spectra acquired at different scattering geometry (denoted by the δ angle) for positive and negative values of the momentum transfer. The stack is zoomed on the low energy scale, where we note the elastic peak at zero energy loss and a dispersing peak dominated by the single magnon excitation; (b) colormap representation of the energy vs momentum dispersion. At the Γ point the gapped (*optical*) branch has finite energy ~ 60 meV. Data are fitted according to [52]; (c) analogues results from INS [52].

Analogous measurements (here not shown) have been carried out on the infinite layer $CaCuO_2$, suggesting a fully 3D antiferromagnetic order. This was probed measuring a dispersion of the magnetic excitations both in the CuO_2 planes and perpendicularly to them. The latter requires changing the total momentum transfer **q** and not only its projection into the *ab*-planes. The possibility of changing in a continuous way the scattering angle, provided by ERIXS, made this type of measurements possible for the first time.

The azimuthal rotation of the sample holder, provided by the diffractometer sample stage, also allows to measure, for the first time, the dispersion of magnetic excitations along the diagonal direction and the AF Brillouin zone boundary of $NdBa_2Cu_3O_6$, as shown in Fig. 3.14.

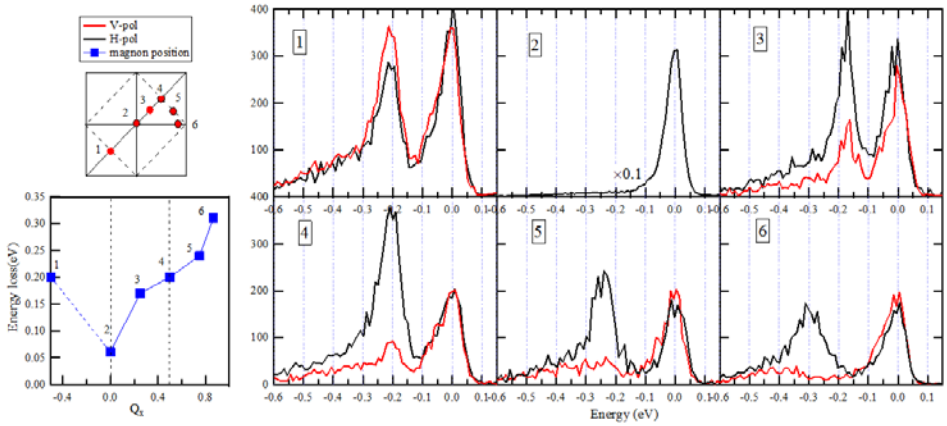

Fig. 3.14: Magnon dispersion along the diagonal direction and the AF Brillouin Zone boundary of antiferromagnetic NBCO. Red spectra are acquired with σ incident polarization, while π was used for spectra in black. The latter have been used for the estimation of the magnon peak position, due to cross-section reasons better explained in Chapter 4.

Preliminary measurements on underdoped and optimally doped YBCO (here not shown) and single layer Bi2201 have also been acquired. In doped cuprates, the spectral features related to magnetic excitations are not resolution limited, as discussed in Chapter 4, therefore the superiority of ERIXS in the study of superconducting samples is more related to sample orientation control, counting time and reproducibility, allowing to perform systematic measurements, rather than in

the improved energy resolution.

A better energy resolution is anyway important to discriminate phonons and other ordering phenomena related peaks, that are expected to sharpen. In Fig. 3.15 we show a false-color dispersion map of underdoped Bi2201. Thanks to the diffractometer, the beam spot on the sample is fixed in the center of rotation throughout the entire measurement; this provides higher quality maps, in which the quasi-elastic charge density wave (CDW) peaks, whose meaning is better clarified in Chapter 6, can be very easily detected around 0.26 r.l.u. (reciprocal lattice units).

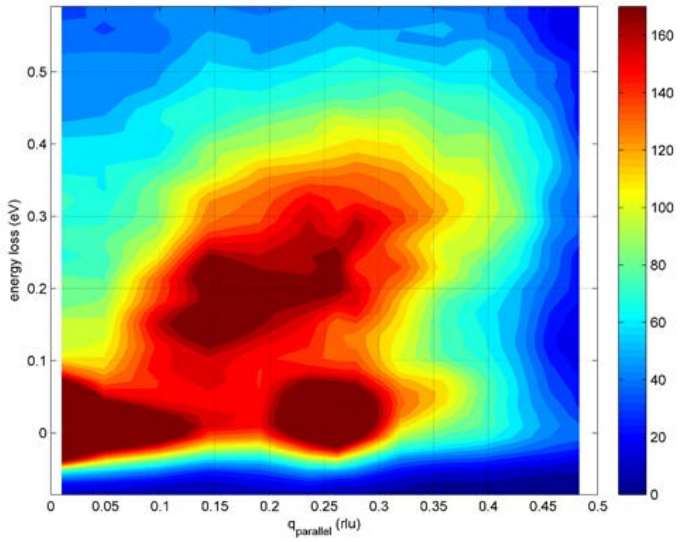

Fig. 3.15: Underdoped Bi2201 Cu-L_3 RIXS, π incident polarization. Colormap of the magnetic excitation dispersion for positive $\mathbf{q}_{\parallel}$ values: a strong CDW is visible close to zero energy loss and $\mathbf{q}_{\parallel}$ = 0.26 r.l.u..

All the measurements shown so far have been acquired in the HE mode. In the following we present some very recent (November 2015) results exploiting the HR mode. To further stress the importance of the advances in energy resolution, we indeed notice that ERIXS is the first soft-RIXS instrument capable of breaking the 100 meV resolution barrier, probing excitations with energies comparable to the gaps generated by collective electronic instabilities (such as superconductivity, charge or spin density waves) in correlated-electron materials.

In our explorative experiments we used HR mode to investigate phonons, linked to lattice excitations in solids. Due to their sharpness, they should be clearly

resolved over the entire region of the reciprocal space accessible to RIXS; this would allow determining their interplay with spin excitations for the first time.

In Fig. 3.16 we show HR RIXS spectra from AF $NdBa_2Cu_3O_6$ and $CaCuO_2$. The energy range is restricted below 100 meV. In both samples one single phonon peak is clearly visible and distinguishable from the elastic line.

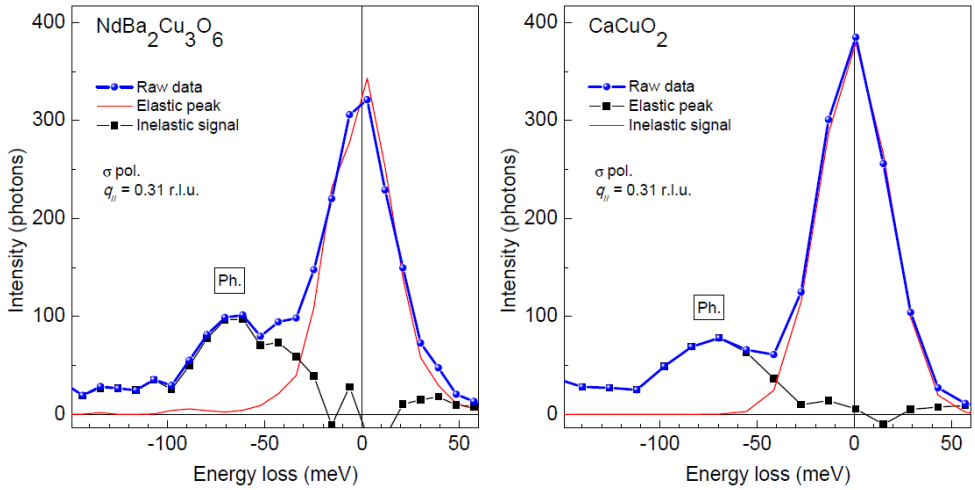

Fig. 3.16: Cu-L_3 HR-RIXS measurements for undoped $NdBa_2Cu_3O_6$ (left) and $CaCuO_2$ (right). Spectra are measured with σ incident polarization at $\mathbf{q}_{\parallel}$ = 0.31 r.l.u.; a resolution limited elastic contribution (red line) have been removed from the raw data (blue line) in order to retrieve the inelastic phonon peak around 60 meV.

During the April-May commissioning we also performed some feasibility measurements from edges different from Cu-L_3, such as: Ni-L_3, Mn-L_3, Ti-L_3, Ce-M_5, Gd-M_5, Eu-M_5. Thanks to ERIXS optimized performances it is indeed possible to exploit soft-RIXS in a wide class of materials, precluded so far mainly due to the weak count rate and the reduced accessible region of the reciprocal space.

The sample cooling was still not available in the commissioning phase; therefore we chose very robust samples that could be investigated at room temperature, like the MnO, NiO, and Gd-Ga garnet. Spectra are shown in Fig. 3.17.

We note that both the intensity and the resolution were still not optimized, also because the central 2.5 m undulator was not in place yet. Despite these limited measurements conditions, the spectra are already very encouraging.

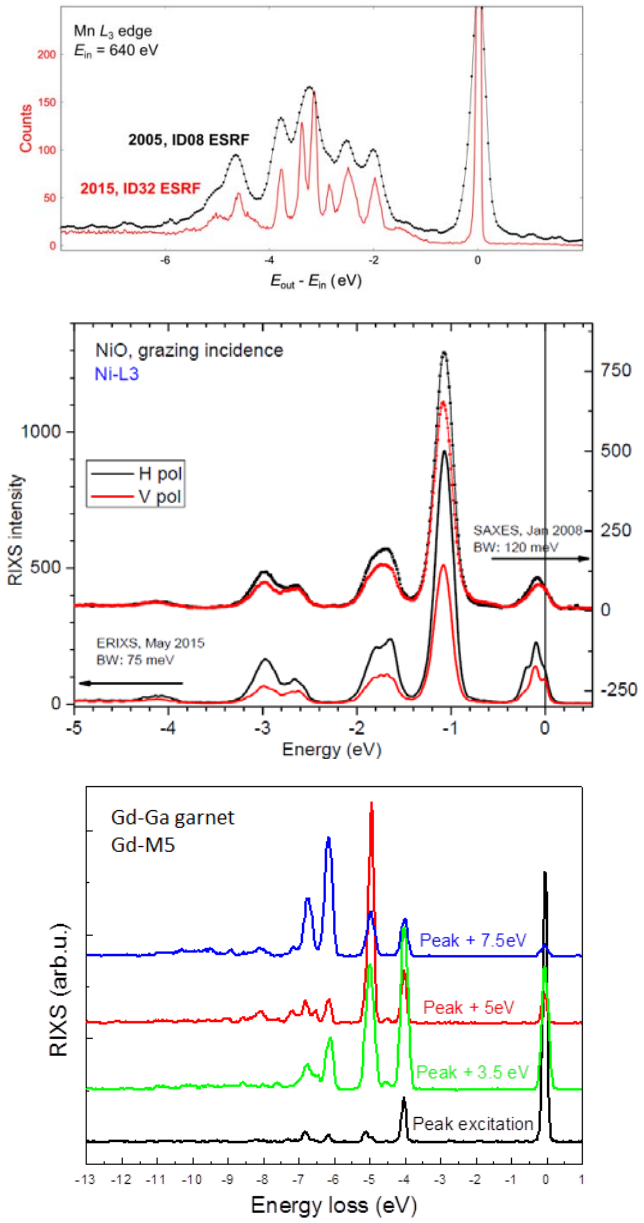

Fig. 3.17: From top to bottom: (i) MnO Mn-L_3 RIXS; data from ERIXS are compared to previous AXES spectra [53] underlining the improved spectrometer performances. (ii) NiO, Ni-L_3 RIXS showing rich *dd*-excitations and a double magnetic peak; ERIXS spectra are compared to those of SAXES [54]. (iii) $Gd_3Ga_5O_{12}$ garnet Gd-M_5 RIXS and detuning effects; spectra show sharp *ff*-excitations compared to Ref. [55].

Once having probed the extraordinary capability of the new ERIXS spectrometer, we can think of many possibilities for high resolution soft-RIXS future trends. Hereafter we list some of them: (i) a systematic study of *dd* and magnetic excitations in HTS cuprates with complete polarization control, disentangling orbital and magnetic excitations from the charge continuum; (ii) observation of charge and/or spin fluctuations exploiting the combination of diffractometer capability in the control of the scattering geometry and increased energy resolution; (iii) a systematic study of phonons in cuprates made with soft-RIXS, possibly providing novel insights into the coupling between magnetic, charge and vibrational excitations; (iv) study of medium- and low-energy excitations in liquids and molecules.

3.3 Polarimetery in soft-RIXS

The data and the analyses presented in this session have been published as part of *"The simultaneous measurement of energy and linear polarization of the scattered radiation in resonant inelastic soft x-ray scattering"* by L. Braicovich, M. Minola, G. Dellea, M. Le Tacon, M. Moretti Sala, C. Morawe, J-Ch. Peffen, R. Supruangnet, F. Yakhou, G. Ghiringhelli and N. B. Brookes, Rev. Sci. Instrum. 85, 115104 (2014).

The AXES spectrometer has been equipped, since 2011, with a multilayered mirror used as a device for polarization analysis of the scattered beam. By combining spectra measured with and without the multilayer, we have demonstrated that it is possible to decompose the RIXS spectra into a crossed and a non-crossed polarization scattering components, directly linked to spin-flip and non-spin-flip magnetic transitions and to different *dd*-excitations.

An evolution of this device has been implemented on the new ERIXS spectrometer, covering the energy range from O-*K* edge to Nd-$M_{4,5}$. With the help of this analyzer, we expect to be able to discriminate the magnon-like peaks from a continuum mainly made of charge and bimagnon excitations. Performing this kind of experiments at several reciprocal lattice points could also lead to a mapping of the charge continuum.

The main difficulty encountered in the polarization measurement of the scattered radiation is given by the necessity to develop a spectral analysis without

losses in the energy resolution. This has been done in the hard x-ray RIXS [56,57] by exploiting the high reflectivity of Bragg optics based on crystals. In the soft x-ray range, the situation is made more difficult by the low efficiency of the available optical elements; in this regime the measurement of the linear polarization of scattered photons has been realized in the past years only in instrumentation with limited or no energy analysis capabilities [58-61].

The polarimeter shown hereafter overcomes these problems. It is based on the idea that the measurement of linear polarization could be directly achieved by exploiting the polarization dependence of reflectivity. This is done in the soft x-ray range by means of a multilayer (ML) mirror.

The polarimeter is added to a traditional RIXS spectrometer just before the CCD camera, as a final optical element, and ideally it deflects the beam without affecting the vertical energy dispersion; it is schematically shown in Fig. 3.18.

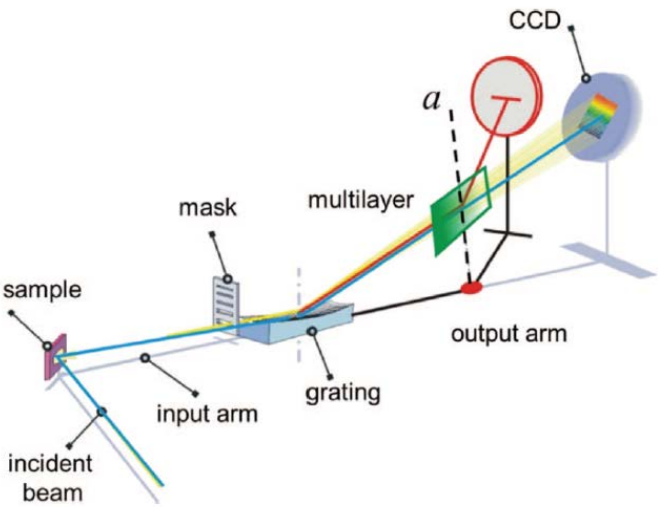

Fig. 3.18: Cartoon showing the insertion of a multilayer (in green) along the spectrometer output arm [51].

It is constituted by a multilayer mirror working in Bragg conditions at the chosen photon energy with intermediate incidence angle, so that the reflectivity is larger for σ' polarization compared to π'. We note that, as convention, we refer to the beam polarization component before (after) the sample with σ and π (σ' and π').

Obviously the reflectivity effect is strongest at 45°, which corresponds to the Brewster angle for x-rays, and lowest at normal and very grazing incidence, but already at ~ 20° from the mirror surface, the polarization dependence of reflectivity is strong enough for our purposes. The system can thus be regarded as a filter with a small efficiency (the average reflectivity of the ML mirror is typically around 10%) and with preferential transmission of the σ' component with respect to π'.

For the analysis of the scattered polarization, two spectra are needed, which should be measured with identical energy resolution and experimental conditions: the spectrum I_D is obtained by the direct detection, while the spectrum I_M is recorded after the ML mirror. These two spectra differ for two reasons: (i) the overall intensity of I_M decreased by the average reflectivity of the ML mirror, and the relative weight of σ' and π' has been modified in the reflection. By properly combining these two spectra, thanks to the accurate knowledge of the ML reflectivity for both σ' and π', it is possible to decompose the spectra recovering the two linear components of the polarization.

From a technological point of view, the most crucial issue in projecting the prototypical polarimeter of AXES was given by the optical matching between the ML and the spectrometer. The horizontal acceptance of the spectrometer is much larger than the angular window accepted by a standard, plane ML, as schematized in the cartoon of Fig. 3.19.

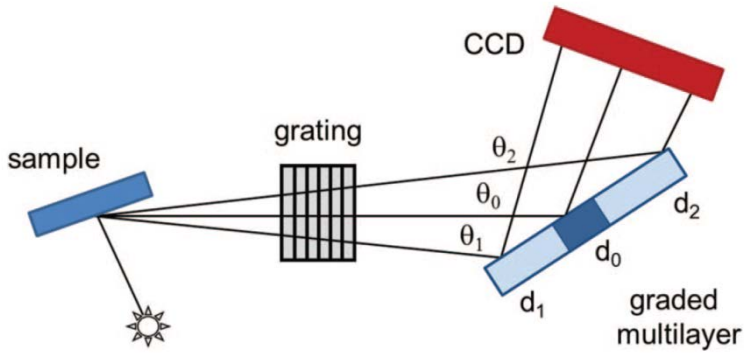

Fig. 3.19: Schematic illustration of the need for a graded multilayer when working with a diverging beam, like in AXES spectrometer [51].

A multilayer with a fixed period d_0 would reflect with good efficiency only from a narrow central area where the incidence angle ϑ_0 is optimized for the selected energy E; due to the beam divergence, the incidence angles on the lateral areas (ϑ_1

and ϑ_2) are different from ϑ_0 and the reflectivity quickly drops, dramatically reducing the detection efficiency. The solution is a ML with a variable *d* spacing in the horizontal direction, so that the same energy is in Bragg condition in each point of the ML along the horizontal fan. This graded multilayer recovers a factor of 4–5 in intensity with respect to a constant-period one.

A further requirement for the ML design is a reflectivity peak as broad as possible, and compatible with an average value not far from 10%. This was obtained on AXES using 150 periods ML made of W and B_4C. The gradient in the direction of the beam footprint is 2.3% and the central spacing is 1.91 nm [62].

Here we report an example of the use of the AXES polarimeter in the study of cuprates. We chose a sample, i.e. underdoped $YBa_2Cu_3O_{6.6}$, and a scattering geometry for which the theory predicts a traditional spectrum given by the superposition of the two outgoing polarizations, both with sizable weights [17,32], as better explained in Chapter 4. The results are shown in Fig. 3.20.

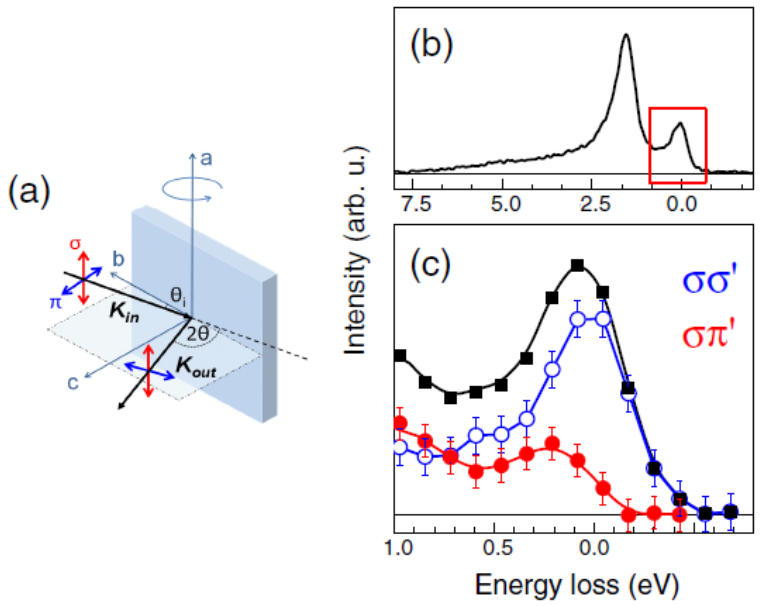

Fig. 3.20: AXES polarimeter results on underdoped $YBa_2Cu_3O_{6.6}$ (hole concentration p = 0.12) at 30° grazing incidence and σ incident polarization. (a) Schematic of the experimental geometry. (b) Traditional spectrum integrated over the outgoing polarization. Spectral region within the red box is expanded in (c) (black squares) giving the decomposition in the crossed (red circles) and non-crossed (blue open circles) polarization components [51].

The low energy scale of the spectrum measured without polarimeter (black) and σ incident polarization have been decomposed in two fully polarized subcomponents: (ii) the σσ' component (blue) contains the elastic peak broadened at the left by a not resolved phonon contribution and a bimagon shoulder around 500 meV, while the crossed component σπ' (red) gives the magnon. The error-bars correspond to the statistical values based on errors propagation through the formulas used to extract the polarized component.

We finally stress that the ration between magnon and bimagnon components are in good agreement with the theoretical model based on a simple local ion picture, developed in Ref. [32].

The main limitation of the AXES polarimeter is the narrow bad-pass (~ 2.5 eV), whose expansion would led to an inacceptable reduction in the efficiency. This problem has been overcome by the ERIXS polarimeter [63].

The new ID32 spectrometer is indeed equipped with a parabolic mirror making the beam horizontal fan collimated. As a consequence, the ML grading in the horizontal direction is no more needed, because all the rays are now impinging at the same angle.

A constant-period ML, optimized for a generic energy E_0, would work as shown in Fig. 3.21.

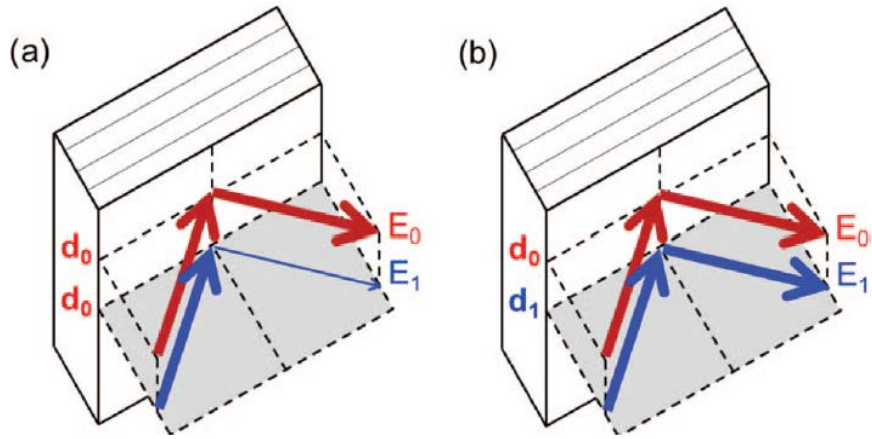

Fig. 3.21: Multilayer top view in the case of a collimated beam (arrows thickness schematize the intensity). (a) Uniform-spacing ML: E_0 is at Bragg condition, while E_1 (with $E_1 > E_0$) is reflected with lower efficiency. (b) Graded ML: thanks to a different period *d*, the response function is almost flat [51].

Due to the dispersing properties of the spectrometer grating, different energies, i.e. E_1 (with $E_1 > E_0$), impinge on the ML at a different vertical position. Then if E_0 is at the Bragg condition for the ML, E_1 will be out of tune and reflected with lower efficiency.

A way to broaden the ML band-pass is thus by tuning the local period of the ML in order to follow the energy dispersion dictated by the grating. This solution is made possible by the use of a graded ML, where the period is now linearly modulated in the vertical direction: this is a dispersion compensating multilayer, with a period gradient along the dispersion direction.

In Fig. 3.22 we show the very first RIXS spectra resolved in scattered polarization by mean of the new ERIXS spectrometer.

In the low energy scale it is clearly decomposed in a crossed contribution σπ' that gives the magnon, and in a non-crossed component σσ', mainly constituted by the elastic peak. Thanks to the increased bad-pass, it is also possible to decompose on a wider energy scale, leading to the separation of the different *dd*-excitations.

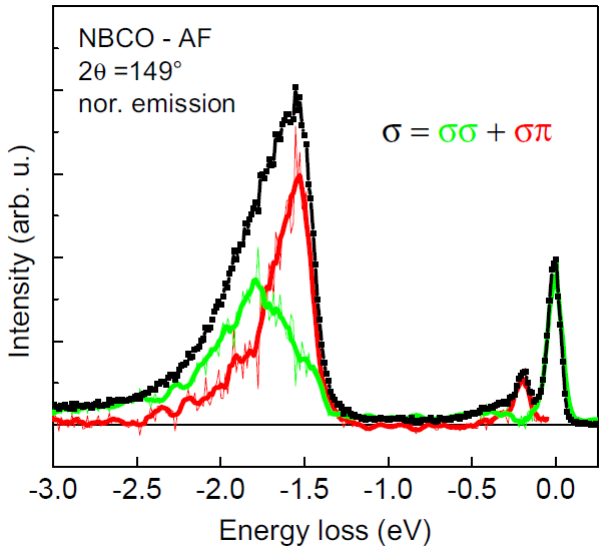

Fig. 3.22: Total RIXS spectra from AF NBCO (black) decomposed in crossed (red) and non-crossed (green) polarization components. Spectra acquired with ERIXS.

As a concluding remark, we would like to stress that very recent approximated theoretical calculations of the RIXS cross-section have shown that, in the cross-polarized channel, on a qualitative level Cu *L*-edge RIXS line shapes correspond to

the spin dynamical structure factor $S(\mathbf{q},\omega)$. However, In the parallel-polarized channel, the situation is more difficult, reflecting the complexity of the RIXS process itself [37,38]. Thus, while line shapes in RIXS should closely resemble charge excitation, a more complicated analysis is required to deeper understand and disentangle the various spectral contributions.

3.4 CCD single photon counting algorithm

The data and the analyses presented in this session have been published as part of "Enhancing spatial resolution of soft x-ray CCD detectors by single-photon centroid determination" by A. Amorese, G. Dellea, L. Braicovich and G. Ghiringhelli, arXiv:1410.1587 (2014).

In ERIXS experiments we can use two identical CCD cameras, one for the direct acquisition and a second one for polarimetric analysis.

As we mentioned before, in Charge Coupled Device (CCD) detectors the absorption of an incoming x-ray photon excites a number of electrons proportional to its energy. These electrons diffuse and generate charge-spots often larger than pixel dimensions. In the soft x-rays this phenomenon drastically limits the effective spatial resolution to approximately 25μm, irrespective of the pixel size.

When the fluency is low enough to be ascribable to the single photon counting approximation, an algorithm for the charge-cloud centroid determination can be used on each individual spot, in order to estimate the actual photon impact position with sub-pixel precision, artificially improving the resolution. The main limiting factors to this procedure in commercial devices are readout noise and speed.

Centroiding procedures have already been used with good result for hard x-rays [64,65], whereas only recently they have been explored in the soft x-ray regime, providing encouraging results [66,67], but an actual evaluation of their improvements in spectroscopy is still missing. Moreover, recent studies are focusing on the use of innovative detectors specifically designed for single photon counting, which provide a shorter readout time with low noise, at the price of a higher cost [68,69].

In the following we show the *in-house* test apparatus that we developed at the Physics Department of Politecnico di Milano in order to probe the potentialities of our Single Photon Counting (SPC) algorithm and improve the related results.

It should be noted that SPC is nowadays the standard procedure for ERIXS CCD images treatment, with an estimated contribution to the spatial resolution of 6-7µm, for ~ 1 keV incoming photon energy.

The *in-house* experimental setup is depicted in Fig. 3.23. A conventional copper anode, producing a continuous spectrum between 500 eV and 2000 eV, has been used as a source, and a collimated beam is obtained with two adjustable slits. Part of the beam is shadowed by a razor blade, located few millimeters before the CCD surface. In this way the straight razor blade profile is projected onto the CCD surface. The width associated to this cut can be fitted with an error-function, whose derivative Gaussian FWHM corresponds to the estimated resolution.

The blurring of the images due to the diffraction from a knife edge was minimized to about 2 µm, by setting the distance blade-camera to 6-9 mm. The broadening due to the residual beam divergence is less than 0.2 µm.

In our test we used two commercial thinned back-illuminated CCD cameras by Roper Scientific [70], with a pixel size of 20 and 13.5 µm respectively. The latter is the one actually used in ERIXS. In order to reduce the dark current to negligible values, CCDs were also cooled down to −60° C and −110° C.

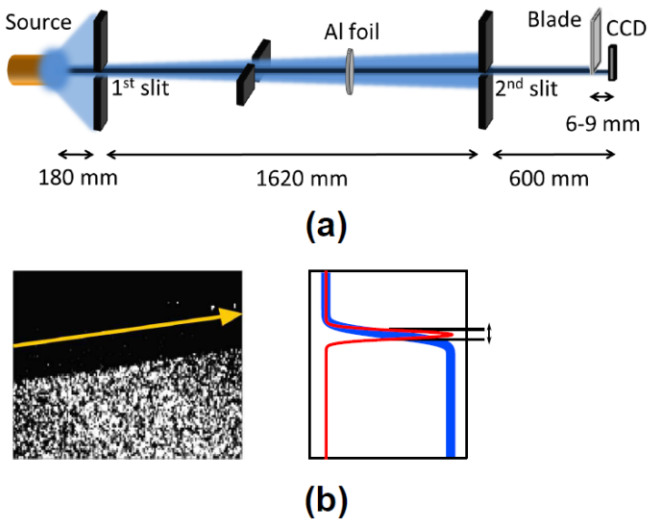

Fig. 3.23: (a) Experimental set-up for SPC tests. (b) Sum over 360 acquisitions of a typical razor blade cut. The image has been integrated along the shadow of razor blade to get the intensity profile, fitted by an error function. The FWHM of the underlying Gaussian function gives the resolution estimation [47].

The SPC algorithm searches the charge-spots on the image and determines the centroids positions by a center of mass calculation. For each spot, the possible central pixels are chosen according to their intensity being included in a range empirically optimized. The centroid coordinates are calculated as first order momentum; they are thus known with sub-pixel accuracy.

A direct comparison between the FWHM of the intensity profile resulting from our algorithm and the one obtained by a simple integration of the pixels intensity without performing the centroid reconstruction provides an estimation of the improved performances in spectroscopic applications.

The results of these experimental tests are shown in Fig. 3.24. They prove a resolution enhancement by a factor ~ 3.5, thanks to centroid reconstruction.

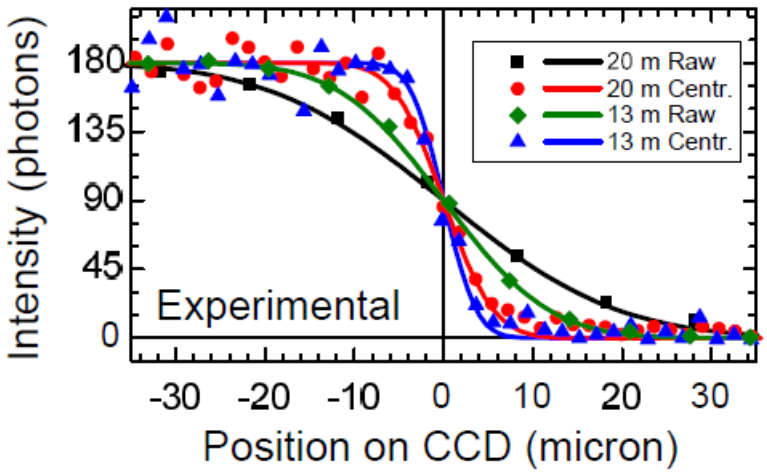

Fig. 3.24: Intensity profiles from experimental images (scatters), without (Raw) and with centroid reconstruction (Centroid). Continuous lines give the error function fits [47].

By analyzing the experimental images without centroid reconstruction, we get a resolution estimation of 36 µm and 22 µm for CCD camera with 20 µm and 13.5 µm pixels size respectively. Both these values differ from the charge-cloud size of 25 µm; this means that other contributions must be taken into account.

When the centroid reconstruction algorithm is used, the resolutions estimated are 9.8 µm and 6.8 µm respectively.

For further improvements of the SPC algorithm, other phenomena should be taken into account, such as the effect of systematic and random noise. These aspects go beyond the phenomenological description provided in this chapter and are addressed elsewhere.

Here we just point out that at present the most important limitation in the application of SPC algorithm comes from the need of isolated charge-spots, which requires, in modern soft x-ray spectrometers such as ERIXS, an exposure time of few seconds. By comparing this time with the detector readout time, i.e. ~ 15-40 seconds for the current CCD cameras, we obtain a very low duty cycle and consequent low photon detection efficiency. A way to overcome this problem consists in the selection of the region of interest (ROI) from the CCD image, containing the interesting energy scale for the sample under investigation.

New generation CCD cameras with higher performances are also envisaged for the years to come to be installed in the ERIXS spectrometer.

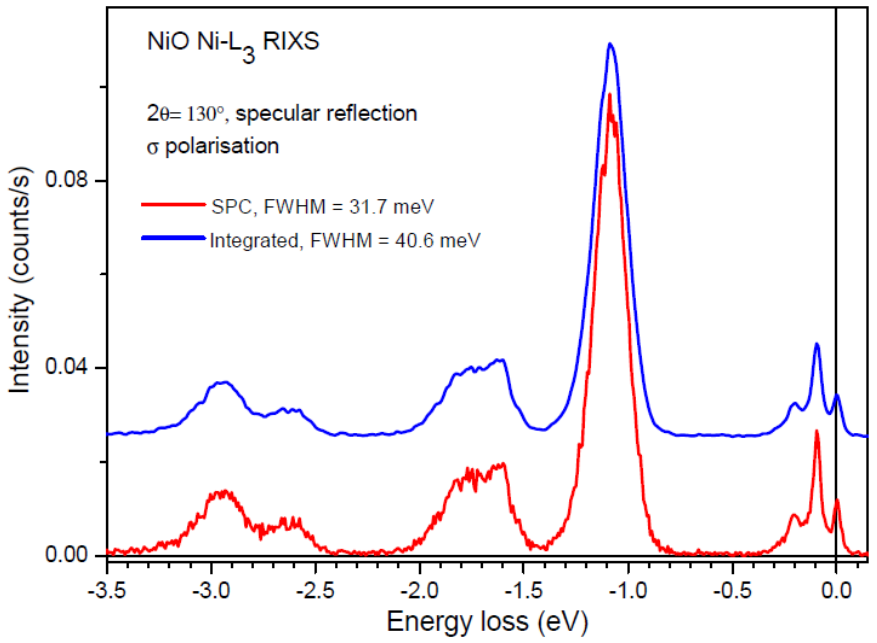

Fig. 3.25: NiO, Ni-L_3 RIXS in HE configuration, showing rich *dd*-excitations and a double magnetic peak. Spectra extracted with traditional integrated algorithm (blu) and SPC (red).

To close this Chapter, in Fig. 3.25 we show a spectrum recently measured with ERIXS in the HE configuration, extracted with both traditional and SPC algorithm.

Compared to the NiO spectra in Fig. 3.17, the HE configuration makes possible to clearly distinguish the two magnetic peaks below 500 meV.

Moving from the traditional integrated algorithm to SPC, we clearly see how resolution limited peaks (i.e. elastic and magnetic) get sharper, while *dd*-excitations width is limited by the intrinsic broadening. By comparing the linewidths of the resolution limited spectral features in the two spectra, we can conclude that the introduction of the SPC algorithm provides an improvement in energy resolution by a factor of $\sim$ 25% at Ni-L_3 edge.

Chapter 4

Ubiquitous magnetic excitations in hole-doped cuprates

As introduced in Chapter 1, since the discovery of high temperature superconductors (HTS), increasing efforts have been devoted to the search of the mechanism at the basis of superconductivity in cuprates, but a conclusive explanation is still unknown [71]. Recent experimental results [17] and theoretical models [72-74] suggest that magnetic excitations can be a good candidate for driving Cooper Pairs formation. In this scenario, a better understanding of the evolution with doping of these spectral features, as well as the development of new families of Cu-based HTS, has become fundamental issues.

In the last years, thanks to high resolution RIXS at Cu-L_3 edge, magnon dispersions have been characterized in undoped insulating cuprates [28,32-34,75,76], while damped spin excitations, the so called *paramagnons*, have been measured in bulk crystals and thin films of hole-doped cuprates, persisting from the superconducting underdoped to the optimally doped samples [14,17,77].

In the present Chapter, after providing a general overview of magnons and paramagnons in cuprates, we show how magnetic-like excitations are indeed an ubiquitous feature in hole-doped cuprates, persisting in a wide range of dopings up to the not superconducting highly overdoped samples, as well as in all the cuprates

families investigated so far, from the well-known bulk crystals and thin films, to more exotic structures (like the superlattices discussed in Chapter 5) down to a few unit cells or nanopatterned samples.

The Chapter also provides an introductory session in which the collective nature of spin excitation will be clarified by recent experimental results.

4.1 Spin excitations: from magnons to paramagnons

In the opening of the Chapter, we briefly recall the work already done with RIXS in the study of magnetic excitations in cuprates, from undoped parent compounds to superconducting and optimally doped samples, in order to get familiar with the problem and with some typical results.

As mentioned in Chapter 2, Cu-L_3 edge RIXS gives direct access to magnetic excitations associated to a spin-flip. We also know that a spin-flip is not an eigenstate of the bidimensional antiferromagnetically ordered CuO_2 planes of layered cuprates. Therefore Cu-L_3 RIXS actually measures spin-waves, i.e. the so called magnons, which are coherent collective magnetic excitations involving more than one site in the same CuO_2 plane. Their collective behavior is probed by the **q**-dependence of the RIXS signal; however for bidimensional systems, such as layered cuprates, the problem can be restricted to the study of the 2D Brillouin Zone (BZ), projecting the momentum transfer onto the sample CuO_2 planes ($\mathbf{q}_{\parallel}$).

In particular, it can be demonstrated that Cu-L_3 RIXS probes magnetic excitations in all cases except the very special one in which Cu spins are aligned along the [001] direction [32]. Moreover, the spin orientation within the *ab*-plane has no influence on the spin-flip cross-section, making simpler to measure the magnon dispersion in samples with multiple magnetic domains.

Before the advent of RIXS, the main technique for investigating the magnetic properties of cuprates was inelastic neutron scattering (INS). Compared to INS, RIXS presents some advantages and complementarities. We briefly recall them: (i) RIXS can be used on tiny amounts of material, while INS works only for massive samples; INS provides an exceptional energy resolution (down to a few meV), but it is mainly restricted to the study of magnetic excitations with low energies (< 200 meV), while RIXS provides spectral information up to high-excitation energies, where the use of neutrons is experimentally very demanding; RIXS also covers a

big area of the 2D-BZ centered around the Γ point, while INS usually reaches only a small area around each corner of the BZ, as shown in Fig. 4.1(b).

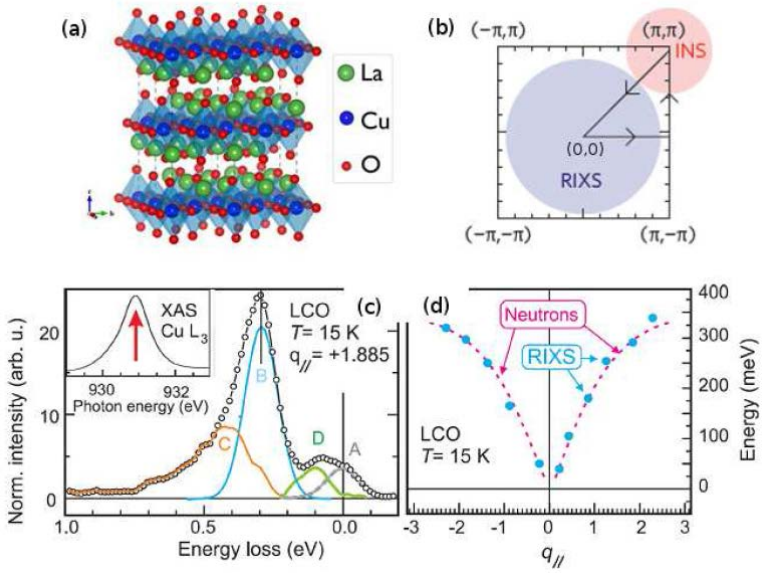

Fig. 4.1: (a) Crystal structure of La_2CuO_4 (LCO) showing octahedral coordination of Cu ions. (b) Accessible regions of 2D Brillouin Zone of cuprates for Cu-L_3 RIXS and inelastic neutron scattering (INS). (c) Decomposition of the RIXS spectrum of LCO at fixed momentum transfer $\mathbf{q}_{\parallel}$ = 1.85 Å, showing spectral features corresponding to: elastic (A), single magnon (B), multiple magnon (C) and optical phonons (D). (d) Single magnon dispersion extracted by various RIXS spectra (blue dots) and determined by INS (dashed purple line from Ref. [79]). Panels (c) and (d) are reproduced from Ref. [33].

The group of prof. G. Ghiringhelli and prof. L. Braicovich first showed in 2009 [33] that RIXS can be used to probe magnons. This was done studying La_2CuO_4 (LCO), which is one of the most extensively investigated cuprates parent compounds and it can be considered as a benchmark. Fig. 4.1 presents a summary of these results.

The spectra have been measured with the standard experimental layout shown in Fig. 3.6. Fig. 4.1(c) shows how the low energy region of a typical RIXS spectrum (from 0 to ∼ 500 meV energy loss) can be decomposed in several contributions, whose origin was determined by studying their dependence upon energy, polarization, scattering geometry and temperature.

In particular, by tracking the energy peak position of the feature B as a function of $\mathbf{q}_{\parallel}$, a symmetric dispersion-like behavior is found, as shown in Fig. 4.1(d). The dispersion curve of peak B follows perfectly the one inferred by INS data for a single magnon [78,79] measured around the AFM (π,π) point, once we report it at the (0,0) point of the BZ, where RIXS works. We note that this is possible because in AFM cuprate parent compounds the magnon dispersions at the center and at the corner of the BZ are superimposable.

This direct comparison confirms that the peak B is a single magnon, and it can be fitted using a Gaussian line-shape with FWHM given by the instrumental resolution (i.e. the broadening due to magnon lifetime is negligible, if any). This result is the first experimental demonstration that Cu-L_3 RIXS is able to probe single magnons in undoped cuprates, and it is supported by the theoretical arguments published in the same year [32].

The other features in Fig. 4.1(c) are assigned to the elastic peak (A) and the optical phonons contributions (D). The former is centered at zero energy loss and its FWHM defines the energy resolution of the measurement, while the latter lies at about 80 meV. The feature C is identified as a bimagnon and its dispersion have been mapped in the reciprocal space for the first time in Ref. [33].

After this first experimental demonstration, RIXS has been extensively used to study magnons on undoped cuprates [34,76,80]. Magnons peak positions and intensities extracted from the data have also been compared to theoretical calculations for the atomic cross sections [23,31]. The agreement of experimental and theoretical results confirmed the assignment of RIXS spectral features to single-magnons and a detailed analysis allows disentangling single-magnon scattering from other spectral contributions.

In particular, single magnons are shown to be enhanced and dominate the low energy spectra, when working around normal incidence conditions with π incident polarization, while non-spin-flip features are stronger with σ polarization. As a consequence, this is the experimental configuration generally used in studying excitations linked to a single spin-flip, as the ones presented in this Chapter. For an exhaustive discussion of the implications connected to the scattering geometry in the determination of RIXS spectral features, we refer to the next session.

We have seen that RIXS can thus probe magnetic excitations and their dispersions in undoped layered cuprates. The following logical step is to apply the same technique to the study of the magnetic excitations evolution upon doping in high-temperature superconductors (HTS).

We should now notice that in all the superconducting samples studied in this Chapter the doping is achieved by adding holes to the electronic bands of cuprates, i.e. we are focusing on the hole-doped region of the phase diagram.

It is commonly believed that each of these doping holes occupies oxygen states and gets delocalized on the four oxygen surrounding the Cu atom in a plaquette. Since the hole in the oxygen has spin in the opposite direction with respect to the one of copper, they cancel out each other and the whole system becomes less magnetic. In that sense, the doping hole can be considered as a magnetic impurity that locally quenches the superexchange, creating a new entity with zero net spin and one more hole called Zhang-Rice singlet [81].

The magnon detection in undoped cuprates parent compounds has thus motivated researchers interest in the investigation of similar excitation is both the undoped [17,28,82,83] and optimally doped region [17,77].

A milestone in this search is constituted by the work done in Ref. [17], where RIXS has been extensively used to show that a large family of cuprates superconductors, from the underdoped $YBa_2Cu_4O_8$ to the overdoped $YBa_2Cu_3O_7$, exhibits damped spin excitations, with dispersions and spectral weights closely similar to those of magnons in undoped cuprates. Due to their nature, these spin excitations have been called *paramagnons*. In Fig. 4.2 typical RIXS spectra from doped samples are shown, together with the estimated peak position and width.

All subsequent studies on hole-doped cuprates present qualitatively the same spectra. Among them we cite $Bi_2Sr_2CaCu_2O_{8-\delta}$ [77], $La_{2-x}Sr_xCuO_4$ [14] and $La_{2-x}Ba_xCuO_4$ [83]. In general, a single not-resolution-limited peak is observed dispersing from $\sim$ 100 meV at $\mathbf{q}_{\parallel}$ = (0.1,0) to $\sim$ 300 meV near $\mathbf{q}_{\parallel}$ = (0.4,0), with a behavior closely similar to what has been shown for La_2CuO_4 [33,79] in Fig. 4.1.

The expression paramagnon derives from the observation that this excitation arises from a state characterized by short range rather than long range magnetic correlations; this explains why paramagnons spectral features possess an intrinsic width, differently from the resolution limited magnons.

The experimental observation of paramagnons in doped cuprates has many important implications. First of all it demonstrates the existence of magnetic correlations up to the optimal doping, better clarifying the normal state from which superconductivity emerges. Before the advent of RIXS, magnetic correlations up to optimally doped cuprates have been already measured by INS, but RIXS has the merit of having expanded the accessible energy range and portion of the reciprocal space.

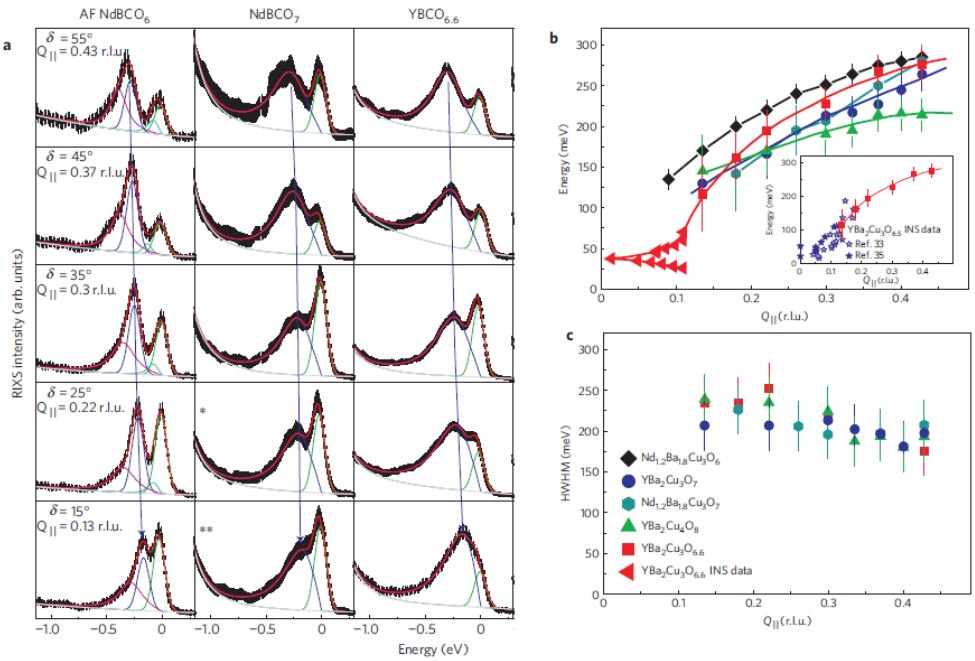

Fig. 4.2: (a) RIXS low energy spectra of undoped antiferromagnetic (AF) $Nd_{1.2}Ba_{1.8}Cu_3O_6$ ($NdBCO_6$) and underdoped $Nd_{1.2}Ba_{1.8}Cu_3O_7$ ($NdBCO_7$), $YBa_2Cu_3O_{6.6}$ ($YBCO_{6.6}$) at various values of the momentum transfer and T = 15 K. The elastic contribution has been fitted with a resolution limited Gaussian. The same fitting function has been used for the magnetic peak of the undoped compound, while broad paramagnons have been fitted with an Voigt profiles that are the result of the convolution of the Lorentzian lineshape of excitations with finite lifetime with the Gaussian resolution function, in order to take into account of the metallic nature of the doped cuprates. The error-bars give the statistical error. (b-c) Experimental paramagnon dispersion along the 100 direction for a wide class of cuprates, as shown in the legend; (b) magnetic peak position and (c) HWHM. Low-frequency INS data recorded along the 100 direction from $\mathbf{q}_{AF}$ for $YBa_2Cu_3O_{6.6}$ have been added for comparison [84]. Solid lines are guides to the eye. Fig. from [17].

Finally, we would like to point out that all the comparisons made so far between INS and RIXS data are based on the assumption that the magnetic dispersion from (0,0)→(0.5,0) is equal to the one from (0.5,0.5)→(0.5,0), which corresponds to assuming that the excitations are equivalent in the full and in the AFM reduced BZ. This is strictly true only in the undoped parent compounds; in fact Γ and $\mathbf{q}_{AF}$ are no longer equivalent in the absence of magnetic long-range order, and

despite RIXS data nicely extrapolate to the low-energy *hour-glass* dispersion around $\mathbf{q}_{AF}$ from INS data, the problem should be treated with caution when adding doping charges to the systems.

4.2 Experimental demonstration of the collective nature of paramagnons

The data and the analyses shown in the following paragraph has been published as part of *"Collective Nature of Spin Excitations in Superconducting Cuprates Probed by Resonant Inelastic X-ray Scattering"* by M. Minola, G. Dellea, H. Gretarsson, Y. Y. Peng, Y. Lu, J. Porras, T. Loew, F. Yakhou, N. B. Brookes, Y. B. Huang, J. Pelliciari, T. Schmitt, G. Ghiringhelli, B. Keimer, L. Braicovich, and M. Le Tacon, *Phys. Rev. Lett*. 114, 217003 (2015).

To realize the potentialities of RIXS as a probe of HTS superconductors and other strongly correlated electron systems, the advances in instrumentation described in Chapter 3 are necessary, but not enough. It is also imperative to develop a reliable quantitative description of the RIXS cross-section.

Initial theoretical work on undoped cuprates suggested that the RIXS intensity can be interpreted in terms of spin-spin correlation functions [22,32,85], in close analogy to what is done for INS. This conclusion is supported by recent numerical calculations of spin excitations in the two-dimensional Hubbard model and for a wide range of dopings. Calculated spectral features are also found to be in good agreement with the magnon-like collective modes measured in the RIXS experiments [37].

This well-established interpretation in terms of collective modes has been widely accepted by the scientific community. But a new theoretical work called it into question during the last year [86]. By taking into account the effect of the core hole created in the intermediate state, they suggested that RIXS data on metallic cuprates can be understood in terms of incoherent particle-hole excitations in a simple non-interacting electron picture.

Benjamin et al. [86] analyzed RIXS with a single-band quasiparticle model, which considers the process where one quasiparticle state is filled by photo-absorption and a different quasiparticle hole is left by re-emission, as explained in

Fig. 4.3(a). They argued that calculated RIXS spectra, using a model of non-interacting quasiparticles but including an interaction with a positively charged core hole and taking into account the spin-orbit splitting of the core level, are able to retrieve a feature corresponding to an intensity peak that disperses to higher energy with increasing momentum. According to the theory presented in [86], if such features are related to a process in which the final state belongs to the particle-hole continuum, by measuring RIXS line shapes for incident energy ω above the absorption maximum, as ω increases line shapes will move to larger Δω, as shown in Fig. 4.3(b). The RIXS signal due to inelastic scattering of a collective mode does not behave this way because Δω cannot exceed the energy of the mode.

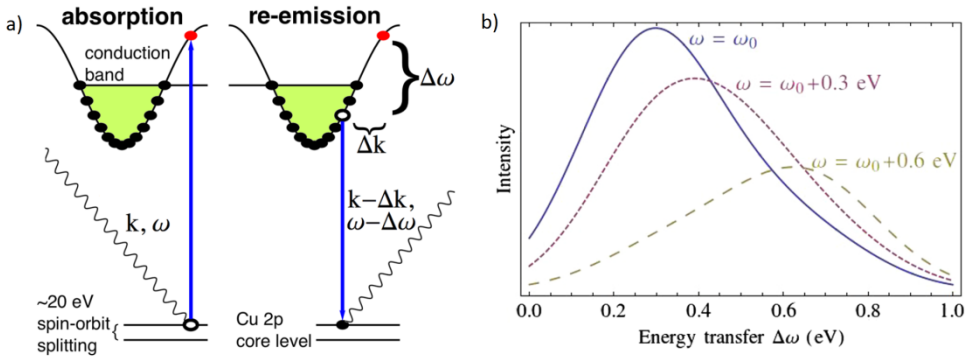

Fig. 4.3: (a) Direct RIXS process that leaves behind a single particle-hole pair, as proposed by Ref. [86]. (b) Calculated intensity vs energy transfer for spin-flip RIXS of optimally doped cuprates, at incident energies 0, 0.2, and 0.4 eV above the absorption maximum according to Ref. [86]. The increase in Δω with ω occurs when the RIXS final state belongs to the particle-hole continuum and does not occur if the final state is an excitation of a collective mode. Fig. from Ref. [86].

In order to resolve this controversy, we decided to exploit the potentiality of RIXS energy dependence. The RIXS profile predicted by Benjamin et al. [86] should shift upon detuning of the incident photon energy from the *L* edge, as we expect for a fluorescence-like excitation in a broad particle-hole continuum, as observed in Chapter 2; while a Raman-like feature, as what we call (para)magnons, is independent of the incoming photon energy.

We have thus experimentally measured the Cu-L_3 edge RIXS dependence on photon energy, from the prototypical high-temperature cuprate superconductor $YBa_2Cu_3O_{6+x}$ ($YBCO_{6+x}$) in both undoped and doped samples.

We find that the energy of the spin excitations does not change with the incoming photon energy at all doping levels. We can conclude that the magnetic signal seen in RIXS experiments arises from the Raman scattering from collective spin excitations, which thus remain a central ingredient for theories of unconventional superconductivity.

4.2.1 Scattering geometry for spin excitation detection

In order to meaningfully perform the detuning experiments, it is necessary to properly choose the scattering geometry for the detection of spin flip excitation. Before presenting the experimental data, we therefore introduce a brief digression, which is of crucial importance for the interpretation of all the data shown in Chapters 4 and 5.

As we already know, a spin flip excitation can take place in *L* edge RIXS, due the strong spin-orbit interaction in the 2*p* intermediate states, that allows the coupling between photon angular momentum and electron spin. Since the total angular momentum has to be conserved during the scattering process, a spin flip necessarily yields a 90° rotation of the scattered beam polarization with respect to the incident one [32]. In other words, when the *c* axis of the crystal lies in the scattering plane, like in typical RIXS experiments on cuprates, a single spin-flip occurs only in the so called cross-polarization channels. So that the best way to discriminate a single spin-flip excitation is to use a polarimeter, as the one shown in Chapter 3.

In the absence of a device for the detection of the scattered beam polarization, it is possible to retrieve the spin-flip information from geometrical considerations. This can be better understood considering the scheme presented in Fig. 4.4, where we show the spin-flip fraction calculated with the simplified RIXS cross sections of Refs. [31,32,34] for $2\vartheta = 130°$.

The blue (red) line represents the spin-flip fraction of the low energy excitation spectral weight for incident π (σ) polarization. For incident π polarization at positive $\mathbf{q}_{\parallel}$, most of the low-energy signal originates from single spin-flip, with a small fraction arising from the non-spin-flip channel. All other scattering geometries probe a mix of spin-flip and non-spin-flip events without analysis of the scattered photon polarization. These incident polarization dependences have been estimated with a simple local ionic picture, and are thus strictly valid only for AFM undoped samples. The possibility to extend them to doped cuprates has been recently supported by numerical calculations [37,87], and has been further confirmed by RIXS polarimetric experiments [51,88], like the one shown in Fig. 4.6.

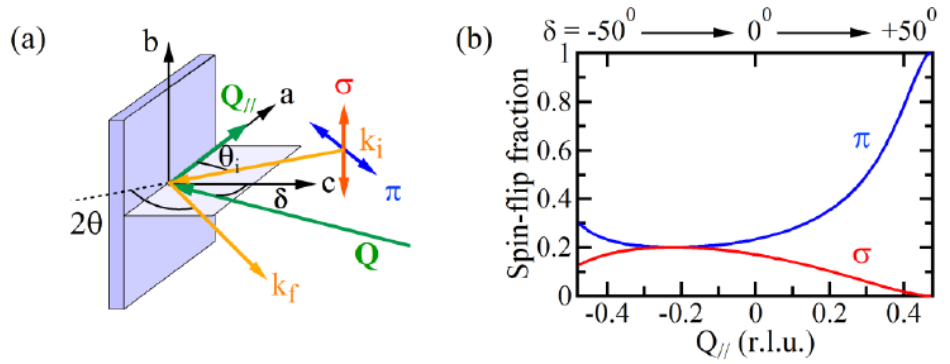

Fig. 4.4: (a) Experimental geometry. (b) Single spin-flip fraction (without orbital excitations) for π or σ polarizations according to RIXS cross section calculations for $2\vartheta = 130°$. Fig. reproduced from Ref. [89]

It should also be kept in mind that the non-spin-flip contribution is spread over several features differing in nature (charge excitations, phonons, diffuse elastic, double spin-flip) and energy, while the single spin-flip channel is mainly concentrated in the (para)magnon peak.

To probe high-energy magnetic excitations close to the Brillouin zone (BZ) boundary (i.e., maximizing the in-plane component $\mathbf{q}_\parallel$ of the total momentum transfer), in principle we can either work with photons near grazing incidence Fig. 4.6(a), $\mathbf{q}_\parallel < 0$ in our convention [17,34,82,90,91], or close to normal incidence with almost grazing emission and $\mathbf{q}_\parallel > 0$, Fig. 4.5(b). These two configurations are probed to be not equivalent. In the latter case, the transition with outgoing π' polarization is dipole forbidden, so that we can only have σσ' or πσ' channels. When the incident beam has σ polarization, the resulting spectrum does not contain single spin-flip contributions, while with incident π polarization the largest fraction of the low energy scale spectral weight is associated to (para)magnons.

This is summarized in Fig. 4.5, where the allowed transitions for $\mathbf{q}_\parallel > 0$ are schematized together with a typical cuprate RIXS spectrum acquired with the two possible incident polarizations. Changes in both the high-energy *dd*-excitations and in the low energy scale of the spectra, on which we will focus from now on, are clearly visible.

These conclusions can now also be experimentally demonstrated with a polarimetric analysis of the RIXS spectra in the discussed configurations, as shown in Fig. 4.6(c-f) for underdoped $YBCO_{6.35}$ and overdoped YBCO+Ca samples.

In agreement with previous experiments [14,17,34,77,82,83,90], the RIXS spectrum acquired with σ polarized light on a very underdoped $YBCO_{6.35}$ shows a strong quasi-elastic line, whereas in the π channel, an intense excitation is seen at around 300 meV energy loss, associated to a paramagnon. The polarization analysis confirms vanishingly small contributions for the π' outgoing component.

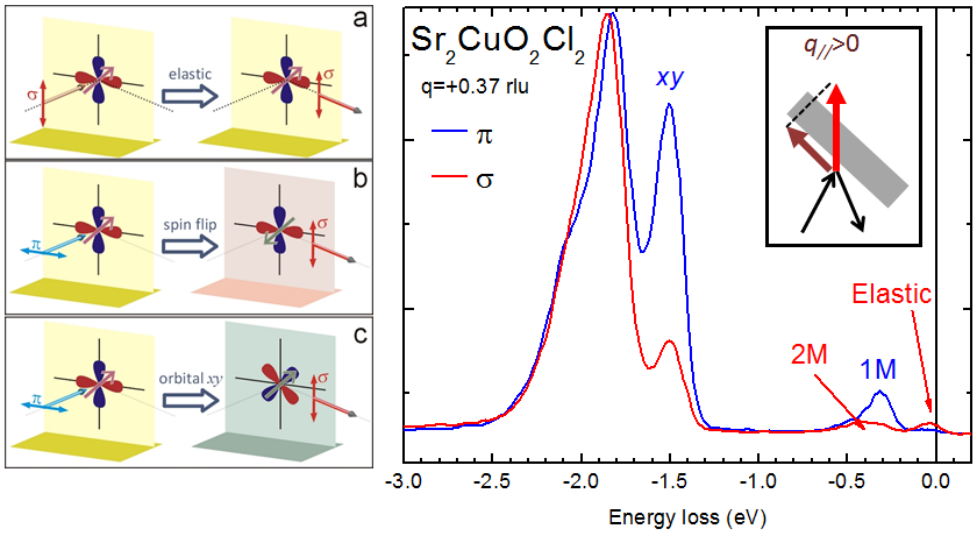

Fig. 4.5: Schematic representation of selected scattering processes in Cu-L_3 edge RIXS, on the left. (a) The polarization is preserved in elastic scattering. (b) A spin-flip process, ultimately leading to a single magnon excitation, must be accompanied by a rotation of the linear polarization vector of the scattered photon; the incident π polarization gets rotated and σ polarization is present in the scattered beam. (c) The *dd*-excitation corresponding to a transition from the ground state with 3*d* hole having x^2-y^2 symmetry to an excited state of *xy* symmetry would be similar [32]. On the right, a typical RIXS spectrum of $Sr_2CuO_2Cl_2$ for $\mathbf{q}_\parallel > 0$ and π (blue) or σ (red) incident polarization is shown. The scattering geometry is reported in the insert. Fig. on the left reproduced from [92].

The same conclusions hold for the overdoped YBCO + Ca sample, except for a large continuum of charge excitations in the σσ' channel, which is summed to the elastic peak. For incident π polarization, most of the low energy signal originates from the πσ' channel, with only a small fraction arising from the non-spin-flip ππ'.

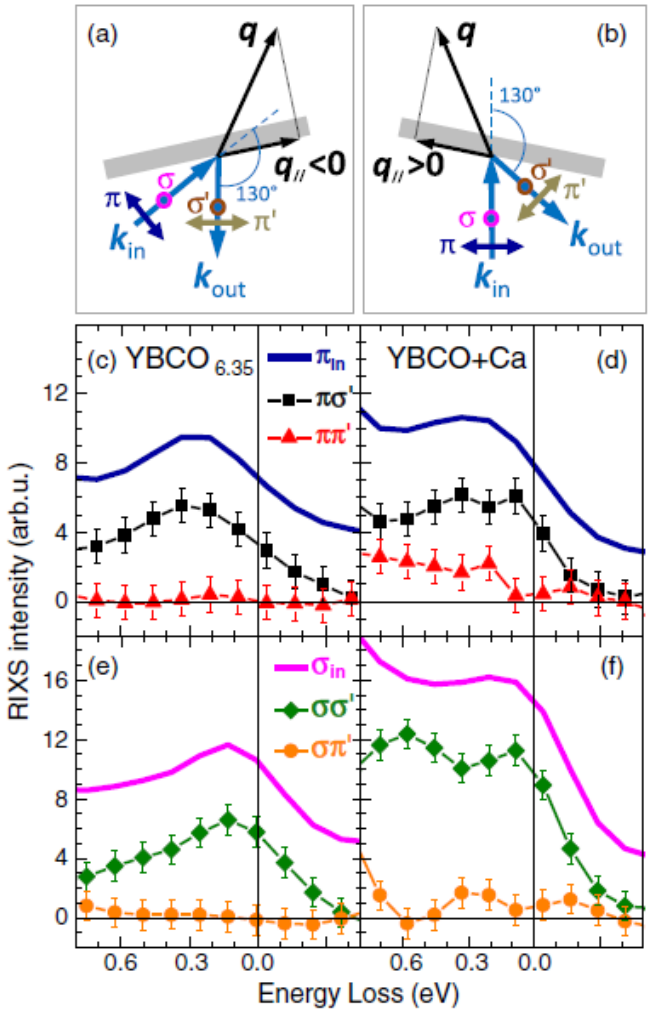

Fig. 4.6: (a-b) Scattering geometries scheme, maximizing the momentum transfer with (a) grazing incident photons or (b) grazing emitted photons. (c-f) Polarization resolved measurements of underdoped $YBCO_{6.35}$ taken with incident π (c) and σ (e) polarized light, and overdoped YBCO + Ca with incident π (d) and σ (f) polarized light. Spectra acquired with incoming photon beam at 20° from normal incidence, i.e. $\mathbf{q}_{\parallel} > 0$ and close the BZ X point. Spectra acquired with AXES spectrometer at ID08 – ESRF, with a combined resolution of 350 meV FWHM [88].

Having firmly established grazing emission (i.e. $\mathbf{q}_{\parallel} > 0$ and close to the X point of the BZ) and π incident polarization as the optimal geometry for the investigation of magnetic excitations with RIXS, we can analyze the energy dependence of these features to discriminate between a collective and fluorescence like behavior.

4.2.2 Experimental

The RIXS experiments have been performed at the ADRESS beamline of the SLS with the SAXES spectrometer. The combined instrumental resolution is 160 meV. The standard scattering geometry has been used, in the particular configuration described in the previous session.

A systematic investigation has been performed on various single crystals of $YBCO_{6+x}$, spanning the entire phase diagram from the nearly undoped to the overdoped regimes, with: x = 0.1, 0.35, 0.55, 0.79, to 0.99, plus a Ca-doped sample ($Y_{0.85}Ca_{0.15}Ba_2Cu_3O_{6+x}$). The resulting spectra, obtained by changing the incoming photon energy from the Cu-L_3 absorption edge, are summarized in Fig. 4.7.

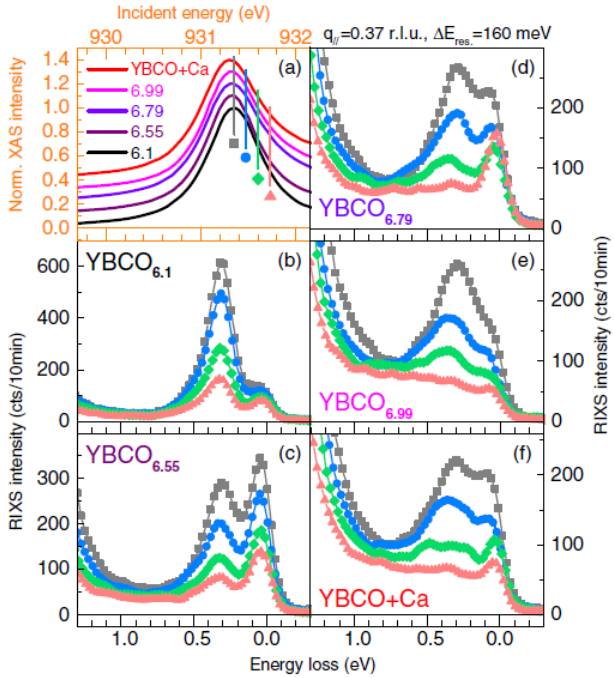

Fig. 4.7: RIXS spectra measured with π polarization and excited at selected incident energies across the corresponding Cu-L_3 edge XAS profile [88].

For all the investigated doping levels, from the raw data the energy of the magnetic peak appears not to change while tuning the incident photon energy. This is in stark contrast with the spectra behavior observed in the σ channel, which is shown in the color maps of Fig. 4.8, where the RIXS signal is plotted as a function

of the incident photon energy above the L_3 edge (931.35 eV) for the two extreme doping levels investigated (antiferromagnetic $YBCO_{6.1}$ and overdoped YBCO + Ca).

In the magnetically ordered compound, a stronger quasi-elastic line and a bimagnon signal are visible in the σ channel. Similarly to the single spin-flip seen in the π channel, the bimagnon energy does not depend on the incident photon energy.

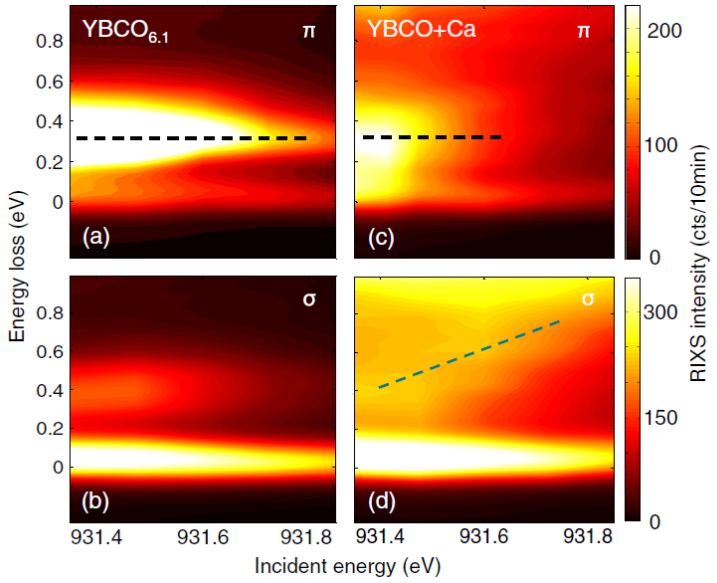

Fig. 4.8: Energy dependence of the RIXS intensity for AFM $YBCO_{6.1}$ (a,b) and overdoped YBCO + Ca (c,d) with π (a,c) and σ (b,d) incident polarizations [88].

In the overdoped compound with incident σ polarization, the bimagnon excitation cannot be resolved, but a strong charge continuum is visible and it clearly exhibits a fluorescent behavior.

By a deeper investigation of the π map for the overdoped samples, we can argue that the spectra seem presenting also a weak fluorescent like component superimposed to the collective excitation. This is confirmed from very recent systematic detuned RIXS data on slightly and highly overdoped Tl2201 and Bi2201 cuprates, here not shown.

From our preliminary analysis, we can anticipate that the collective behavior of the magnetic peak is confirmed up to optimal doping in both cuprate families, as already seen for YBCO. However, when moving to the highly overdoped side of the

phase diagram, the magnetic peak progressively starts to shift with incident energy, as a fluorescent signal. This agrees well with a picture of correlations persisting up to high doping, and just beyond optimal doping there seem to be a crossover such that at extremely high doping levels the system behaves as a weakly correlated metal.

4.2.3 Discussion

Our RIXS measurements confirm the presence of collective spin excitations associated with short-range antiferromagnetic correlations in doped high-T_c superconductors up to optimal doping at least, while a crossover from a collective like to a fluorescence like behavior is likely to happen when moving to very high overdoped systems; the latter requires further investigations.

Our results on optimally and slightly overdoped cuprates are also consistent with recent theories describing the RIXS cross section in terms of a spin-spin correlation function [37,85], avoiding the necessity of materials-specific numerical simulations in order to properly interpret RIXS data.

Given the above considerations, a further enhancement of the instrumental energy resolution, and the systematic use of polarization analysis of the scattered photons, would definitely lead RIXS to become the primary probe for dispersive spin excitations in a wide variety of structures.

4.3 Paramagnons up to overdoped cuprates

The data and the analyses shown in the following paragraphs have been published as part of *"Persistence of magnetic excitations in $La_{2-x}Sr_xCuO_4$ from the undoped insulator to the heavily overdoped non-superconducting metal"* by M. P. M. Dean, G. Dellea, R. S. Springell, F. Yakhou-Harris, K. Kummer, N. B. Brookes, X. Liu, Y-J. Sun, J. Strle, T. Schmitt, L. Braicovich, G. Ghiringhelli, I. Božović and J. P. Hill, Nat. Mater. 12:3723 (2013); and *"High-energy magnetic excitations in overdoped $La_{2-x}Sr_xCuO_4$ studied by neutron and resonant inelastic x-ray scattering"* by S. Wakimoto, K. Ishii, H. Kimura, M. Fujita, G. Dellea, K. Kummer, L. Braicovich, G. Ghiringhelli, L. M. Debeer-Schmitt, and G. E. Granroth, Phys. Rev. B 91, 184513 (2015).

As anticipated before, during the last 30 years, many different scenarios have been postulated in order to explain high temperature superconductivity (HTS) in cuprates. Among them, pairing by exchange of magnetic excitations was definitely one of the most intensely studied [72]. Spin excitations have indeed been observed persisting from the undoped parent compound up to optimal doping [17,93-97]. On the contrary, in the heavily overdoped regime, neutron scattering measurements indicate that magnetic excitations disappear [98–100], and this has been argued to cause the decrease and subsequently expiration of HTS with doping levels progressively exceeding the optimal value [72,99,100].

In order to confirm this assumption, we used resonant inelastic x-ray scattering, which is a complementary technique for INS, to measure the evolution of magnetic excitations in $La_{2-x}Sr_xCuO_4$ across the entire phase diagram, from a strongly correlated insulator (x = 0) to a non-superconducting metal (x = 0.40). In the absence of a universally accepted theory of high-T_c superconductivity, it is indeed essential to consider the excitation spectrum over the whole Brillouin Zone.

For x = 0, well-defined magnon excitations are observed [78]. For increasing doping, these magnetic excitations broaden, but they persist with a similar dispersion and comparable intensity in the entire doping range under investigation, up to the heavily overdoped metallic phase.

The destruction of HTS with overdoping is therefore not simply explained in terms of a general disappearance of magnetic excitations. Other factors, such as the redistribution of spectral weight or the interconnection with other ordering phenomena, must be considered.

4.3.1 Experimental: $La_{2-x}Sr_xCuO_4$ along (0,0) → (0.5,0)

Cu-L_3 edge RIXS experiments have been performed using the AXES spectrometer at the ID08 beamline of the ESRF. The data reported here have been acquired with incident π polarization, and high values of the momentum transfer $\mathbf{q}_{\parallel}$ corresponding to x-rays that leave the sample at grazing angles, i.e. using the standard scattering geometry introduced in Chapter 3 and well known for increasing the sensitivity to the spin-flip spectral features.

The combined resolution function of the monochromator and the spectrometer is approximately 260 meV at FWHM. All the data have been collected at T = 25 K.

The investigated samples are $La_{2-x}Sr_xCuO_4$ thin films with x = 0, 0.11, 0.16, 0.26 and 0.40 respectively. These doping levels have been chosen in order to span the entire $La_{2-x}Sr_xCuO_4$ phase diagram, as shown in Fig. 4.9(a).

The main advantage of using thin films, instead of bulk samples, is given by the presence of atomically smooth surfaces, i.e. the root mean square roughness measured by atomic force microscopy corresponds to a few Å. This has been probed to reduce the diffuse elastic scattering contribution [22].

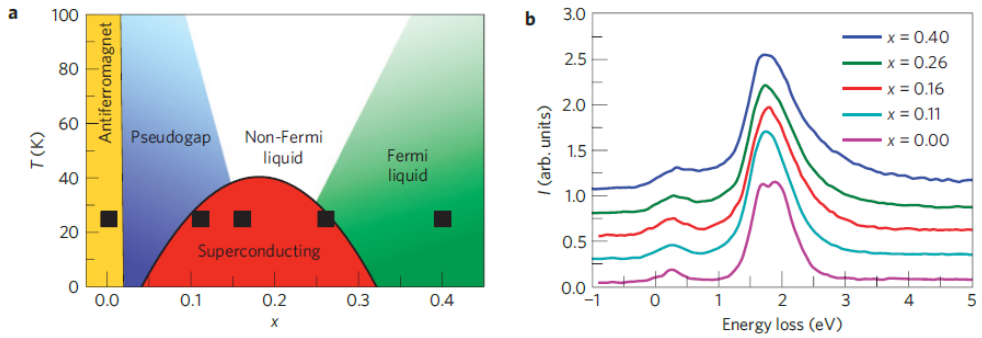

Fig. 4.9: (a) Schematic phase diagram for $La_{2-x}Sr_xCuO_4$ as a function of x. The superconducting (SC) and antiferromagnetic (AF) states are retrieved from Ref. [101]. Black squares mark the doping levels under investigation and the measurements temperature. (b) Typical RIXS spectra of $La_{2-x}Sr_xCuO_4$ at fixed momentum transfer $\mathbf{q}_{\parallel}$ = (0.36,0) and for different doping levels. The peaks in the 1–3 eV energy window corresponds to the *dd*-excitations, whereas the low-energy peak around 300 meV arises from magnetic scattering. Fig. reproduced from [14].

Typical RIXS spectra for $La_{2-x}Sr_xCuO_4$ films are shown in Fig. 4.9(b). They are dominated by *dd* orbital excitations, whose peaks lie in the 1-3 eV energy window. As mentioned before, these excitations correspond to a transition in which the valence band hole, primarily of Cu d_{x2-y2} character, is promoted into higher energy orbitals [102]. Since the determination of the absolute scattering intensity is not trivial in RIXS experiments, and the overall intensity of *dd*-excitations is almost constant when changing the scattering geometry, these features are often used in data analysis as references [34].

In the mid-infrared energy scale (50-500 meV) single spin-flip excitations can be observed [32,85]. At higher energy loss, a broad and flat background arises from charge-transfer (CT) excitations of the Cu d_{x2-y2} hole into the O 2*p* states.

When the doping content x increases, the *dd*-excitations broaden. This suggests hybridization between the *d* orbitals and the itinerant states of doped holes, i.e. the so called ZR singlets appear. Doping charges thus create an intensity tail ex-

tending into the mid-infrared region.

We now focus on the low energy scale of the RIXS spectra. Fig. 4.10 shows a summary of the data acquired for all the available dopings while spanning the in-plane momentum transfer from $\mathbf{q}_{\parallel}$ = (0,0) to $\mathbf{q}_{\parallel}$ =(0.4,0), i.e. covering up to 80% of the 2D Brillouin Zone, along the (0,0) → (0.5,0) direction of the reciprocal space.

Close to the Γ point, the spectra are dominated by the strong specular elastic scattering. At higher $\mathbf{q}_{\parallel}$ a second peak becomes visible around 300 meV. Following the results presented at the beginning of this Chapter, for the undoped (x = 0) sample this peak can be easily assigned to a magnon [28,34,82], which has also been previously observed by inelastic neutron scattering [78].

We now consider the spectra for higher doping levels; we already see from the raw data that the so called magnon smoothly broadens with increasing doping and persists as a paramagnon across the entire $La_{2-x}Sr_xCuO_4$ phase diagram, retaining its spectral feature also in the heavily overdoped metallic region. This observation, in stark contrast with our expectations, opens new challenging questions about the relation between the observed paramagnon behavior and HTS in cuprates.

In order to retrieve more quantitative information, the spectra have been properly fitted using the approach shown in Ref. [17]. The total spectrum is given by the sum of three functions; each of them accounts for (i) the elastic scattering, (ii) the smooth background and (iii) the magnetic contribution.

The elastic peak is fitted with a resolution limited Gaussian, i.e. FWHM = 260 meV, which is a good approximation for the instrumental resolution function. The background coming from the charge-transfer and the tail of the *dd*-excitations is schematized with a smooth line, and the paramagnon is fitted with an anti-symmetrized Lorentzian function, in order to take into account the Bose factor.

Due to the limited energy resolution and to the intrinsic broadening of the magnetic excitations in doped samples, it was not possible to separate the contributions given by phonons and multi-spin-flip scattering from the paramagnon [17,77]. It should also be reminded that this leads to a slight overestimation of the width and the intensity of the magnetic peak [17]. We finally note that at the highest doping the paramagnons become extremely broad and fitting becomes really challenging, bringing to further uncertainties.

Fitting results are summarized in Fig. 4.11. We note that the dispersion of magnetic excitations is unchanged, within the scatter of the data points.

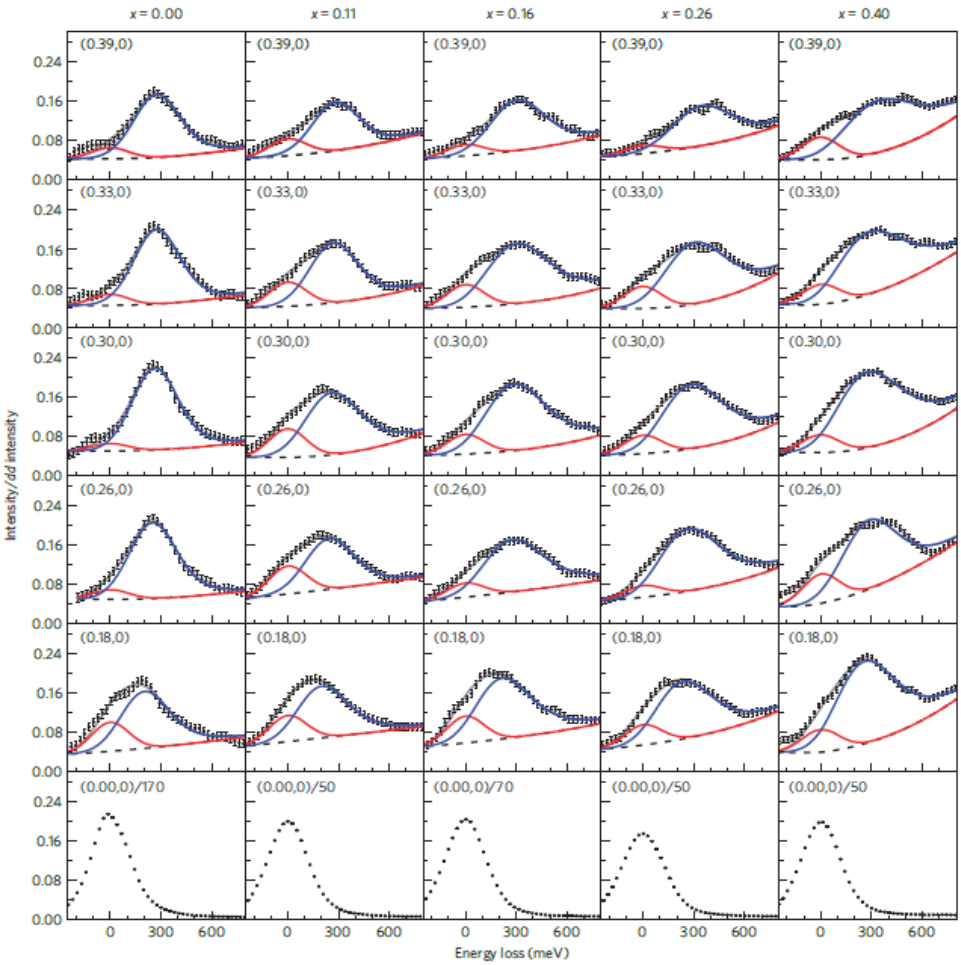

Fig. 4.10: Magnetic excitations dispersion in $La_{2-x}Sr_xCuO_4$ as function of $\mathbf{q}_{\parallel}$ and x. The filled black circles represent the experimental data and the solid grey line shows the results of the fitting, obtained by the sum of a resolution limited elastic contribution (red), an anti-symmetrized Lorentzian convolved with the experimental resolution (blue), which describes the magnetic scattering, and the background coming from *dd*-tails and CT (dashed black). At $\mathbf{q}_{\parallel}$ = (0,0), magnetic excitations cannot be observed due to the very strong elastic scattering, and the peak shape primarily reflects the experimental resolution function. The intensities are presented after being normalized to the spectral weight in the 1–3 eV region containing the *dd*-excitations. The spectra at $\mathbf{q}_{\parallel}$ = (0,0) have been divided by the factors indicated on the plots, in order to make them visible on the same scale. Error bars indicate the magnitude of the statistical variations in the summed spectra. Fig. from [14].

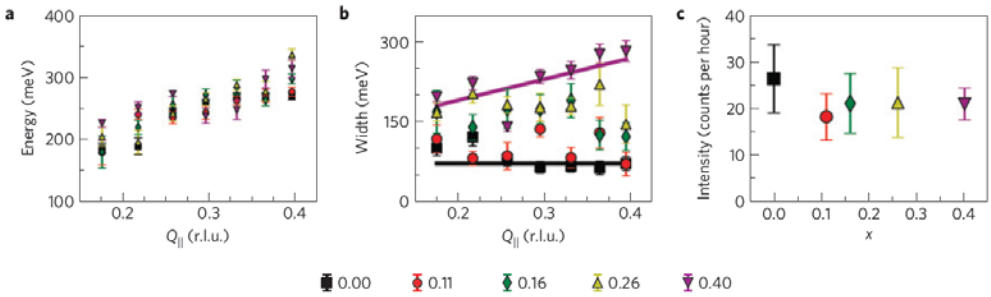

Fig. 4.11: (a) Energy dispersion of the magnetic excitations along the reciprocal space direction **q** =($\mathbf{q}_{\parallel}$,0). The magnetic excitation energy does not change significantly with doping. (b) Half-width at half-maximum (HWHM) $\mathbf{q}_{\parallel}$ dependence of the magnetic excitations; black and purple lines are guides to the eye, corresponding to the data with x = 0 and x = 0.40 respectively. (c) RIXS intensity of the magnetic excitations averaged over the measured $\mathbf{q}_{\parallel}$. Within the errors, the intensity of magnetic excitations is conserved with increasing x. The error bars represent the uncertainty in the fitting procedure. Fig. from [14].

In contrast, the width of the excitations increases dramatically with doping. This damping has been tentatively interpreted in terms of a coupling and consequent decay of the magnetic excitations into Stoner quasi-particles as low-energy electronic states becomes available.

4.3.2 Discussion: $La_{2-x}Sr_xCuO_4$ along (0,0) → (0.5,0)

The most important implication of our RIXS measurements is the observation of a substantial magnetic correlation persisting up to overdoped cuprates in the entire region of the reciprocal space under investigation.

Overdoped cuprates are thus not simply non-magnetic metals, and paramagnons measured with RIXS retain almost unchanged energy and spectral weight, while the doping increases and the superconductivity disappear. The change in T_c is thus most likely driven by other factors, such as the low-energy magnetic excitations which instead have been proved to change dramatically in the overdoped cuprates [98-100].

Our results on $La_{2-x}Sr_xCuO_4$ samples show an increase of the magnetic peak width with doping, since more electronic states become available for the scattering process. This finding is confirmed by measurements spanning the underdoped and slightly overdoped regions of the phase diagram in other cuprates families,

such as neodymium yttrium [17] and bismuth [77] based samples. Widths comparable to the ones of our overdoped samples are also found in recent results on Tl-based cuprates [90]. This may imply that the increasing in width is primarily determined by the hole concentration level rather than possible structural disorder induced by doping, which is expected to be more sample dependent.

Remarkably, the paramagnon excitation also exhibit comparable RIXS intensity across the entire phase diagram, up to the heavily overdoped region.

These results should also be considered in light of other probes of magnetic excitations. In particular, RIXS has been mainly used to measure the (0,0) → (0.5,0) high symmetry line, while less is known regarding the RIXS spectra behavior along the other primary symmetry direction (0,0) → (0.5,0.5). Unfortunately, state of the art RIXS cannot reach the antiferromagnetic scattering vector (0.5,0.5) for undoped cuprates, where INS measurements are mainly focused. On the other hand, the magnetic signal along the (0,0) → (0.5,0) is usually below the signal-to-noise ratio for neutrons, making the two techniques strongly complementary.

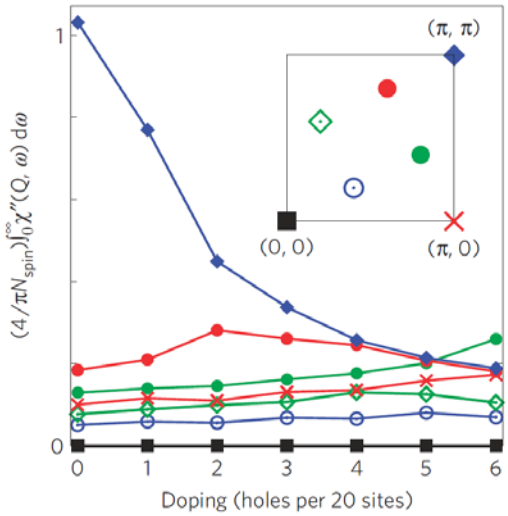

Fig. 4.12: Imaginary part of the energy-integrated spin susceptibility plotted as a function of doping, as derived from exact-diagonalization calculations of the t-*J* Hamiltonian with exchange coupling constant *J* =0.3t on finite-sized clusters. The seven accessible non-equivalent **q** vectors are shown in the inset [17].

Putting together RIXS and INS data, we infer a not uniform attenuation of the magnetic excitations upon doping; in particular, the high energy excitations along

(0.18,0) → (0.4,0) remain relatively constant, while low energy excitations close to (0.5,0.5) are strongly reduced.

Finally, we would like to point out that although the paramagnon behavior probed by RIXS in overdoped cuprates is somehow unexpected in the light of INS results, the phenomenology shown so far is actually predicted by recent theoretical calculations based on a single band Hubbard model [37].

The inconsistency between INS and RIXS data is actually just apparent, due to the capability of traditional INS measurements to cover only a small fraction of the energy and momentum space associated to spin-flip excitations, mainly in the proximity of $\mathbf{q}_{AFM}$. Previous numerical calculations for the t-*J* model [17], Fig. 4.12, have already argued that the intensity in the undoped region is strongly peaked at $\mathbf{q}_{AFM}$, and fairly uniformly distributed in the rest of the plane. However, as holes are added to the clusters, the magnetic spectral weight strongly decreases only around $\mathbf{q}_{AFM}$, and remains essentially constant everywhere else, accordingly to our results.

4.3.3 Experimental: $La_{2-x}Sr_xCuO_4$ along (0,0) → (0.5,0.5)

In the second part of this session, we would like to show some more recent results on overdoped $La_{2-x}Sr_xCuO_4$ single-crystals. The combination of INS and Cu-L_3 edge RIXS techniques, together with the improved experimental performances have allowed to overcome the main limitations discussed in precedent investigations on overdoped cuprates, retrieving a general description for RIXS and INS.

Our starting point was thus provided by the mentioned above systematic studies of paramagnons in the hole-doped YBCO [17] and LSCO [14] family compounds. These investigations have revealed high energy magnetic excitation with a dispersion relation along the (0,0)→(π,0) direction independent of the hole concentration in a wide doping range, contrary to neutron results in the low-energy region.

We also remind that RIXS and INS are usually considered as complementary measurements technique. Traditional RIXS, due to the limited wave vector of the incident photons in the soft x-ray regime, and its relatively large energy resolution is more appropriate for the detection of magnon excitations above 100 meV and dispersing from the (0,0) position. In contrast, neutron scattering has a fine energy resolution, typically a few meV, which makes difficult to observe high-energy magnetic excitation, and consequently, neutron inelastic scattering is suitable for the observation of magnetic excitations below 150 meV, dispersing from the antiferromagnetic (AF) zone center (π,π).

We now show that we were able to probe high energy magnetic excitations (> 100 meV) in two over-doped $La_{2-x}Sr_xCuO_4$ single crystals, with x = 0.25 (Tc = 15 K) and x = 0.30 (non-superconducting) respectively, along both the (0,0)→(π,0) and the (0,0)→(π,π) directions of the reciprocal space, reconciling the apparent discrepancies found in previous session.

In particular, INS measurements of high energy magnetic excitations, up to ∼ 250 meV for x = 0.25, were made possible by the use of a spallation source and were performed at the Spallation Neutron Source (SNS) at Oak Ridge National Laboratory (ORNL). The resulting peak positions along the (0,0)→(π,π) direction are summarized in Fig. 4.14. They agree with the dispersion relation of the spin wave in the undoped La_2CuO_4 (LCO). This result is consistent with the previous RIXS studies of cuprate superconductors.

Cu-L_3 edge RIXS experiments were performed using the AXES spectrometer at the ID08 beam line of the European Synchrotron Radiation Facility (ESRF), with a combined energy resolution of 290 meV FWHM. The incident photon polarization was set either horizontal (π polarization) or vertical (σ polarization) to the scattering plane, and the samples were aligned on the sample holder with either the [1,0] or the [1,1] axis horizontal, in order to enable the measurement of the paramagnon dispersion along the (0,0)→(π,0) or (0,0)→(π,π) direction, respectively. The standard scattering geometry has been used.

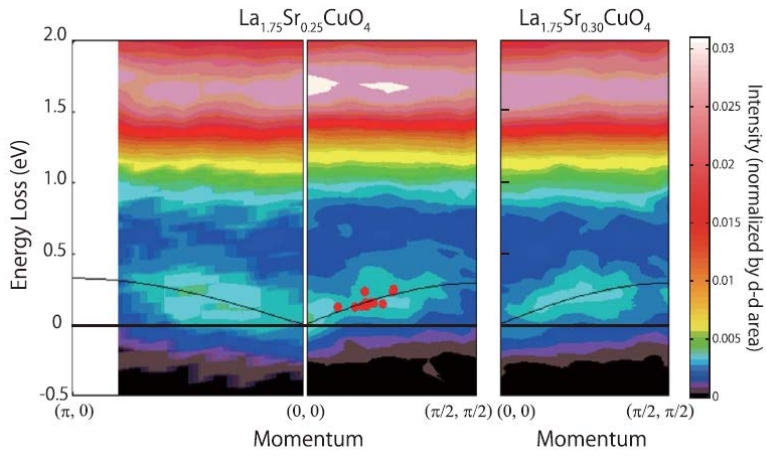

Fig. 4.13: Contour maps of RIXS intensity. The high intensity at ∼ 1.8 eV is due to the *dd*-excitations. The dispersive feature below 0.5 eV is the paramagnon. Solid lines give the spin-wave dispersion of LCO, solid circles indicate the peak positions of neutron magnetic peak. Fig. reproduced from Ref. [103].

Fig. 4.13 shows a color map of the RIXS intensity measured along the two high symmetry directions. We can clearly distinguish the *dd*-excitations around 1.6 eV and a dispersive mode assigned to a paramagnon excitation below 500 eV, for both directions. For sake of clarity, the spin-wave dispersion of LCO is plotted in solid lines above the map, together with the experimental points derived from INS along the (0,0)→(π,π) direction. The paramagnon peak positions have been also determined by a fitting of the RIXS data, in analogy with what we have done for $La_{2-x}Sr_xCuO_4$ thin films. The resulting magnetic peak positions infeed by RIXS and INS data have been summarized in Fig. 4.14, together with the data derived from thin films samples. Data from bulk crystals and thin films are in good agreement, as expected.

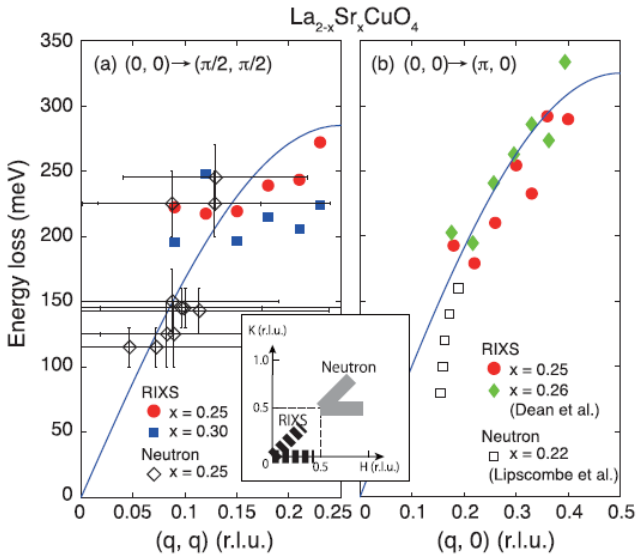

Fig. 4.14: Paramagnon dispersions along (a) the (0,0)→(π,π) and (b) the (0,0)→(π,0) directions of the reciprocal space. Solid lines give the spin-wave dispersion of LCO. The thick dashed and gray lines in the insert indicate the **q** trajectories of the dispersions measured by RIXS and neutron, respectively [103].

4.3.4 Discussion: $La_{2-x}Sr_xCuO_4$ along (0,0) → (0.5,0.5)

We have demonstrated that high-energy magnetic excitations of overdoped LSCO single crystals measured by neutron and RIXS are qualitatively consistent with each other, and that the corresponding high-energy magnetic dispersion along the (0,0)→(π,0) direction follows the spin-wave dispersion relation of the

undoped LCO in the energy range above 150 meV.

This behavior is consistent with the postulated doping independence of magnon dispersion observed by RIXS for hole-doped cuprate thin films [14,17,90].

On the contrary, from Fig. 4.14 we notice that the magnetic dispersion along the (0,0)→(π,π) direction presents a worse agreement with the spin-wave dispersion model. Such asymmetry is also consistent with numerical calculation of the Hubbard model by Jia et al. [37].

Recently, Guarise et al. [104] and Dean et al. [105] reported that the RIXS profiles of Bi-based cuprates along (0,0)→(π,π) exhibit anomalous softening or dispersionless broad excitation. This is compatible with our RIXS data, which also appear to be less dispersive than those along the (0,0)→(π,0) direction.

To better understand these phenomena, we tried to investigate the RIXS dependence on the incoming photon polarization. By comparing the spectra acquired in the configuration described in session 4.2.1 with both incident π and σ, as shown in Fig. 4.15, we conclude that an appreciable charge excitation exists in the same energy range of magnetic excitation. These charge excitations may affect the magnetic excitations, possibly in different manners between the two directions of the reciprocal space, causing the observed difference in magnetic excitations.

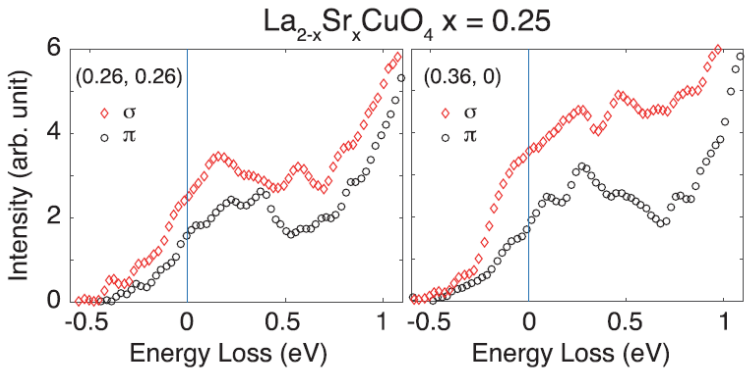

Fig. 4.15: RIXS profiles measured with π and σ configurations at 45° rotation of the sample from the specular orientation [103].

More precise RIXS measurements, with both finer energy resolution and polarization analyses are thus necessary to properly distinguish the magnetic and charge excitations. However, such a balance of the π- and σ-configuration spectra sug-

gests that spin and charge excitations are mixed because of the itinerant character, in analogy with what we have seen in session 4.2 and we will show in the next Chapter for electron-doped samples.

We now anticipate that our findings on over-hole-doped samples add new elements to the understanding of the asymmetry between electron- and hole-doping discussed in Chapter 5, where we will simply suggest that: (i) in the electron-doped system the itinerant character becomes stronger even at the optimally doped level and the magnetic excitation changes concomitantly, whereas (ii) in the hole-doped system, the itinerant character slowly grows with doping, and the high-energy magnetic excitation hardly changes.

In all the discussions presented in the next Chapter, we should thus keep in mind that observed persistence of paramagnons in the strongly itinerant over-hole-doped samples actually further complicates the problem, adding a new tassel to the puzzle of superconductivity.

4.4 Paramagnons in exotic systems

The RIXS spectra shown so far have been mainly acquired from single crystals or thin films samples. As a concluding remark for this Chapter devoted to the study of magnetic excitations in cuprates, we would like to stress that HTS superconductivity can also be achieved in more exotic copper oxides and the study of their collective excitations has recently attracted increasing interest.

Advances in thin films deposition techniques allow nowadays the synthesis of transition-metal oxides layers with atomic precision. In this way is it possible to alter the cuprates, in order to optimize their existing behavior and also engineering new states not feasible in the crystalline structure [106]. This can be done by growing heterostructures where the doping is controlled by charge transfer from the interfaces [107], or by confinement within nanostructures [28,75], strain [108], orbital reconstruction [109], and many other phenomena.

The need of investigating the collective excitations in these artificial cuprates follows directly from their increased complexity. We stress that INS is not applicable to the study of so tiny amount of material, RIXS is thus the leading technique for collective excitations investigation in HTS heterostructures.

The second part of Chapter 5 is mainly devoted to a direct comparison between

hole- and electron-doped artificial superconducting cuprates, obtained by superlattices and heterostructures, respectively. These systems are studied in a wide range of dopings and their spectral features are directly investigated, probing a perfect correspondence between collective excitations in bulk crystals and artificial samples.

In general, we can asset that (para)magnon-like collective excitations persist in a wide range of cuprates, irrespectively of the complexity of their structure [28,34,75,82,110].

Here we just show to very special cases in which the reduced dimensionality is brought to its limits: (i) single unit cell layers and (ii) nanopatterned cuprates.

4.4.1 Paramagnons in ultrathin cuprates

The data and the analyses shown in the following paragraph have been reported from *"Spin excitations in ultrathin optimally doped high-Tc cuprates"* by M. Minola, G. Dellea, M. Salluzzo, F. Baiutti, G. Cristiani, G. Logvenov, M. Le Tacon, and B. Keimer, L. Braicovich, and G. Ghiringhelli, unpublished.

Considering the first case, we know that most part of the physics of HTS copper oxides is linked to their intrinsic bidimensionality and takes place in the CuO_2 planes. However, technical limitations in sample preparation have always precluded the possibility to narrow the study of cuprates down to a few layers of material or, ideally, to a single doped CuO_2 plane.

The recent progress in layer-by-layer deposition techniques has now made available high quality ultrathin films with thicknesses down to a few unit cells.

Here we show that momentum resolved high resolution resonant inelastic x-ray scattering (RIXS) can be pushed to measure ultrathin cuprates down to one single unit cell. This means only two isolated CuO_2 planes, differently from what was done in prior works [28,75], where ultrathin films were repeated in a superlattice geometry.

In particular, we use RIXS at Cu-L_3 to probe ultrathin cuprate films of optimally doped $La_{1.85}Sr_{0.15}CuO_4$ (LSCO) and $NdBa_2Cu_3O_7$ (NBCO).

The ultrathin LSCO samples are respectively 1, 2, and 4 unit cells (u.c.) thick films grown on (100) $LaSrAlO_4$ (LSAO) substrate and protected on top with a 10 nm thick Au capping layer. The NBCO samples are 1 and 2 u.c. thick films grown on (100) $SrTiO_3$ (STO) substrate and covered by amorphous NBCO with an equivalent

thickness of 2 u.c. (roughly 25 Å). The thick films used as bulk references are respectively a 30 u.c. thick LSCO and a 80 u.c. thick NBCO, both with no capping layer. The 1 u.c. films show no superconducting transition while all other samples become SC at T_c = 20, 25, and 38 K for 2, 4 and 30 u.c. LSCO respectively, and T_c = 30 and 92 for 2 and 80 u.c. NBCO.

The RIXS measurements were performed at the ADRESS beamline of the Swiss Light Source using the SAXES spectrometer, with a combine resolution of 190 meV. The standard scattering geometry has been used, and π incident polarization has been chosen in order to increase the sensitivity to the magnetic signal.

Fig. 4.16 shows a summary of the raw spectra from LSCO and NBCO.

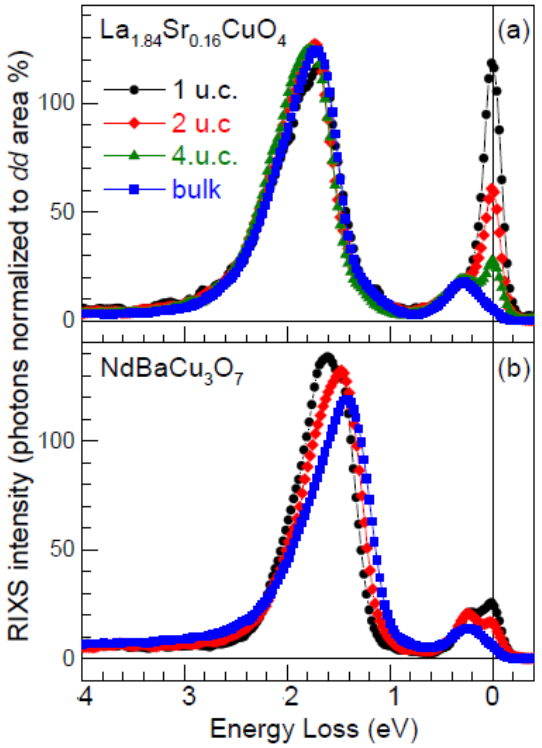

Fig. 4.16: RIXS spectra at fixed $\mathbf{q}_{\parallel}$ = 0.37 r.l.u. for LSCO (a) and NBCO (b) samples respectively. The intensity has been normalized to the area of *dd*-excitations put equal to 100.

The spectral features between 1 and 2.5 eV corresponds to *dd*-excitations, as already observed elsewhere [31] they get broader with increasing doping. The low

energy spectra is mainly dominated by the strong elastic scattering in thin films, while it clearly presents a paramagnon peak around 250 meV in bulk reference samples.

By properly fitting the RIXS spectra following the procedure previously shown in this Chapter, the paramagnon peak position a width can be determined for all samples. Results are shown in Fig. 4.17.

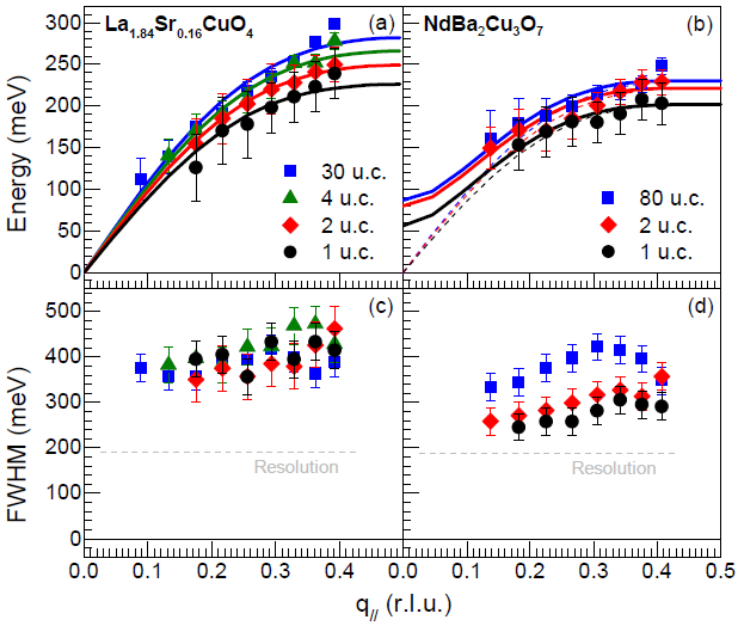

Fig. 4.17: Dispersion of magnetic excitations and linewidth of the magnetic peak for LSCO (a, c) and NBCO (b, d) samples respectively.

The analysis clearly shows the presence of a paramagnon excitation in the spectra obtained from the ultrathin samples. This is a remarkable result and suggests that short range antiferromagnetic (AF) order is still present even in a sample as thin as one unit cell.

Surprisingly, all ultrathin films show a dynamics similar to the bulk reference, but progressively reduced as the thickness of the film is decreased down to one unit cell, i.e. only two CuO_2 planes. This implies a decrease of the superexchange in the planes with respect to the bulk case. However, even if the in-plane magnetic coupling is weakened, the AF order is remarkably strong and preserved on a range long enough to allow the measurement of the paramagnon dispersion.

4.4.2 Paramagnons in nanopatterned cuprates

The effect of reduced dimensionality on collective excitations in cuprates can be further investigated by the RIXS study of nanopaterned samples [111-115].

In Fig. 4.18 we show preliminary feasibility spectra acquired with ERIXS spectrometer from: (i) a strongly underdoped YBCO thin film grown on a MgO(110) substrate, with T_c = 42.5 K (black); (ii) 50 nm thin of underdoped YBCO on MgO(110), with T_c = 53.7 K, covered on top with 50 nm of Au capping (blue); (iii) YBCO nano-wires with 65 nm width (see the insert) obtained by nanopattering of the 50 nm film (red).

Spectra have been acquired in the standard experimental geometry, with π incident polarization and 15 minutes acquisition time. For the free of them, elastic peak, *dd*-excitations and a low energy contribution compatible with paramagnons observations can be easily identified.

Despite a proper estimation of the low energy feature dispersion has still to be performed, these results suggest once more the robustness of magnetic excitation across all families of cuprates samples.

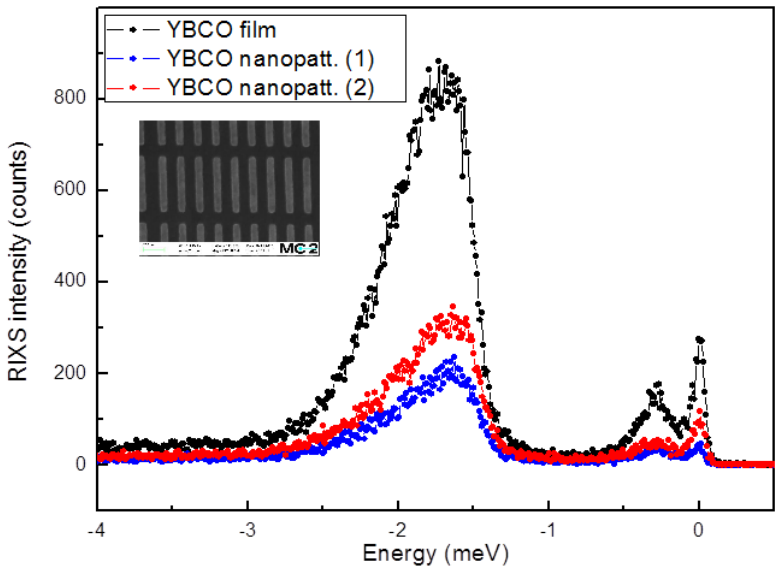

Fig. 4.18: RIXS spectra of YBCO thick film (black), YBCO thin film (blue) and YBCO nanowires (red).

Chapter 5

Collective excitations in electron-doped cuprates

We have shown that the evolution of electronic excitations upon carrier doping is an extremely important piece of information in the understanding of layered cuprates physics. Despite intensive studies on different samples, a comprehensive knowledge of the asymmetry between electron- and hole-doping and the evolution of relative magnetic and charge excitations is still fragmentary.

It is possible to achieve superconductivity by doping with both holes [116] and electrons [117], but collective excitations in the electron-doped cuprates have been less investigated so far, mainly due to technical limitations in sample growing and experimental performances [118,119], leading to the necessity of a deeper exploration of the e-doped side of the phase diagram.

It should also be noted that changing the sign of the doping carriers has strong implications for the shape of the corresponding phase diagram, and some important physical proprieties, such as pseudogap, stripe order and maximum critical temperature (T_c) dramatically change from the h-doped to the e-doped side [120]; these evidences strengthen the interest in e-doped samples.

In the following we present some recent results from e-doped cuprates. The

first part of this Chapter is devoted to the study of the archetype e-doped bulk crystal $Nd_{2-x}Ce_xCuO_4$ (NCCO), while more exotic cuprates were used to perform a direct comparison between e- and h-doping, covering the entire $T_c(p)$ phase diagram within the same HTS family. In particular, copper L_3-edge resonant inelastic x-ray scattering (RIXS) measurements were performed on artificial n- and p-type infinite layers (IL). Beyond their doping dependence, these systems are also interesting *per se*, providing a new ground for the search of increasing T_c.

Beside several analogies, RIXS results show noticeable differences in the evolution with doping type of the magnetic and charge intensity and damping. Compatible trends can be found in spectra measured on both bulk and artificial cuprates, as well as in recent theoretical calculations of the spin dynamical structure factor $S(\mathbf{q},\omega)$. This gives a deeper insight in the evolution of collective excitation along the cuprates phase diagram, underlining general features, only connected to the doping type, and envisaging the possibility to explore general properties of HTS physics on a broad range of conditions, by means of artificial compounds not constrained to the thermodynamic limitation governing chemical stability of bulk materials.

5.1 $Nd_{2-x}Ce_xCuO_4$ (NCCO): the archetype e-doped

The RIXS data and the analysis presented in this session have been published as part of *"High-energy spin and charge excitations in electron-doped copper oxide superconductors"* by K. Ishii, M. Fujita, T. Sasaki, M. Minola, G. Dellea, C. Mazzoli, K. Kummer, G. Ghiringhelli, L. Braicovich, T. Tohyama, K. Tsutsumi, K. Sato, R. Kajimoto, K. Ikeuchi, K. Yamada, M. Yoshida, M. Kurooka and J. Mizuki, Nat. Commun. 5:3714 (2014).

Since a couple of years ago, the literature regarding high-energy magnetic excitations in electron-doped cuprates was restricted to a few INS works. These papers covered only a limited number of electron concentrations [119,121] and, due to the cross-section limitation, they investigated only a small region of the reciprocal space in the vicinity of the antiferromagnetic ordering vector $\mathbf{q}_{AF}$ = (0.5, 0.5). Magnetic excitations of the e-doped samples are shown to differ from the h-doped ones and they exhibit a commensurate peak centered at $\mathbf{q}_{AF}$ at low energy [118].

Here we use for the first time Cu-L_3 edge RIXS for studying the electron-doping

dependence of high-energy spin and charge excitations in the archetype $Nd_{2-x}Ce_xCuO_4$ (NCCO) single crystal.

Our data interpretation is made simpler by the help of experiments done with complementary techniques, such as Cu-*K* edge RIXS and INS measurements on the $Pr_{1.40-x}La_{0.60}Ce_xCuO_4$ (PLCCO) e-doped cuprate. PLCCO and NCCO belong to the same family of cuprates, so that they can be meaningfully compared.

A generic phase diagram of $(Nd,Pr,La)_{2-x}Ce_xCuO_4$ is shown in Fig. 5.1(a) as a function of the Ce concentration. For the present study, a selection of representative Ce concentrations, spanning the entire phase diagram, has been chosen for NCCO investigations: x = 0 (undoped antiferromagnet), x= 0.075 (doped antiferromagnet), x = 0.15 (optimally doped superconductor) and x = 0.18 (overdoped superconductor). Sample temperature was kept at 20 K, well below the antiferromagnetic or superconducting transitions.

5.1.1 Experimental

The Cu-L_3 edge RIXS experiments were performed at the ID08 beamline of the ESRF using the AXES spectrometer. The total energy resolution was estimated around 250 meV, which is not strictly limiting for the present study due to the intrinsic broadening of the magnetic spectral features under investigation.

We used the standard experimental geometry, which is schematically reported in Fig. 5.1(b). The configuration with $\mathbf{q}_{\parallel} > 0$ and π incident polarization was chosen to maximize the spectral weight of the spin excitations compared with other excitation channels, such as charge and lattice [32].

In Fig. 5.1(c) we show the doping dependence of the RIXS spectra in the low energy scale and at fixed momentum transfer $\mathbf{q}_{\parallel}$ = (0.18,0). Following the spectra decomposition used in Ref. [82] and in Chapter 4, the spectrum for the undoped compound (x = 0) can be univocally separate into the elastic (purple), single-magnon (red) and multi-magnon (cyan) components. We clearly notice that the single-magnon component is dominant, and its spectral weight moves to higher energy upon electron doping, while its width broadens.

In general, a resolution-limited Gaussian function is used to fit the elastic peak, while the inelastic excitations (i.e. magnetic and charge) are modeled by an anti-symmetrized Lorentzian function multiplied by the Bose factor and convoluted by the Gaussian resolution function. The Lorentzian width is infinitesimal for the spectra of the undoped compound (x = 0), whereas it is kept variable when the effect

of doping has to be taken into account. In doped samples, an extra peak close to the Γ point has also been found, as shown for x = 0.15 in Fig. 5.1(d). It is probably related to a charge excitation, as discussed later. A tail (in gray) coming from the *dd*-excitations located at higher energies (∼ 2 eV) has also been introduced in the analysis.

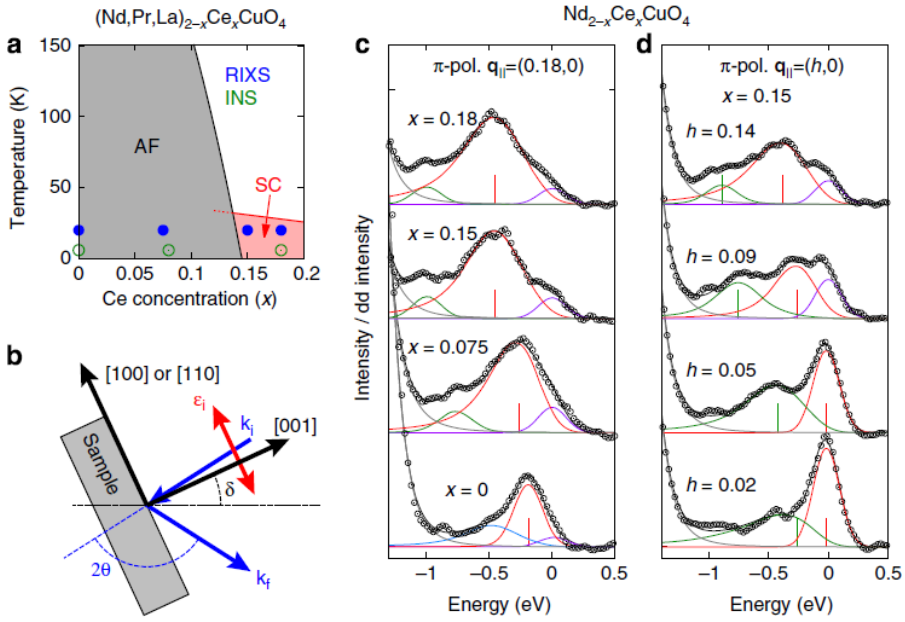

Fig. 5.1: (a) Generic phase diagram of the electron-doped copper oxide superconductor $(Nd,Pr,La)_{2-x}Ce_xCuO_4$. Antiferromagnetic (AF) and superconducting (SC) phases are shown. Filled circles indicate the measured points for Cu-L_3 RIXS; INS complementary measurements were taken in correspondence of the open circles. (b) Cu-L_3 RIXS experimental configuration. (c,d) $Nd_{2-x}Ce_xCuO_4$ Cu-L_3 RIXS spectra with π incident polarization; (c) doping dependence at fixed in-plane momentum $\mathbf{q}_\parallel$ = (0.18,0) and (d) momentum dependence at fixed doping x = 0.15. The experimental spectra (open circles) are restricted to the low energy scale, and they are decomposed into a few components (solid lines). The peak positions of the spin-flip magnetic component (red) and the charge excitations (green) are indicated by vertical bars. Fig. reproduced from Ref. [122].

A systematic of the doping and momentum dependence of Cu-L_3 RIXS spectra of NCCO have been exploited and it is summarized in Fig. 5.2.

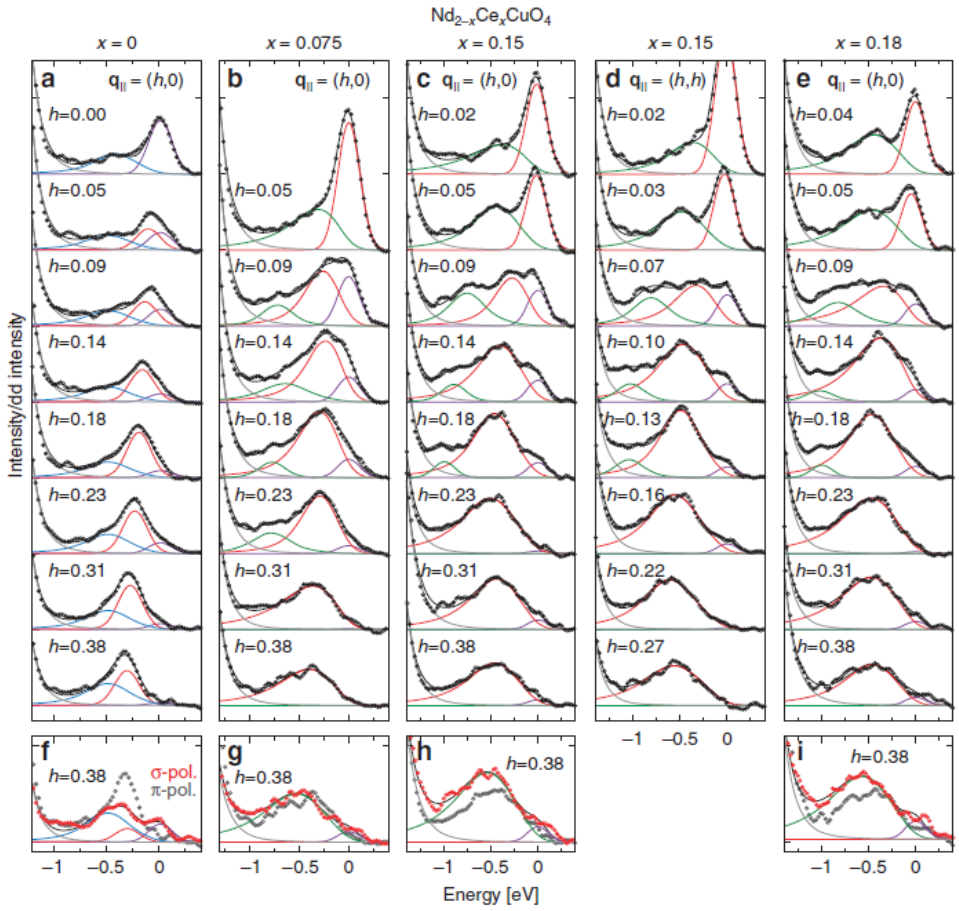

Fig. 5.2: $Nd_{2-x}Ce_xCuO_4$ Cu-L_3 RIXS spectra. (a–e) Momentum dependence; spectra are acquired with π incident polarization. Open circles denote the experimental data and solid lines gives the fitting results for elastic (purple), spin-flip excitations (red), multi-magnon (cyan), *dd*-excitations tail (grey) and the sum of the all components (black). For doped compounds (b-e), the decomposition of the elastic and the magnetic components is not trivial at very low $\mathbf{q}_\parallel$, therefore we do not separate them, and a single magnetic component (red) is used, together with an additional charge peak (green). We rely on INS for the determination of the magnetic peak positions near the Γ point. (f–i) Comparison between the spectra observed with incident σ and π polarization at fixed momentum transfer $\mathbf{q}_\parallel$ = (0.38,0) [122].

The results for x = 0, shown in Fig. 5.2(a), are similar to those obtained in previous studies on undoped cuprates [17,76,82]. The single-magnon components are found to be resolution-limited and their momentum dependence follows the dis-

persion of a spin-wave in an antiferromagnetic square lattice.

The analysis of the doped compounds spectra, shown in Fig. 5.2(b–e), is less straightforward, due to the intrinsic peaks broadening. For large values of the in plane momentum transfer $\mathbf{q}_{\parallel}$, a single inelastic component is used, whose spectral weight is mainly assigned to the spin-flip excitations [14,17,77,90], similar to what is done in Chapter 4 for hole-doped cuprates. This assignment is supported by recent theoretical studies, which probed that RIXS spectral shape agrees well with the dynamical spin correlation function $S(\mathbf{q},\omega)$, when incident π polarization is used [37,38]. In addition, Raman scattering observed a weakening of the two-magnon component by electron doping [123], and it is therefore acceptable to neglect it in our analysis.

In Fig. 5.3(a,b) the peak position and width obtained from the above fittings are plotted against the momentum transfer. These results clearly show that the magnetic excitations broaden and shift to higher energy upon electron doping, consistently with recent theoretical calculation [37].

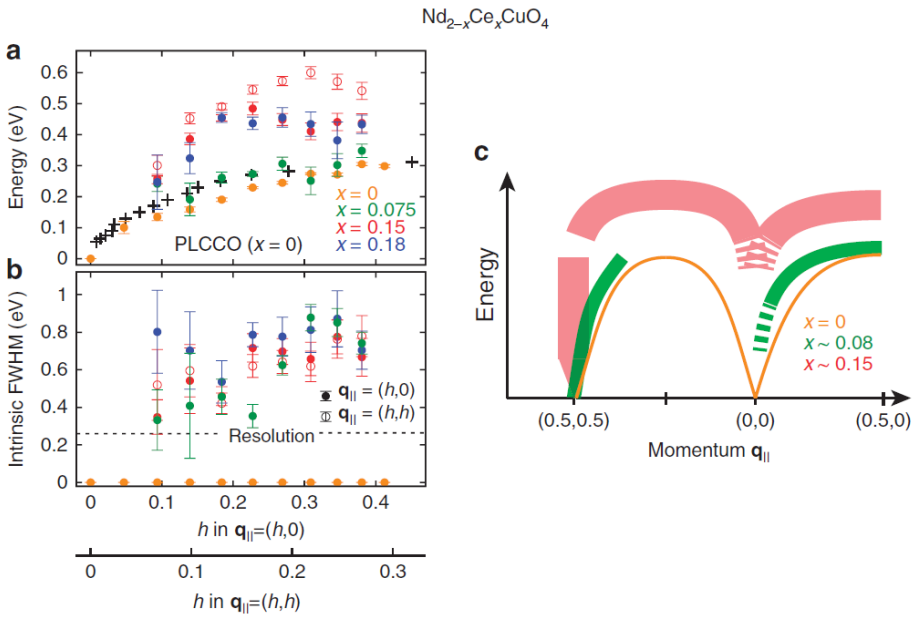

Fig. 5.3: (a,b) Peak position and width (FWHM) of NCCO magnetic excitations as probed by RIXS. INS estimated peak positions of undoped PLCCO are also shown (black crosses). The peak width of undoped NCCO is fixed to infinitesimal in the analysis. Vertical bars represent the uncertainty in fitting procedure. (c) Schematic representation of the magnetic excitations in energy-momentum space [122].

Combining our data with complementary INS measurements on the equivalent PLCCO electron-doped cuprate, we can have a deeper understanding of the evolution of magnetic excitation across the momentum space. While Cu-L_3 RIXS is able to investigate a large portion of the first BZ around the Γ point, INS can indeed cover the region near $\mathbf{q}_{AF}$. Briefly, the magnetic spectral weight in neutron measurements is probed to move toward higher energy upon doping at a certain momentum away from $\mathbf{q}_{AF}$, consistently with our RIXS results around the Γ point. This outcome is qualitatively summarized in Fig. 5.3(c).

We now turn to the study of the extra peak (green in fittings) observed in the doped samples with Cu-L_3 edge RIXS. It is a fast dispersing peak, whose intensity rapidly decreases while moving away from the Γ point. We note that the evaluation of its cut-off momenta is made difficult by the overlapping with the huge tail of *dd*-excitations.

To understand its nature, we plot the corresponding peak positions for NCCO (x = 0.075, 0.15 and 0.18) obtained by the fitting analysis on a Cu-*K* edge RIXS intensity map re-plotted from Ref. [124].

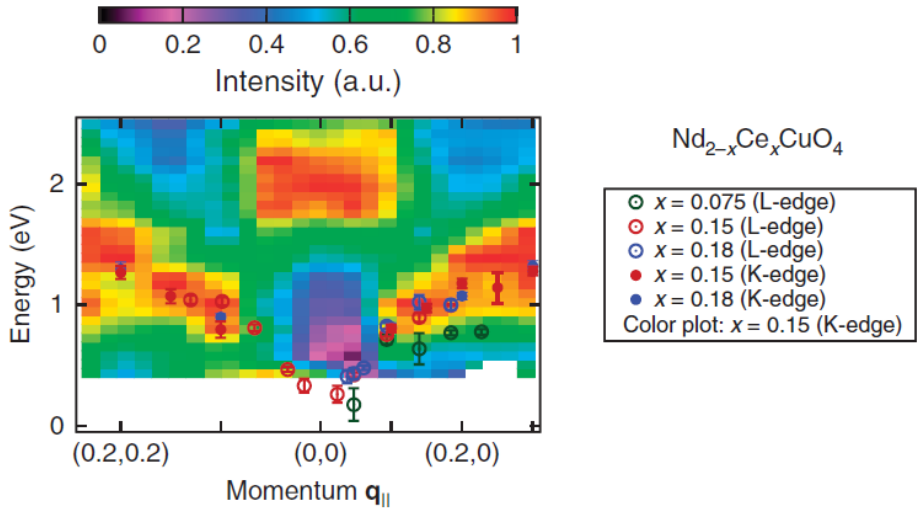

Fig. 5.4: Open circles give the peak position of the additional spectral feature observed with Cu-L_3 RIXS in doped cuprates. The intensity map of *K* edge RIXS measurements is re-plotted from Ref. [61]. Filled circles give the peak position of *K* edge RIXS for NCCO with x =0.15, 0.18. Vertical bars represent the uncertainty in the fitting analysis [122].

From Fig. 5.4 we can conclude that the peak positions from Cu-L_3 edge RIXS smoothly connect to the dispersive features in the Cu-*K* edge RIXS. Therefore, it seems reasonable to ascribe the two excitations to the same origin, i.e. possibly particle-hole excitations within the upper Hubbard band. We stress that spin-flip transitions are forbidden in *K* edge RIXS, so that the extra peak intensity seen in our spectra can be assigned only to charge excitations [124,125].

5.1.2 Discussion

For the first time we were able to perform Cu-L_3 RIXS on electron-doped cuprates. Our data, complemented by INS and Cu-*K* edge RIXS, have provided important information on the doping evolution of spin and charge excitations in these systems. The spin-wave magnetic excitations typical of the undoped insulator shift to higher energy upon electron doping over a wide region of the momentum space. This is in stark contrast with the hole-doped case, where the spectral features related to magnetic excitations broaden with doping, but their energy position remain almost unchanged, closely following the spin-waves dispersion of the parent compound [14,17,77,90].

We can thus conclude that, while in hole-doped cuprates the observed high energy spin excitations are likely a remnant mode of the antiferromagnetic parent compound and the spin dynamics retain a localized nature, the RIXS spectra for electron-doped copper oxides seems to reflect a strongly itinerant character [121].

This itinerant character can be also observed by exploiting the polarization dependence of Cu-L_3 RIXS, as done in Fig. 5.2(f,i). We know that for large positive values of $\mathbf{q}_{\parallel}$, spin-flip excitation dominate the low energy scale of the RIXS spectra when π incident polarization is used, whereas they are negligible in incoming σ polarization condition [31,32]. If we systematically compare RIXS spectra acquired in these two conditions, we notice that for the undoped NCCO the single magnon is clearly enhanced by π polarization, as expected from our previous observations in other antiferromagnetic parent compounds [17,33], while multi-magnons dominate the spectrum with incident σ polarization. When the electron doping is further increased, the spectral shape becomes similar between the two polarizations. In optimal and over- electron-doped compounds, magnetic (spin-flip) and charge (not-spin-flip) excitations are thus mixed in the same energy scale.

A new charge related spin excitation has been also observed, despite its origin is still unclear. More recent RIXS results on NCCO electro-doped samples, beyond confirming our experimental finding for the magnetic excitations, have showed a

temperature dependence of this fast dispersing feature [126]. The results coming from this investigation, together with the observation of a charge density wave related signal in NCCO [127], suggest that these collective charge modes might be associated to a symmetry-broken state.

5.2 Infinite layer samples: a direct comparison

Our understanding of collective excitation in electron-doped cuprates is mainly based on two pioneering experiments on the archetype crystal NCCO [122,126]. This boosts the interest in the exploration of the doping dependence of magnetic and charge excitations in new families of cuprates and more exotic samples.

In this contest, infinite layer (IL) AFM parent compounds represent the best starting point for our systematic research, because of their crystallographic structure, which is the simplest among layered cuprates.

As we have seen in Chapter 1, the doping charge needed for the superconducting transition is provided, in bulk crystals and thin films, by a change in stoichiometry. A different approach takes advantage of recent progresses in epitaxial growth, and it is based on a proper engineering of heterostructures (HSs) [128,129] and superlattices (SLs) [130,131]. These synthetic HTS, not constrained by thermodynamic limitations connected with bulk crystal growth, are particularly interesting in the search of increasing T_c.

In this Chapter two families of artificially engineered Cu-based superconductors have been used: $(CaCuO_2)_n/(SrTiO_3)_m$ (CCO/STO) SLs were necessary to obtain h-doped IL superconductors [75,132], while $Sr_{1-x}La_xCuO_2/GdScO_3$ (OLSCOG) HSs allow to achieve superconducting ILs doped with electrons [133,134].

In Fig. 5.5 a schematic layout of these two samples families is presented. Fig. 5.5(a) shows the SLs structure: $(CaCuO2)_n/(SrTiO3)_m$ superlattices are made by n u.c. of $CaCuO_2$ alternated with m u.c. of $SrTiO_3$ for N = 10 ÷20 repetitions, on a $NdGaO_3$ (110) substrate; when these SLs are grown in highly oxidizing atmosphere, the interfaces act as a charge reservoir leading to superconductivity. X-ray diffraction (XRD) characterization indicates the formation of a high quality superlattice [132]. For superconducting SLs, CCO_n/STO_m heterostructures were respectively: n=13, m=2, T_c = 12 K (thick CCO layer); n=7, m=2, T_c = 16 K (intermediate CCO layer); n=3, m=2, T_c = 25 K (thin CCO layer). Undoped SL (n=3, m=2.5) is not superconducting, being not grown in ozone atmosphere.

Fig. 5.5(b) schematizes the HSs structure: starting from undoped $SrCuO_3$, superconductivity is achieved by controlling the La substitution stoichiometry, the substrate lattice constant and the oxygen level in the growing atmosphere. In particular, electron doped $Sr_{1-x}La_xCuO_2$ thin films have been grown on $GdSO_3$ substrates, and superconductivity is achieved by *in situ* vacuum annealing step, which results in an oxygen loss from the films. The superconducting transition temperature depends on the La content (x = 0.08, 0.10 and 0.13) and corresponds to: T_c = 27.8, 28 and 19.5 K [133].

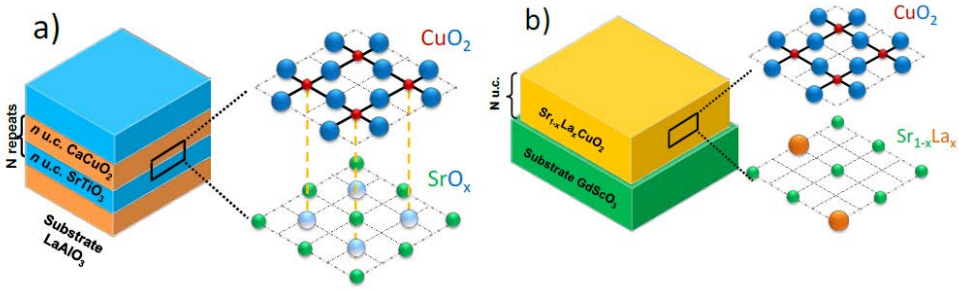

Fig. 5.5: Schematic cartoon of the artificial e- and h-doped cuprates under investigation. (a) Typical h-doped $(CaCuO_2)_n/(SrTiO_3)_m$. When a SrO_x-CuO_2 interface is formed, copper oxides planes can partially gain apical oxygens losing their IL structure. Doping charge transfer is also possible between CuO_2 and CaO_y oxidized planes (here not shown). If SLs are growth in high oxygen pressure, the oxygen content at the interfaces will be x+y > 1, and this will lead to superconductivity. For more details see Ref. [132]. (b) Typical e-doped $Sr_{1-x}La_xCuO_2$ HEs. Alternating CuO_2 and $Sr_{1-x}La_x$ planes gives rise to the IL structure. Tensile strain from the substrate, partial substitutions of large rare-earth La^{3+} ions and in situ vacuum annealing are crucial in achieving superconductivity. For a detailed description of sample preparation and characterization see Ref. [133].

5.2.1 Experimental

Cu-L_3 RIXS experiments were performed with AXES spectrometer at the ID08 beamline of the European Synchrotron Radiation Facility (ESRF). RIXS represents the only available tool to investigate magnetic excitations in such small samples: the scattering cross section is indeed 11 orders of magnitude larger compared to inelastic neutron scattering (INS), and allows to dramatically reducing the required sample volumes [91].

The estimated combined energy resolution of the beamline monochromator and the spectrometer is 250-265 meV for $(CaCuO2)_n/(SrTiO3)_m$ SLs and $Sr_{1-x}La_xCuO_2$ HSs measurements respectively. Samples temperature was kept at 20 K.

As already done in the NCCO experiment, we use the experimental configuration (π incident photon polarization, and $\mathbf{q}_\parallel > 0$) well known for enhancing the spin flip contribution [31].

Fig. 5.6 presents a general overview of the momentum and doping dependence for the two sample families. In Fig. 5.6(b) the two AFM parent compounds are directly compared; a distinct feature emerges from the elastic peak at zone center (Γ point) for both AFM samples, it disperses toward higher energies with increasing momentum and reaches its maximum ($\sim$ 300 meV) along the high symmetry direction of the AFM ZB. Notably, this spectra feature is almost perfectly superimposed for both $SrCuO_2$ (blue line) and $(CaCuO_2)_3/(SrTiO_3)_{2.5}$ (red line), confirming the assumption of considering two sample families with equivalent behavior in the AFM state.

In analogy with previous analyses on insulating bulk cuprates [77] and SLs [75], spectra can be simply decomposed in two resolution limited contributions: (i) an elastic peak and (ii) an inelastic peak; remaining spectral weight at higher energies was associated to multiple magnons, and a phonon contribution at $\sim$ 80 meV was considered for SLs [75]. Experimental geometry allows straightforward identification of the inelastic-resolution-limited peak with a single magnon excitation [31]. The peak position and energy dispersion can be determined by fitting. The results are shown in Fig. 5.7(b); data present the typical evolution of spin waves in an AF square lattice, consistent with what already found in previous RIXS experiments on undoped bulk cuprates [32-34,76] and SLs [28,75].

Fig. 5.7(a-c) shows the corresponding spectra for hole- and electron-doped samples: $Sr_{0.9}La_{0.1}CuO_2$ and $(CaCuO_2)_3/(SrTiO_3)_2$ respectively. Raw data clearly display dramatic differences in the low energy scale under different dopings. Dispersing peak in h-doped sample closely mimic the magnon peak observed in AFM parent compounds. While e-doped features present a steeper dispersion: faster at lower $\mathbf{q}_\parallel$ ($\leq$ 0.18 r.l.u.) and almost flat for higher values of the momentum transfer; a significant hardening in energy ($\sim$ 20% at AFM ZB) compared to undoped and h-doped case is also revealed.

A fitting procedure was used to determine the dispersing features peaks for doped samples. As already discussed, the inelastic contribution is broad, and the spectra cannot be easily decomposed in two resolution limited components. This is

better exemplified in Fig. 5.7(a), showing a comparison between RIXS spectra of insulating $SrCuO_2$, and best superconducting h- and e-doped samples.

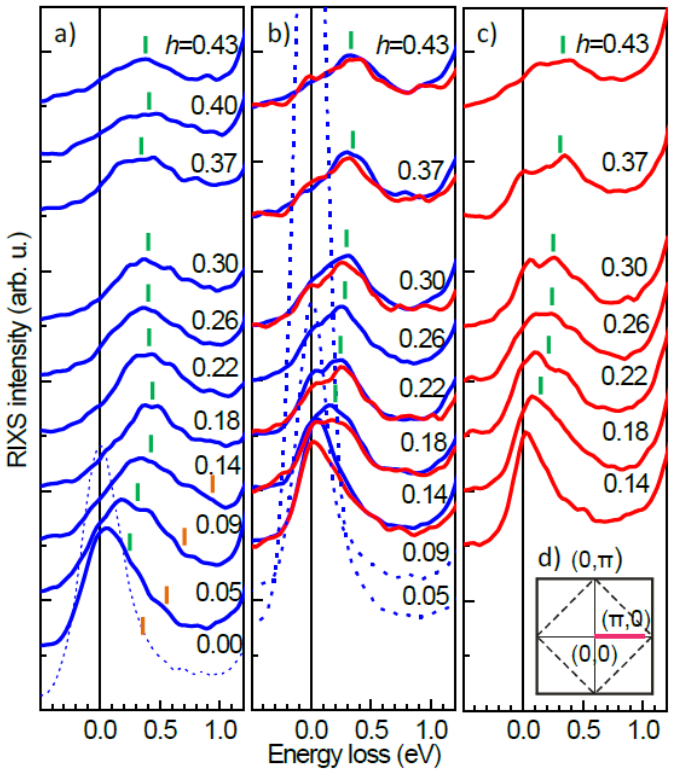

Fig. 5.6: (a-c) Cu-L_3 edge RIXS raw spectra waterfall plots of the momentum dependence as a function of doping type, with π incident polarization, along the (0,0) → (π,0) direction. The in-plane transferred momentum is defined as $\mathbf{q}_{\parallel} = (h,0)$ and expressed in reciprocal lattice units. $Sr_{1-x}La_xCuO_2$ are denoted with blue lines, while SLs $(CaCuO_2)_n/(SrTiO_3)_m$ with red lines. Green ticks indicate the (para)magnong position as estimated by fitting procedure. Orange thick lines give the fast dispersing charge peak. (a) Optimally electron-doped sample: $Sr_{1-x}La_xCuO_2$ with x = 0.1. (b) Insulating AFM parent compounds: $SrCuO_2$ (blue solid lines) and not superconducting $(CaCuO_2)_3/(SrTiO_3)_{2.5}$ (red solid lines). (c) Best superconducting hole-doped sample: $(CaCuO_2)_3/(SrTiO_3)_2$. (d) Schematic picture of the first Brillouin Zone. Pink solid line highlights the spanned region of the reciprocal space.

The instrumental resolution used to fit the AFM data is not large enough to properly fit the doped spectra. Moreover, e-doping induces a stronger broadening compared to h-doping. This broadening is an intrinsic phenomenon, suggesting

that we are dealing with dynamical magnetic fluctuations [17]. Hole-doped spectra in Fig. 5.6(c) were fitted associating the inelastic spectral weight to a single non-resolution-limited magnetic component, following the procedure used in Chapter 4. A paramagnon-like dispersion is clearly noticeable, similar to what is found in bulk h-doped samples [14,17,77,90]: the magnetic peak gets damped and broadened, but retains the same trend with increasing $\mathbf{q}_{\parallel}$ of the AFM parent compound. The energy peak position slightly shifts to lower energies as a consequence of a reduced dynamics.

Our RIXS results clearly demonstrate that magnetic excitations associated to doped SLs, where superconductivity was obtained by artificially induced doping at the interfaces, preserve the behavior observed in bulk crystals.

The peak decomposition is less straightforward for superconducting e-doped sample in Fig. 5.6(c). The inelastic feature gets broader for lower $\mathbf{q}_{\parallel}$ (≤ 0.18 r.l.u.); alternatively we can think that the charge continuum coming from doping carriers undergoes an evolution close to the Γ point.

As clarified in Fig. 5.7(a) and in Ref. [17], while doping the sample, spectral weight around 0.8-1.5 eV increases due to the filling of continuum states associated to doping carriers. At equivalent doping levels, the charge contribution given by e-doping is stronger compared to h-doping. Moreover, while the charge-step associated to h-doping is constant in $\mathbf{q}_{\parallel}$, the corresponding e-doping charge signal presents $\mathbf{q}_{\parallel}$ dependence, predominantly close to the Γ point.

To take into account this experimental evidence, according to what is done in the previous Session, at lower $\mathbf{q}_{\parallel}$ (≤ 0.18 r.l.u.) the inelastic spectral weight was decomposed in two non-resolution limited components: a magnetic and a charge peak, while for higher $\mathbf{q}_{\parallel}$ (> 0.18 r.l.u.), where the magnetic peak is located at higher energies and become impossible to distinguish between two different components, if any, a unique inelastic-not-resolution-limited component was fitted.

The results obtained are in good agreement with recent RIXS measurements on the prototypical e-doped cuprates NCCO as shown in the previous session and in Ref. [126], suggesting that the observed strong asymmetry between h- and e-doped samples in the magnetic spectrum, which gets steeper and harder under e-doping, and the new fast dispersing charge mode, are general features connected to the electron doping and not related to the particular sample under investigation. Fig. 5.7(b) summarizes the experimental dispersions in comparison with theoretical calculation of the dynamic spin structure factor $S(\mathbf{q},\omega)$, proved to be in good agreement with RIXS spectra, even without outgoing polarization analysis [37].

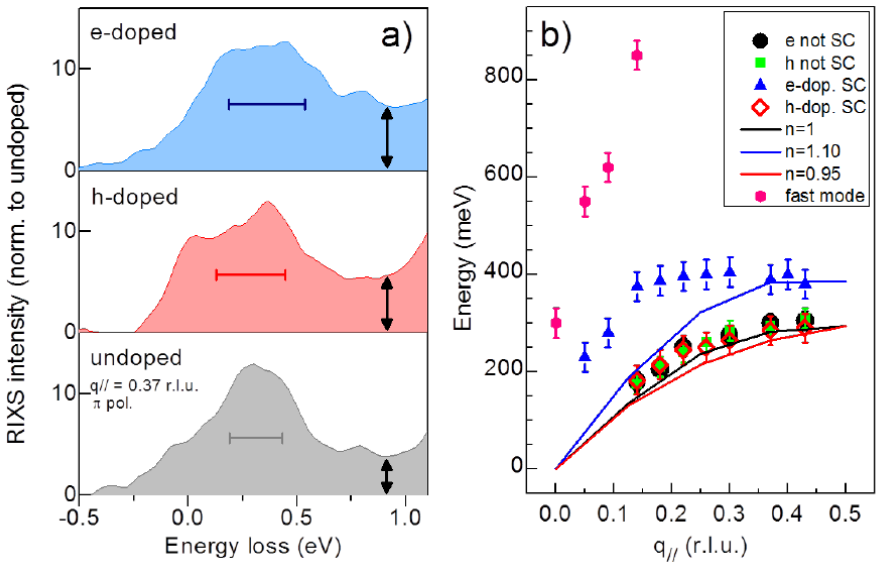

Fig. 5.7: (a) Cu-L_3 edge RIXS raw spectra of not superconducting $SrCuO_2$ (gray), best superconducting $(CaCuO_2)_3/(SrTiO_3)_2$ (red) and optimally doped $Sr_{0.9}La_{0.1}CuO_2$ (blue), at fixed $\mathbf{q}_\parallel$ = 0.37 r.l.u., with π incident polarization. Intensities are normalized to have the same height on the (para)magnon peak. Horizontal solid lines represent the FWHM of the (non-)resolution limited Gaussian used to decompose the data. Vertical arrows indicate the high energy tail mainly ascribable to the contribution of extra doping charges. Plotting undoped SL instead of $SrCuO_2$ would lead to the same conclusions. (b) (Para)magnon dispersion and fast dispersing charge mode from RIXS spectra fittings (scatteres), compared to $S(\mathbf{q},\omega)$ theoretical calculations in a single band Hubbard model (solid lines) with nearest hopping parameter t = 500 meV, and doping level denoted by the electron concentration n. Experimental error bars are given by a sensitivity analysis of the fittings.

Theoretical data are in good agreement both with undoped and h-doped experimental points, while the agreement is weaker for e-doping. The loss of agreement is particularly important for lower $\mathbf{q}_\parallel$, while theoretical curves recover the experimental points close to the AFM ZB. This can be explained again in terms of a strong itinerant character of the electron doped copper oxides [122,124]. According to RIXS cross section [29,125] for incident π polarization, at large positive $\mathbf{q}_\parallel$ values the resulting spectra is mostly dominated by magnetic excitations, while at lower $\mathbf{q}_\parallel$ spin-flip excitation are mixing in the same energy range with charge excitations, that are not taken into account by $S(\mathbf{q},\omega)$ calculations.

In Fig. 5.8, spectra at fixed $\mathbf{q}_{\parallel}$ (= 0.37 r.l.u.) and different dopings are compared with calculated $S(\mathbf{q},\omega)$. The chosen momentum transfer is close enough to the AFM ZB to provide a good agreement between experimental data and theoretical predictions.

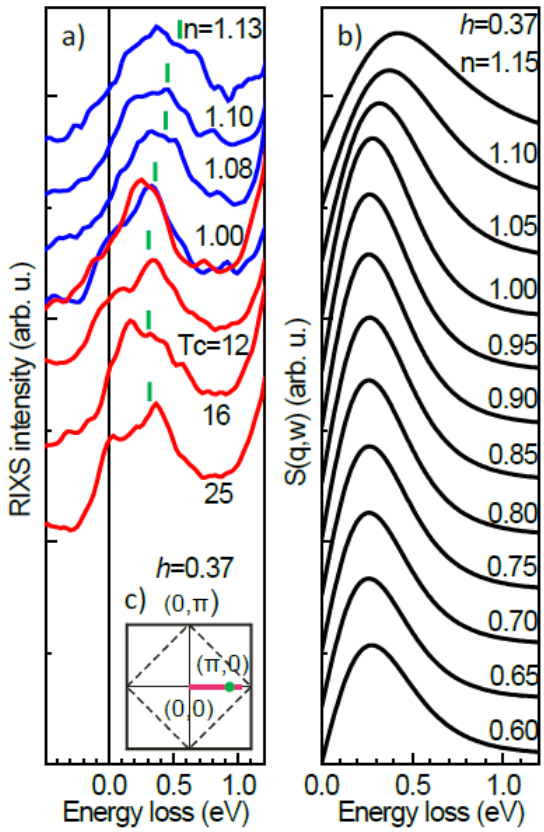

Fig. 5.8: Doping dependence at fixed transferred momentum $\mathbf{q}_{\parallel}$ = (0.37 r.l.u.,0); comparison between raw RIXS spectra and dynamic spin structure factor $S(\mathbf{q},\omega)$ in single band Hubbard model. (a) Raw RIXS spectra are measured with π incident polarization. In $Sr_{1-x}La_xCuO_2$ spectra (blue lines) the doping level is defined according to the x values, while for $(CaCuO2)_n/(SrTiO3)_m$ SLs (red lines) doping is directly linked to T_c. Green ticks indicate the (para)magnon position as estimated by fitting procedure. (b) Dynamic quantum Monte Carlo (DQMC) simulations of the dynamic spin structure factor $S(\mathbf{q},\omega)$ at (3/4π, 0) in the single band Hubbard model. Doping is denoted by the electron concentration n. (c) Schematic picture of the first BZ. Pink solid line highlights the available region of the reciprocal space, while green dot indicates the $\mathbf{q}_{\parallel}$ value used in panel (a-b).

$Sr_{1-x}La_xCuO_2$ e-doping is estimated according to La dopants stoichiometry (x), where x = 0.1 represents the optimal doping [133], while in $(CaCuO_2)_n/(SrTiO_3)_m$ the h-doping is related to the $CaCuO_2$ layer thickness (*n*): since the charge transfer is appearing at the interfaces and propagating through a few u.c., the thicker the $CaCuO_2$ layer, the lower the doping. At some point, the inner CuO_2 planes are not doped anymore and the $CaCuO_2$ layer start behaving like a mixture of bulk $CaCuO_2$ and doped SLs. In that sense, it was not possible to estimate the effective doping amount, but just a qualitative trend associated to T_c [132].

Again a good qualitatively agreement between theory and experiments can be found: h-doped samples present a magnetic peak almost independent on doping, while in e-doped samples the magnetic peak strongly evolves with increasing doping shifting to higher energies.

5.2.2 Discussion

In the present work we have proved that artificial hole- and electron-doped superconducting cuprates perfectly mimic the magnetic and charge behavior of the corresponding bulk crystals.

In particular, according to what already observed in the archetype NCCO [122,126], magnetic excitations harden significantly under e-doping, in stark contrast with hole-doping. This result is counterintuitive: the AFM correlations are presumably short-ranged due to both doping types. To reconcile this apparent discrepancy, the e-doping hardening has been interpreted in terms of strongly itinerant character compared to the more localized spin dynamics found in h-doped cuprates [122]. This unexpected asymmetry between doping types is also intrinsic of the single-band Hubbard model, as proved by $S(\mathbf{q},\omega)$ theoretical calculations [37].

Our data also confirm the unexpected and highly dispersive charge mode present in NCCO, but absent in h-doped samples. Our assignment to charge excitations is supported by RIXS Cu-L_3 edge polarization analysis and RIXS Cu-*K* edge measurements on e-doped crystals [122-124]. The origin of this mode, emanating from zone center and rapidly decaying in intensity, is still uncertain. It has been argued to be signature of a quantum phase distinct from superconductivity [126], a particle-hole excitation [122], or a plasmon excitation [124], and could be a general feature of e-doped cuprates.

In conclusion, our results open the way to the possibility of studying magnetic and charge excitations of cuprate superconductors by using a new generation of HTSC artificial materials, not constrained by thermodynamical limitation, in which

physical properties (i.e. doping level, oxygen content, T_c) can be controlled by properly tuning the growing conditions. This would allow new and unexpected possibilities to experimentally investigate superconducting cuprates.

The strong asymmetry in collective excitations between the two sides of the cuprate phase diagram, probed to be a general property of both e- and h-doped samples, opens new possibilities for future theoretical models too.

It should be stressed that, due to limitation in sample dimensions for SLs and HSs, soft-RIXS is the only possible technique for investigating charge and magnetic excitations in new artificial superconducting cuprates.

Moreover, a better understating of the observed features, especially in the case of the unexpected fast dispersing mode, will for sure benefit of the new high-resolutions-polarization-analysis installed in the new ERIXS machines [51].

5.2.3 A digression: crystal field excitations in ILs

The artificial cuprate samples used in the last session are defined as infinite layers when they are undoped. We show now that Cu-L_3 RIXS also provides a way to experimentally investigate the presence of apical oxygen for the CuO palettes and their evolution with doping. This is done by the study of crystal field (so called *dd*) excitations, which have been introduced in Chapter 2.

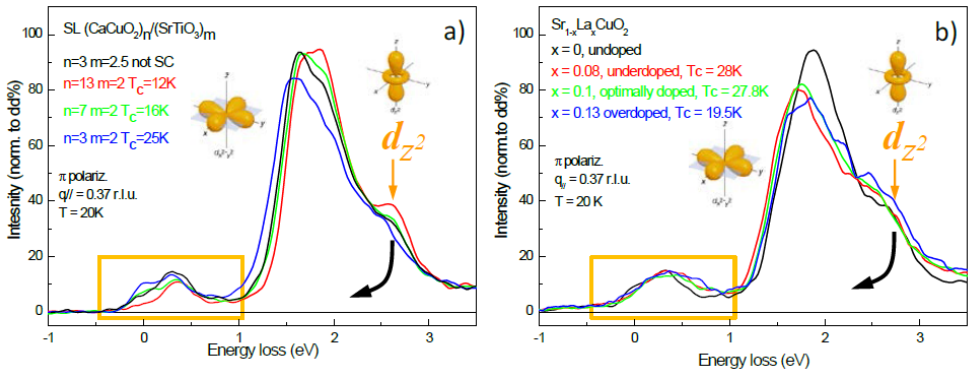

Fig. 5.9: RIXS raw spectra at Cu-L_3 edge with π incident polarization and fixed momentum transfer $\mathbf{q}_{\parallel}$ = (0.37 r.l.u.,0) for (a) $(CaCuO_2)_n/(SrTiO_3)_m$ SLs and (b) $Sr_{1-x}La_xCuO_2$ HEs. Yellow squares highlights the low energy spectral region investigated in the last session associated to magnetic and charge excitations. The peaks at higher energy loss (from 1 to 3.5 eV) correspond to *dd*-excitations. Spectra are normalized to *dd*-excitations area, set equal to 100.

The *dd-excitations* are directly related to the ligand field at Cu sites, and correspond to the transitions between the ligand-field-split *d* states of Cu ions. Their study allows thus a deeper understanding of the environment seen by Cu ions.

Fig. 5.9 shows RIXS raw spectra at Cu-L_3 for $(CaCuO_2)_n/(SrTiO_3)_m$ SLs and $Sr_{1-x}La_xCuO_2$ HEs respectively, at fixed momentum transfer. The energy window has been expanded compared to the one considered so far (yellow boxes in Fig. 5.9), in order to show higher energies excitations, such as the *dd*s (∼ 2eV).

For superconducting SLs, *dd*-excitations behavior is similar to what was observed in Ref. [75] for non-doped SLs. The d_{z2} peak, which is the one directly related to apical oxygen, undergoes a lowering and softening while increasing the number of interfaces, due to the presence of ligand apicals. The lower the number of $CaCuO_2$ u.c. (*n*), the stronger the effect.

A lowering and a softening of the d_{z2} peak is also present in superconducting $Sr_{1-x}La_xCuO_2$. The effect is stronger comparing the undoped sample to the superconducting ones, while no particular evolution is noticeable between different doping. In this case the reduction of IL character in the samples can be mostly due to defects and lattice distortions introduced by the doping process.

Chapter 6

A three-actor scenario for superconductivity

Through the previous Chapters we have demonstrated that resonant inelastic x-ray scattering (RIXS) is the perfect tool for probing low energy excitations in strongly correlated electrons systems, such as cuprates. By properly tuning the experimental parameters, RIXS can indeed reveal a variety of spectral features linked to charge, magnetic, orbital and lattice excitations simultaneously.

So far, we have mainly focused on the investigation of high energy magnetic excitations, i.e. magnons in undoped cuprates and paramagnons in HTS doped samples. We have shown the persistence of these magnetic excitations at all doping levels and both for hole- and electron-doped compounds, across the respective superconducting domes [14,17,90,122,126]. These excitations are thus exceptionally robust and retain their character also in artificial and exotic copper oxides, surviving upon changes in the samples dimensionality down to nanopatterned and single unit cell layers of material.

These observations might imply that high energy magnetic fluctuations are necessary for superconductivity, although their possible role as pairing mechanism has not been clearly demonstrated yet.

To comprehend superconductivity in cuprates we have to consider the diversity of electronic and magnetic excitations on the whole. Whether and how these excitations, such as charge, spin, lattice and orbital orders, interact with each other is still the matter of active research.

A way to investigate these interactions is provided by the ability of RIXS to measure different kinds of excitations simultaneously.

In the following we briefly review the main excitations investigated with RIXS in recent years showing a selection of our most meaningful results. A detailed description of each excitation goes beyond the interest of this introductive Chapter and for more details we refer to the related literature.

6.1 Density-wave ordering

Recent experiments on underoped samples have uncovered the evidence of charge-ordering phenomena in the CuO_2 cuprates planes [135].

The first experimental evidence of such a charge order was obtained in the so-called *214* cuprates family [136-141]. These cuprates have the typical structure of $La2_{-x}Ba_xCuO_4$ and $La_{1.8-x}(Nd,Eu)_{0.2}Sr_xCuO_4$ and their charge ordering was probed to be directly linked to doping-induced incommensurate spin correlations, known as *stripes*. In particular, for a doping charge concentration of $p \sim 1/8$, the uniaxial stripe domains show approximately a commensurate periodicity, corresponding to $\sim 4a$ for charge, and $\sim 8a$ for spin degrees of freedom, where a defines the lattice constant, i.e. the spin periodicity is two times the charge one, as expected for such a ordering.

Another remarkable result in stripe ordered cuprates is the suppression or depression of superconductivity at $p \sim 1/8$, where the correlation lengths for stripe domains reach several tens of unit cells, suggesting a competition between HTS and stripes. The connection between static or fluctuating stripe domains and the cuprates phenomenology and Fermi surface reconstruction has been extensively discussed [142,143]. However, the presence of disorders in such a system further complicates the data interpretation.

In $YBa_2Cu_3O_{6+x}$ and related *123* compounds, doping-induced disorder is significantly reduced. In these cuprates, Nuclear magnetic resonance (NMR) experiments revealed a magnetic-field-induced modulation of the charge density for underdo-

ped compounds, without any signature of static magnetism [144,145].

Motivated by this experimental evidence, resonant [35,146,147] and non-resonant or integrated [148,149] x-ray scattering experiments on *123* underdoped cuprates demonstrated the presence of a charge density wave (CDW) order also in the absence of magnetic fields.

A deeper investigation of the temperature and magnetic field dependence of the revealed signal suggests a competition between charge-order state formation and superconductivity. The x-ray experiments also determined the periodicity of CDW, which is incommensurate with the underlying lattice.

More recent resonant x-ray scattering (RXS) measurements on a wide class of copper oxides probed that CDW correlations can be considered a generic feature for the undoped cuprates. In particular, charge-order has been found in $HgBa_2CuO_{4+\delta}$ [18], $Bi_2Sr_2CuO_{6+\delta}$ [150] and $Bi_2Sr_2CaCu_2O_{8+\delta}$ [36]. The results on Bi-based cuprates are also in good agreement with prior surface-sensitive scanning tunneling spectroscopy measurements [151,152]. CDW have been recently observed also in the electro-doped compound NCCO [127].

6.1.1 Charge modulations up to optimal doping

The data and the analyses shown in the following paragraphs have been published as part of "*Direct observation of bulk charge modulations in optimally-doped* $Bi_{1.5}Pb_{0.6}Sr_{1.54}CaCu_2O_{8+\delta}$" by M. Hashimoto, G. Ghiringhelli, W.-S. Lee, G. Dellea, A. Amorese, C. Mazzoli, K. Kummer, N. B. Brookes, B. Moritz, Y. Yoshida, H. Eisaki, Z. Hussain, T. P. Devereaux, Z.-X. Shen and L. Braicovich, Phys. Rev. B 89, 220511(R) (2014).

As anticipated in the introduction, RIXS allows a direct detection of charge ordering phenomena in cuprates. This is done considering the momentum transfer dependence of the elastic or quasi-elastic spectral features in diffraction-like experiment. When this experiment is performed in a RIXS spectrometer, chemical and element sensitivity is added. Compared to the non-energy-resolved resonant elastic x-ray scattering (REXS), RIXS provides a higher sensitivity, allowing to discriminate the true elastic or quasi-elastic signal given by charge ordering from the dominant inelastic contribution. The latter is indeed the main limiting factor in REXS providing a strong background.

Due to the finite experimental energy resolution, it was not possible to clearly

determine if the detected charge ordering peak was a truly elastic signal or a quasi-elastic contribution. For sake of clarity, we can refer to a generic modulation of the charge density residing in the CuO_2 planes as soft charge collective modes (soft-CCMs). The expression CCMs comprises both static charge density waves associated to zero energy loss, and dynamical charge modes having finite mass and thus related to a quasi-elastic peak.

First measurements performed with bulk sensitive techniques have observed soft-CCMs only in a narrow interval of the underdoped regime, close to the so-called plateau of the $T_c(p)$ phase diagram. Here we probed with RIXS that CCMs are also present in optimally doped $Bi_{1.5}Pb_{0.6}Sr_{1.54}CaCu_2O_{8+\delta}$ (Pb-Bi2212) single crystals, expanding the doping range in which superconductivity, pseudogap and tendency towards charge ordering coexist.

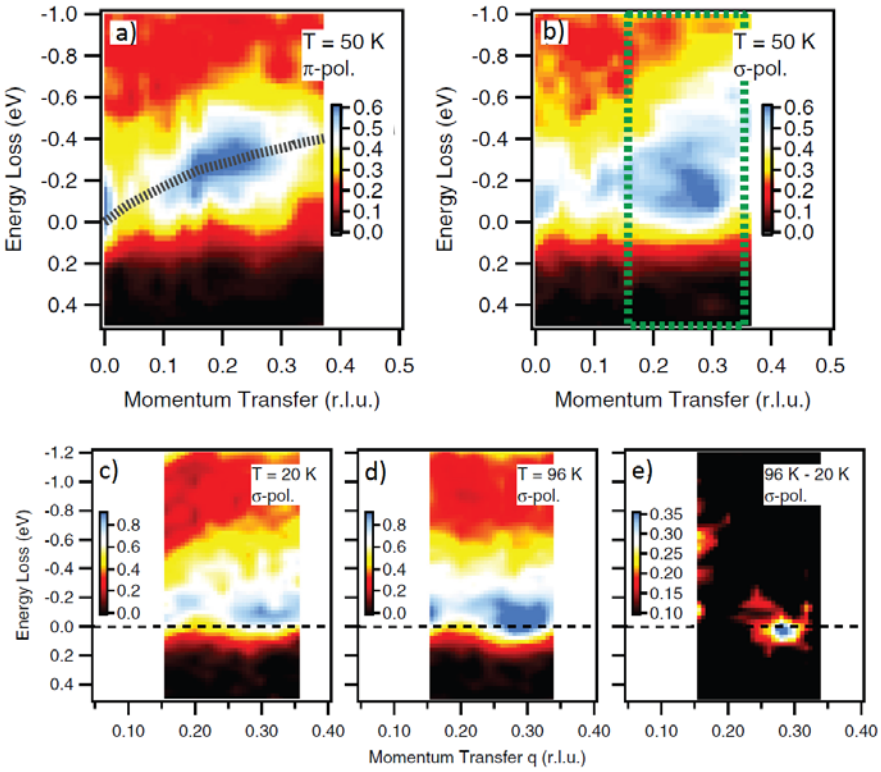

Fig. 6.1: Low-energy RIXS intensity maps (a-b) at T ~ 50 K along the Cu-O bond direction with π and σ polarizations, respectively. (c-e) Temperature dependent measurements with σ polarization in the momentum transfer region indicated by the green box in (b). Fig. reproduced from Ref. [36].

Cu-L_3 edge RIXS were performed at the AXES spectrometer of the ESRF with a combined resolution of 260 meV. The standard experimental geometry has been used and both spectra with π and σ incident polarization have been acquired, in order to exploit a polarization dependence analysis.

In Fig. 6.1 we show a summary of the most significant results. The RIXS map of Fig. 6.1(a), measured with π polarization, is dominated by single spin-flip excitations. These are paramagnons, as already observed by RIXS [14,17,82,90], and their dispersion is indicated by the dashed line that reaches the maximum energy of ∼ 350 meV at the zone boundary.

On the other hand the map of Fig. 6.1(b), measured with σ polarization, is mainly composed of non-spin-flip and double spin-flip processes (elastic scattering, charge excitations, phonons, and bimagnons) [31,34]. Around $\mathbf{q}_{\parallel} \sim 0.25$ r.l.u. we can identify a maximum in the intensity of the quasi-elastic feature. This type of signal, although weak, is similar to the soft-CCMs signature previously detected with RIXS in underdoped YBCO [35].

To better clarify the nature of this quasi-elastic signal, we performed temperature dependence, Fig. 6.1(c-e). The RIXS spectra maps at T = 96 K (∼ T_c) and T = 20 K (<< T_c), show and increased low energy intensity at $\mathbf{q}_{\parallel} \sim 0.28$ r.l.u. for the measurements performed close to the critical temperature, again in agreement with what observed on YBCO [35].

In conclusion, the peak of the quasi-elastic signal at $\mathbf{q}_{\parallel} \sim 0.28$ r.l.u. suggests the existence of soft-CCMs with a periodicity of ∼ 3.57 lattice units in the bulk state of optimally doped Bi2212, thus further extending the doping region in which CCMs have been observed.

More recent RIXS and REXS experiment confirmed the existence of charge modulations up to optimal doping in a wide class of cuprates, such as YBCO [153], NBCO, in Fig. 6.2(a), and LSCO, in Fig. 6.2(d).

Our more recent results on optimally doped NBCO and LSCO, acquired with a higher resolution, i.e. 120 meV, with the AXES spectrometer, also suggest a finite energy for CCMs peaks. This has strong implications in the understanding of the pseudogap phase. Indeed, if the pseudogap was connected to a broken translational symmetry, the soft CCMs would be truly static.

Unfortunately the quality of present data is still not good enough, mainly in terms of energy resolution and zero energy loss determination, to firmly draw conclusions regarding the quasi-elastic peak positions. New high-resolution RIXS spectrometers, such as ERIXS, would for sure allow important breakthroughs also

in the investigations of soft-CCMs.

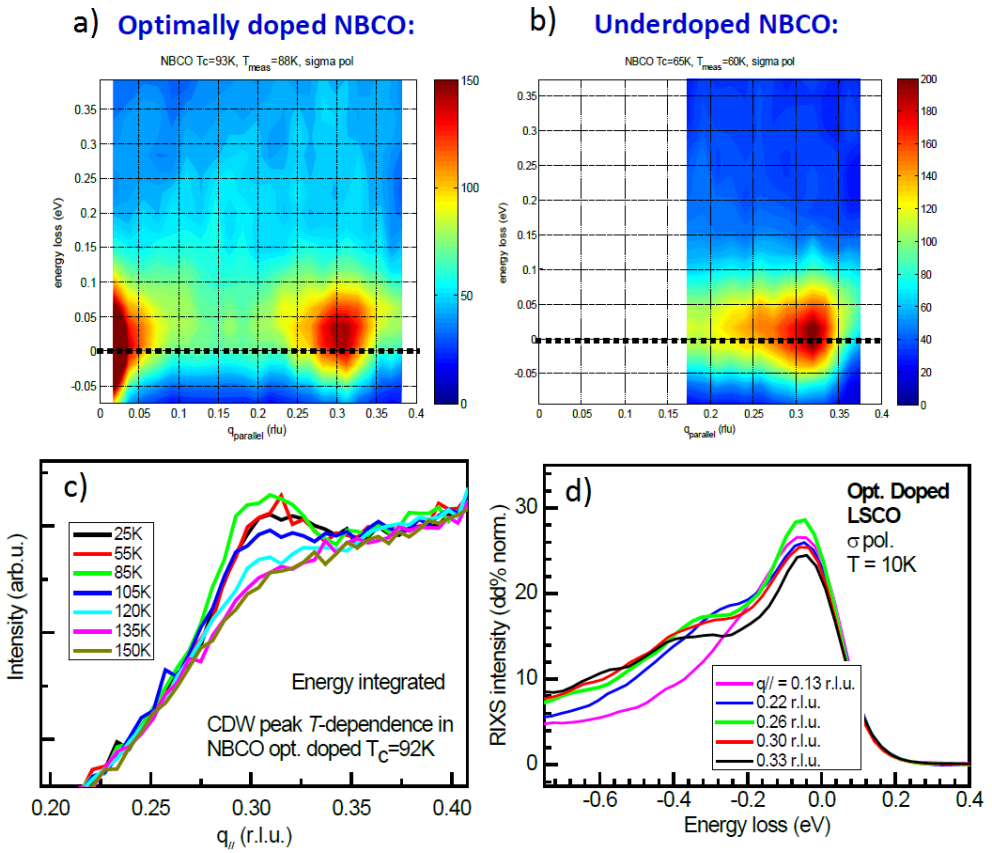

Fig. 6.2: (a-b) RIXS low energy scale maps with σ incident polarization for optimally (a) and under-doped NBCO, quasi-elastic peak is visible at $\mathbf{q}_{\parallel} \sim 0.26$ r.l.u.; (c) CCMs peak temperature dependence for optimally doped NBCO; a plateau more than a clear maximum is visible close to T_c; (d) RIXS spectra with σ incident polarization for optimally doped LSCO; fine tuning of $\mathbf{q}_{\parallel}$ in a range containing the CCMs peak.

It should be finally pointed out that the doping dependence of CCM incommensurability is also found to be in strong contrast with what found for *stripes* in the 214 cuprates [153], as shown in Fig. 6.3.

In conclusion, using resonant x-ray scattering (RXS) we have found evidence of bulk charge modulation in a wide class of optimally doped copper oxides: Bi2212, NBCO, LSCO and YBCO. These results demonstrate the presence of charge modula-

tions over a large region of the pseudogap regime, not constrained to the plateau of the $T_c(p)$ phase diagram but extending at least up to the optimal doping. Whether these charge modes are competing or cooperating with the superconductivity is still an unresolved issue.

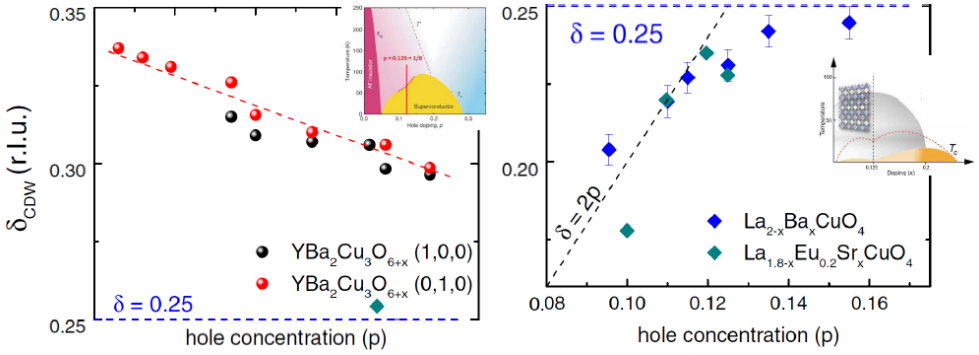

Fig. 6.3: Direct comparison between the CCM incommensurability doping dependence for 123 (left) and 214 (right) cuprates [153].

6.2 Phonons

The majority of RIXS studies on cuprates are focused on magnetic and charge excitations. Less is known regarding lattice excitations, i.e. phonons. This is mainly due to limitations in the energy resolution available in traditional RIXS spectrometers. The maximum phonons energies in cuprates are indeed close to 90 meV, and so difficult to be discerned from the elastic scattering.

The new ERIXS spectrometer has been shown to have the capability of investigating lattice excitations with bulk sensitivity. This has extremely important implications; if we consider that electron-phonon (e-ph) coupling has been suggested as a possible contribution to HTS in cuprates, either as a sole cause [154] or working in concomitance with magnetic excitations [155].

We remind that RIXS also provides the possibility to contemporary study phonons, magnetic and charge excitations; in that sense it is an extremely powerful tool in the search of possible competing or collaborating phenomena involving all the cuprates degrees of freedom.

6.2.1 Competing magnetic and phonon excitations

The data and the analyses shown in the following paragraphs have been published as part of "*Anomalous spectral dispersion of magnetic excitations in optimally doped* $Bi_{1.5}Pb_{0.55}Sr_{1.54}Ca_xCu_2O_{8+\delta}$" by Y. Y. Peng, M. Hashimoto, M. Moretti Sala, A. Amorese, N. B. Brookes, G. Dellea, W.-S. Lee, M. Minola, T. Schmitt, Y. Yoshida, K.-J. Zhou, H. Eisaki, T. P. Devereaux, Z.-X. Shen, L. Braicovich and G. Ghiringhelli, Phys. Rev. B 92, 064517 (2015).

In the following we present some recent RIXS data in which the interplay between magnetic, charge and lattice collective excitations is discussed.

In particular, we investigate in the optimally doped $Bi_{1.5}Pb_{0.55}Sr_{1.6}La_{0.4}CuO_{6+\delta}$ (OP-Bi2201, T_c =34 K).

RIXS measurements have been performed at the ADRESS beamline of the SLS with a combined energy resolution of 150 meV. Data have been collected at two temperatures T = 50, 200K, respectively below and above the pseudogap temperature. The standard experimental geometry has been used.

In Fig. 6.4 we show a summary of the experimental results.

RIXS spectra acquired with π incident polarization along the high symmetry direction (0,0)→(0.5,0) have been fitted in order to retrieve the paramagnon dispersion. In particular, the low energy scale of the spectra has been decomposed in four different contributions: (i) a resolution-limited Gaussian for the elastic peak, (ii) an antisymmetrized Lorentzian for the magnetic scattering, (iii) a smooth background for the particle-hole continuum and the tail of *dd*-excitations, and a resolution-limited Gaussian for the dominant optical phonon mode of ∼ 65 meV [156-158].

The paramagnon peak position determined in this way is shown in the maps of Fig. 6.4(a,b) as white squares. From the maps we note that the intensity of magnetic excitations shows a decrease above $\mathbf{q}_{\parallel}$ = 0.22 r.l.u. for both temperatures; meanwhile one new feature appears below 100 meV at the same momentum transfer. Remarkably, Fig. 6.4(c) depicts a paramagnon dispersion almost temperature independent, as expected.

The energy and the integrated intensity of paramagnons determined from the fitting procedure are compared in Fig. 6.4(c) and Fig. 6.4(d) for the two temperatures respectively. From theoretical predictions, we know that in an antiferromagnetic system the magnon intensity is expected to decrease to zero when approaching the Γ point [32,85].

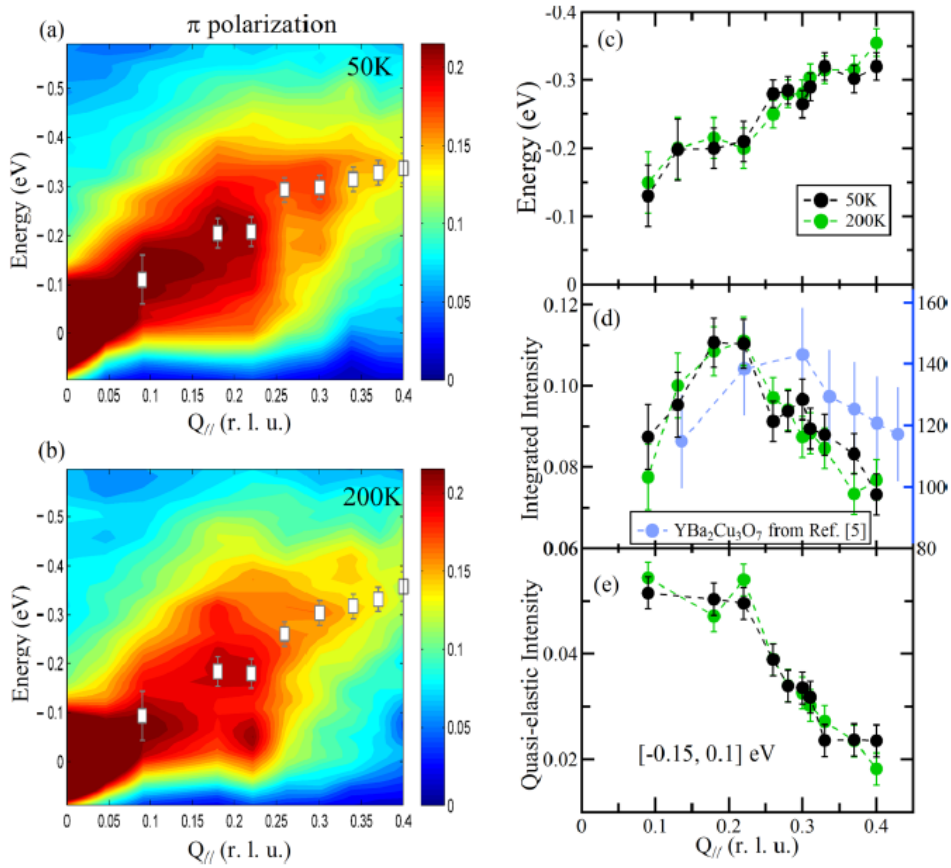

Fig. 6.4: Energy vs momentum intensity maps of RIXS spectra along the (0,0)→(0.5,0) symmetry direction, measured at (a) 50K and (b) 200K, with π incident polarization on OP-Bi2201. White solid squares indicate the paramagnon peak positions as determined fitting procedure. (c) Experimental paramagnon dispersion and (d) integrated intensity of paramagnon peak at 50 K (black) and 200 K (green) determined from the fitting procedure. Integrated inelastic intensity of optimally doped $YBa_2Cu_3O_7$ from Ref. [15] is superimposed for comparison (blue). (e) Intensity at [−0.15,0.1] eV energy window for quasi-elastic signal at 50 K (black) and 200 K (green). Self-absorption correction has been applied to (d) and (e). The error bars represent the uncertainty in the fittings. Fig. from [89].

Fig. 6.4(c) gives a similar behavior below 0.2 r.l.u. also for OP-Bi2201, although the paramagnon intensity could not be tracked below 0.1 r.l.u., due to the onset of the elastic peak that complicates the fitting procedure below 100 meV, also due to the finite experimental resolution.

More interestingly, the intensity of paramagnons also shows an abrupt drop above the already mentioned $\mathbf{q}_{\parallel}$ = 0.22 r.l.u. momentum transfer. In order to better investigate this phenomena, in Fig. 6.4(e) we plot the quasi-elastic intensity integrated over the [−0.15,0.1] eV energy window. A step, or alternatively a peak, in intensity is clearly visible at $\mathbf{q}_{\parallel}$ = 0.22 r.l.u.; for further increase of the momentum transfer the intensity is shown to decrease. We note that these considerations follow for both the temperatures investigated.

The observed drop in intensity above $\mathbf{q}_{\parallel}$ = 0.22 r.l.u. cannot be simply explained in terms of self-absorption. Moreover, the coincident intensity drop of paramagnon and quasi-elastic signal indicates the presence of a nontrivial effect.

We here notice that for optimally doped $YBa_2Cu_3O_7$, the integrated inelastic intensity shows an analogous decrease above 0.3 r.l.u. [17], which is the wave vector characterizing charge order [153] and bond-buckling phonon anomaly [159]. Therefore, charge order and phonon anomaly might play a role in our OP-Bi2201 too.

We finally also notice that around $\mathbf{q}_{\parallel}$ = 0.22 r.l.u., the paramagnon energy in Fig. 6.4(c) seems to deviate from a smooth dispersion.

If we now consider the low energy feature emerging below 100 meV at $\mathbf{q}_{\parallel}$ = 0.22 r.l.u. in the maps shown in Fig. 6.4(a-b), we can try to retrieve its nature. Charge order with a compatible characteristic wave vector has been observed in underdoped Bi2201 by REXS [150] and in OP-Bi2212 by RIXS [36]. However, the persistence of this feature up to 200 K, seems in contrast with the commonly observed temperature dependence of the charge order in hole-doped cuprates [35,150]. In order to have a better understanding of the phenomenology at play, we can thus investigate the dispersions maps acquired with incident σ polarization, shown in Fig. 6.5(a,b).

Following the discussion presented in session 4.2.1, we know that for positive $\mathbf{q}_{\parallel}$ the σ polarization enhances the non-spin-flip final states, including bimagnons, particle-hole pair generation and phonons; contrary, for negative $\mathbf{q}_{\parallel}$ the spin-flip and non-spin-flip excitations have similar intensity.

In our maps, we can unambiguously observe a peak below 100 meV at $\mathbf{q}_{\parallel}$ = +0.22 r.l.u.; this peak is stronger for σ polarization compared to π, as highlighted by the direct spectra comparison in Fig. 6.5(c). This clearly proves its non-spin-flip character. Moreover, its energy is fully compatible with a phonon excitation. This assignment is confirmed by data at negative $\mathbf{q}_{\parallel}$, where the phonon peak has an almost flat dispersion but its intensity increases beyond −0.25 r.l.u. wave vector.

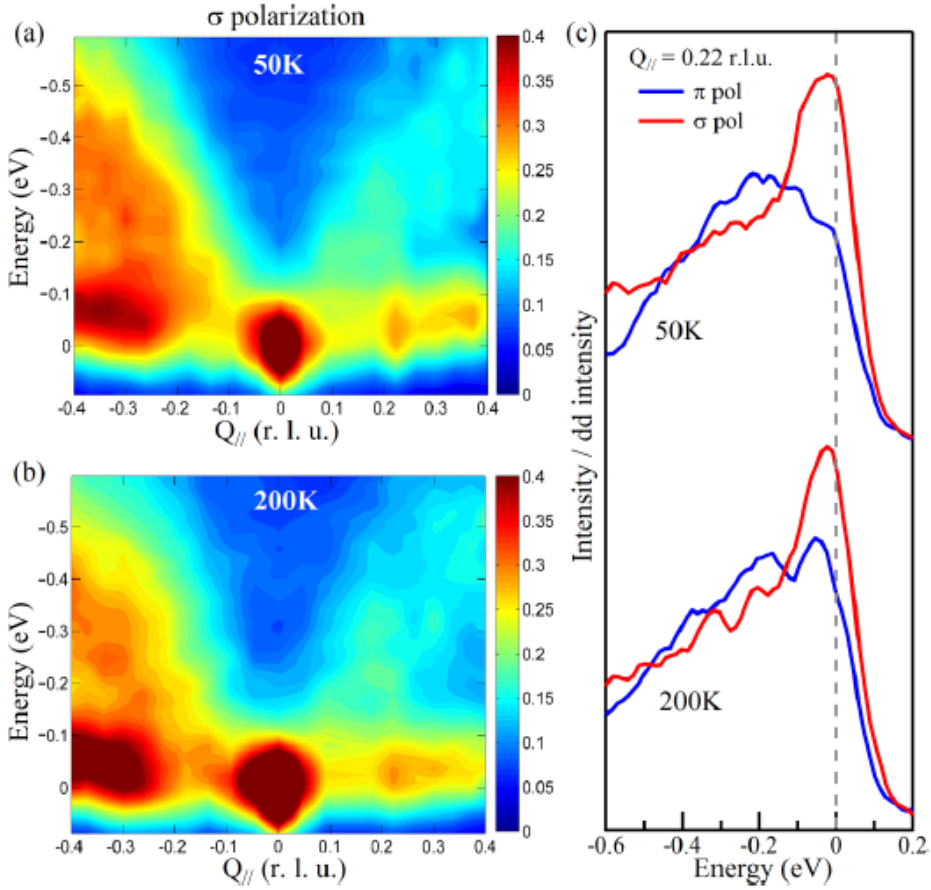

Fig. 6.5: Energy vs momentum intensity maps of RIXS spectra along the (−0.5,0)→(0.5,0) symmetry direction, measured at (a) 50 K and (b) 200 K, with σ incident polarization on OP-Bi2201. (c) Polarization comparison of RIXS spectra at $\mathbf{q}_{\parallel}$ = 0.22 r.l.u. for 50 K and 200 K [89].

Interestingly, inelastic x-ray scattering measurements on optimally doped $Bi_2Sr_{1.6}La_{0.4}CuO_{6+\delta}$ found a softening for the Cu-O bond stretching (BS) phonon and an anomalously broad line shape around 0.22 - 0.25 r.l.u. [157]. Phonon softening and broadening has been also observed around the charge ordering wave vector in several copper oxide superconductors [160,161], revealing the correlation between charge order and phonon anomalies.

In conclusion, we have proved by RIXS on OPBi2201 the coincidence of phonon and paramagnon intensity anomalies, which appears in correspondence of the putative charge-order wave-vector region.

Despite more systematic experiments, ideally with high resolution, full polarization analysis and enhanced control of sample orientation, are required to better understand the connections between charge, phonon and spin-flip excitations in cuprates; there is an increasing general evidence that spin excitations get coupled via the electron-phonon interaction, to both lattice modes and charge order, therefore providing a ubiquitous ingredient for superconductivity pairing mechanisms.

We thus conclude this Chapter and this thesis opening the way to new investigations of HTS in cuprates, in order to better clarify the proposed three-actor scenario, based on the competition and collaboration between spin excitations, electron-phonon coupling, and charge order.

Conclusions and Outlook

Within the context of the present thesis we have deeply exploited the capability of resonant inelastic x-ray scattering to investigate collective excitations in solids, mainly focusing on strongly correlated high-temperature superconducting cuprates.

RIXS at Cu-L_3 edge has been proved to be the perfect tool for exploring spin, charge and lattice excitations in the CuO_2 planes argued to retain the secret of unconventional superconductivity. Their magnetic excitations, in particular, persisting from the undoped antiferromagnetically ordered parent compounds up to the optimally doped samples, have been proposed to be a good candidate for driving Cooper Pairs formation. For this reason we invested many efforts in a deeper understanding of their properties.

After having firmly established the correct measurements conditions to have direct access to spin-flips, we experimentally confirmed their nature of collective excitations investigating the RIXS signal dependence on the incoming photons energy. The possibility of a crossover between optimal doping and high overdoping, corresponding to the transition from a collective-like excitation to a fluorescence-like feature, is also envisaged and it will be better clarified in future works.

The overdoped regime in particular has attracted our interest, being less inves-

tigated in the past. Surprisingly, high-energy magnetic excitations have been found persisting with dispersion and spectral weight closely similar to the ones observed in undoped samples up to very high dopings, also above the disappearance of the superconductivity phase. These observations suggest a more complex explanation for HTS, where magnetic excitations are just one of the actors at play.

The ubiquitous nature of the so called paramagnons has been subsequently confirmed by further measurements of magnetic excitations in a wide class of samples and dopings. In particular, we have proved magnetic excitations to be preserved by dimensionality effects down to one unit cell thick films and nanowires made of superconducting cuprates.

Another important piece of information in disclosing the nature of HTS is linked to the asymmetry between hole- and electron-doping. We have found differences in the behavior of both charge and magnetic excitations on both sides of the phase diagram. Electron-doped samples, in particular, show a hardening and a steeper dispersion of the magnetic excitations that are probed to get mixed with charge contributions; this has been argued to be linked to the more itinerant character, compared to the localized nature of spin excitations in holed-doped samples.

Compatible results have been also found in more exotic cuprates, such as superlattices and heterostructures. This opens the way to a new generations of HTS materials not constrained to the thermodynamical limitations governing the growth of crystals and films, and allowing to improve sample performances and explore new physics.

In conclusion, RIXS has been used to investigate other excitations, mainly focusing on the region of the spectra close to zero energy loss. Signatures of charge collective modes have been found in a wide class of cuprates and up to optimal doping; their contribution pro or against superconductivity is still not clear.

Phonon excitations competing and coexisting with charge and magnetic excitations have been also observed, opening the way to a new scenario in which superconductivity is tuned by the compresence of three different actors.

In conclusion, a lot have been done, but a clear explanation of HTS is still missing. In order to deepen explore the complex and fascinating world of cuprates; a further development in both instrumentation and theoretical understanding of the RIXS cross-section are thus required.

From the instrumental point of view, a new generation of soft-RIXS dedicated spectrometers is coming. The first of them is the ERIXS spectrometers, working since April 2015 at the new ID32 beamline of the European Synchrotron Radiation

Facility in Grenoble. In this thesis we have shown its new potentialities in terms of high-energy resolution, high count rate, sample control and analysis of the scattered polarization. All these features would for sure benefit the future investigations, allowing to complementary and contemporary perform analyses of the different excitations.

There are many possibilities for high resolution soft-RIXS future trends that we can think about. Hereafter we propose some of the most fascinating among them: (i) the systematic study of magnetic and *dd*- excitations in HTS cuprates with complete polarization control; (ii) the observation of charge and spin fluctuations exploiting the combination of diffractometer sample control capability and increased energy resolution; (iii) the systematic study of phonons coupling with magnetic, charge and vibrational excitations in cuprates; (iv) the study of medium- and low-energy excitations in new classes of samples, such as liquids, molecules, rare earth and 3*d* TM oxides.

Acknowledgments

There are several people that in a way or another shared with me these last three years and that I want to thank.

First of all, my gratitude goes to my professors Giacomo Ghiringhelli and Lucio Braicovich; I had the opportunity to appreciate them from both the scientific and the human point of view. Giacomo and Lucio represented a constant reference for me and I ought to them most that I know in physics. It was a pleasure sharing with them long days and nights of experiments and scientific discussions, and every time I was impressed by their competencies and their eclectic and complementary approaches that result in a fantastic mixture for working out solutions even when it seemed almost impossible. Finally, citing a student who made this path before me, "*thanks to Giacomo for bringing cookies at the beamline, and thanks to Lucio for helping us in eating them*"; good things never change.

Thanks to Dr. Nicholas Brookes, Nick, for guesting me at ID32 beamline for one year, and being my mentor during the time spent there, teaching me to never give up and make things working in the better way possible. Thanks to him and to the ID32 staff, Andrea, Flora, Kurt, Emilio, Erica and Andrea, for making my stay at the ESRF more than comfortable.

Thanks to Marco Salluzzo, Mathieu Le Tacon, Yinying Peng, Claudio Mazzoli,

Hlynur Gretarsson, Mark Dean, and all the other several coworkers and collaborators, with whom I shared pleasant beamtimes and sleepless night-shifts.

Thanks to all the friends that I met in Physics, thanks to Giulia for being always much more organized than me, thanks to Fabio for sharing the funniest teaching duties, thanks to Matteo and Marco for transferring to me the most important survival skills in data analysis, saving energies during never-ending beamtimes and, most important, choosing the right food at the ESRF canteen.

And thanks to my family and friends. My endless gratitude goes to my parents, Adolfo and Aurora, and to my brother Gabriele, who have been supporting my choices and believing in me since many years, being my safe place in the world.

And thanks to Fabrizio, who is so precious to me. Thanks for being always by my side in the last three years, in the funniest and the toughest days. Thanks for support and almost infinite patience. Thanks for "*supportarmi and sopportarmi"*.

And finally thanks to myself for not giving up, to Giovanni Rana and caffeine for providing me the "champions breakfast" after sleepless nights and to the Italian-French-Swiss rail services from being my second home for the last three years.

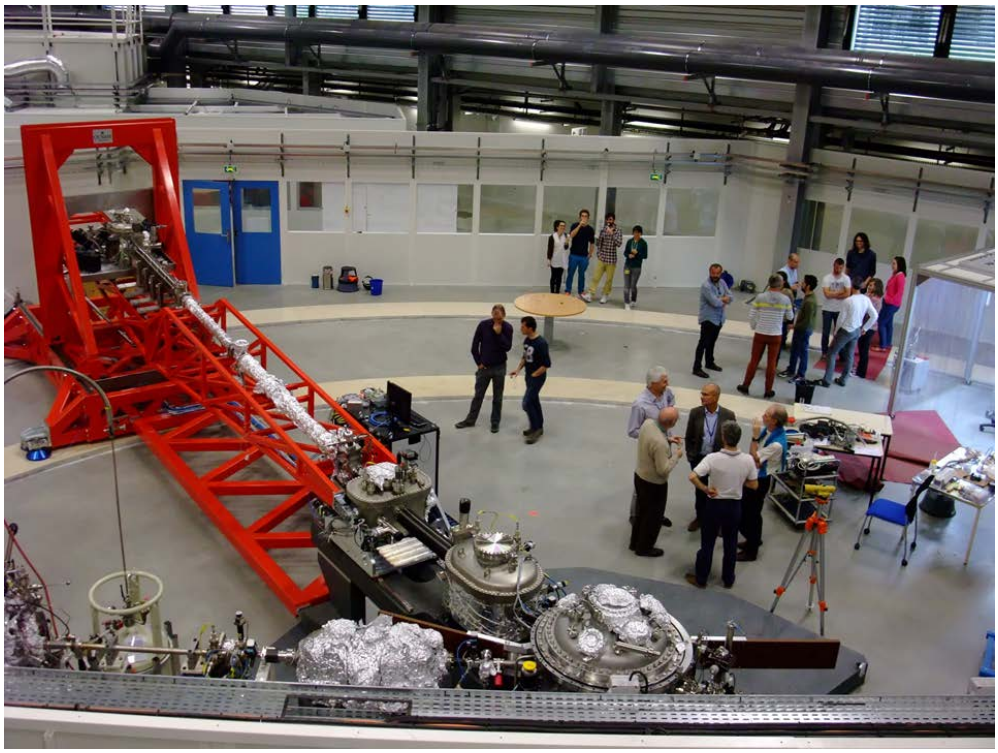

Inauguration of ERIXS spectrometer. Grenoble, 27.04.2015.

Bibliography

1. Sparks Jr, Cullie J. "Inelastic resonance emission of x rays: anomalous scattering associated with anomalous dispersion." *Physical Review Letters* 33.5 (1974): 262.
2. Kotani, Akio, and Shik Shin. "Resonant inelastic x-ray scattering spectra for electrons in solids." *Reviews of Modern Physics* 73.1 (2001): 203.
3. Bednorz, J. George, and K. Alex Müller. "Possible highT c superconductivity in the Ba-La-Cu-O system." *Zeitschrift für Physik B Condensed Matter* 64.2 (1986): 189-193.
4. De Boer, H. J., and E. J. W. Verwey. *Proc. Phys. Soc. London A* 49 (1937): 59.
5. Hubbard, John. "Electron correlations in narrow energy bands." *Proceedings of the Royal Society of London A: Mathematical, Physical and Engineering Sciences.* Vol. 276. No. 1365. The Royal Society, 1963.
6. Zaanen, J., G. A. Sawatzky, and J. W. Allen, “Band gaps and electronic structure of transition-metal compounds.” *Phys. Rev. Lett.* 55.4 (1985): 418–421.
7. Bardeen, John, Leon N. Cooper, and J. Robert Schrieffer. "Theory of superconductivity." *Physical Review* 108.5 (1957): 1175.
8. Coalition for the Commercial Application of Superconductors. http://www.ccas-web.org/pdf/ccas_brochure_web.pdf.

9. Dai, P., et al. "Synthesis and neutron powder diffraction study of the superconductor $HgBa_2Ca_2Cu_3O_{8+\delta}$ by Tl substitution." *Physica C: Superconductivity* 243.3 (1995): 201-206.
10. Kamihara, Yoichi, et al. "Iron-based layered superconductor: LaOFeP." *Journal of the American Chemical Society* 128.31 (2006): 10012-10013.
11. Kamihara, Yoichi, et al. "Iron-Based Layered Superconductor $La[O_{1-x}F_x]FeAs$ (x= 0.05-0.12) with T_c = 26 K." *Journal of the American Chemical Society* 130.11 (2008): 3296-3297.
12. Cava, Robert J. "Oxide superconductors." *Journal of the American Ceramic Society* 83.1 (2000): 5-28.
13. Minola, Matteo "Magnetic, orbital and charge fluctuations in layered cuprates studied by resonant soft x-ray scattering." *PhD thesis*, Politecnico di Milano, (2013).
14. Dean, M. P. M., et al. "Persistence of magnetic excitations in $La_{2-x}Sr_xCuO_4$ from the undoped insulator to the heavily overdoped non-superconducting metal." *Nature materials* 12.11 (2013): 1019-1023.
15. Tranquada, John M., et al. "Neutron scattering study of magnetic excitations in $YBa_2Cu_3O_{6+x}$." *Physical Review B* 40.7 (1989): 4503.
16. Dagotto, Elbio. "Correlated electrons in high-temperature superconductors." *Reviews of Modern Physics* 66.3 (1994): 763.
17. Le Tacon, Mathieu, et al. "Intense paramagnon excitations in a large family of high-temperature superconductors." *Nature Physics* 7.9 (2011): 725-730.
18. Tabis, W., et al. "Charge order and its connection with Fermi-liquid charge transport in a pristine high-T_c cuprate." *Nature communications* 5 (2014).
19. Fischer, Øystein, et al. "Scanning tunneling spectroscopy of high-temperature superconductors." *Reviews of Modern Physics* 79.1 (2007): 353.
20. Lee, Patrick A., Naoto Nagaosa, and Xiao-Gang Wen. "Doping a Mott insulator: Physics of high-temperature superconductivity." *Reviews of modern physics* 78.1 (2006): 17.
21. Norman, Michael R. "The challenge of unconventional superconductivity." *Science* 332.6026 (2011): 196-200.
22. Ament, Luuk JP, et al. "Resonant inelastic x-ray scattering studies of elementary excitations." *Reviews of Modern Physics* 83.2 (2011): 705.
23. Moretti Sala, Marco "Magnetic and orbital resonant inelastic soft x-ray scattering." *PhD thesis*, Politecnico di Milano, (2011).
24. Dean, M. P. M. "Insights into the high temperature superconducting cuprates from resonant inelastic X-ray scattering." *Journal of Magnetism and Magnetic Materials* 376 (2015): 3-13.

25. Grioni, M., et al. "Unoccupied electronic structure and core-hole effects in the x-ray-absorption spectra of Cu_2O." *Physical Review B* 45.7 (1992): 3309.
26. L. B. N. L. Center for X-Ray Optics, "X-ray interactions with matter." http://henke.lbl.gov/optical_constants/.
27. Shirane, Gen, Stephen M. Shapiro, and John M. Tranquada. *Neutron scattering with a triple-axis spectrometer: basic techniques*. Cambridge University Press, 2002.
28. Dean, M. P. M., et al. "Spin excitations in a single La_2CuO_4 layer." *Nature materials* 11.10 (2012): 850-854.
29. Headings, N. S., et al. "Anomalous high-energy spin excitations in the high-T_c superconductor-parent antiferromagnet La_2CuO_4." *Physical review letters* 105.24 (2010): 247001.
30. Lemmens, Peter, Gernot Güntherodt, and Claudius Gros. "Magnetic light scattering in low-dimensional quantum spin systems." *Physics Reports* 375.1 (2003): 1-103.
31. Moretti Sala, M., et al. "Energy and symmetry of dd excitations in undoped layered cuprates measured by Cu-L_3 resonant inelastic x-ray scattering." *New Journal of Physics* 13.4 (2011): 043026.
32. Ament, Luuk JP, et al. "Theoretical demonstration of how the dispersion of magnetic excitations in cuprate compounds can be determined using resonant inelastic X-ray scattering." *Physical review letters* 103.11 (2009): 117003.
33. Braicovich, L., et al. "Dispersion of magnetic excitations in the cuprate La_2CuO_4 and $CaCuO_2$ compounds measured using resonant x-ray scattering." *Physical review letters* 102.16 (2009): 167401.
34. Braicovich, L., et al. "Momentum and polarization dependence of single-magnon spectral weight for Cu L_3-edge resonant inelastic x-ray scattering from layered cuprates." *Physical Review B* 81.17 (2010): 174533.
35. Ghiringhelli, G., et al. "Long-range incommensurate charge fluctuations in (Y, Nd)$Ba_2Cu_3O_{6+x}$." *Science* 337.6096 (2012): 821-825.
36. Hashimoto, M., et al. "Direct observation of bulk charge modulations in optimally doped $Bi_{1.5}Pb_{0.6}Sr_{1.54}CaCu_2O_{8+\delta}$." *Physical Review B* 89.22 (2014): 220511.
37. Jia, C. J., et al. "Persistent spin excitations in doped antiferromagnets revealed by resonant inelastic light scattering." *Nature communications* 5 (2014).
38. Jia, Chunjing, et al. "Using RIXS to uncover elementary charge and spin exci-

tations in correlated materials." *arXiv preprint arXiv:1510.05068* (2015).

39. Ghiringhelli, G., et al. "Saxes, a high resolution spectrometer for resonant x-ray emission in the 400–1600ev energy range." *Review of scientific instruments* 77.11 (2006): 113108.
40. Strocov, V. N., et al. "High-resolution soft X-ray beamline ADRESS at the Swiss Light Source for resonant inelastic X-ray scattering and angle-resolved photoelectron spectroscopies." *Synchrotron Radiation* 17.5 (2010): 631-643.
41. Dallera, C., et al. "Soft x-ray emission spectroscopy at ESRF beamline 26 based on a helical undulator." *Journal of synchrotron radiation* 3.5 (1996): 231-238.
42. Dinardo, M. E., et al. "Gaining efficiency and resolution in soft X-ray emission spectrometers thanks to directly illuminated CCD detectors." *Nuclear Instruments and Methods in Physics Research Section A: Accelerators, Spectrometers, Detectors and Associated Equipment* 570.1 (2007): 176-181.
43. "ID32 - Soft X-ray spectroscopy". http://www.esrf.eu/UsersAndScience/Experiments/EMD/ID32.
44. "European Synchrotron Radiation Facility." http://www.esrf.eu.
45. Yakhou-Harris, F., K. Kummer, G. Berruyer, L. Braicovich, J. C. Cezar, F. Cianciosi, L. Eybert, P. Feder, A. Fondacaro, G. Ghiringhelli, E. Jimenez-Romero, M. Lemé, P. Marion, C. Ravary, L. Zhang, N.B. Brookes, "ID32 - The new ESRF soft X-ray beamline for spectroscopic studies with polarized light." *Poster contribution* (2015).
46. Sasaki, Shigemi, et al. "Design of a new type of planar undulator for generating variably polarized radiation." *Nuclear Instruments and Methods in Physics Research Section A: Accelerators, Spectrometers, Detectors and Associated Equipment* 331.1 (1993): 763-767.
47. Amorese, Andrea, et al. "Enhancing spatial resolution of soft x-ray CCD detectors by single-photon centroid determination." *arXiv preprint arXiv:1410.1587* (2014).
48. Hopkinson, G. R. "Charge diffusion effects in CCD x-ray detectors: I. Theory." *Nuclear Instruments and Methods in Physics Research* 216.3 (1983): 423-429.
49. Yakhou-Harris, F., K. Kummer, A. Amorese, G. Berruyer, F. Cianciosi, L. Eybert, A. Fondacaro, P. Feder, M. Lemé, E. Jimenez-Romero1,P. Marion, C. Ravary, P. van der Linden, E. Velez-Fort, N. B. Brookes, G. Dellea, Y. Y. Peng, L. Braicovich, G. Ghiringhelli, "ERIXS - The new high-resolution soft X-ray RIXS spectrometer at the ESRF beamline ID32." *Poster contribution* (2015).
50. "Cinel - Instruments for Research and Industry." http://www.cinel.com/.

51. Braicovich, L., et al. "The simultaneous measurement of energy and linear polarization of the scattered radiation in resonant inelastic soft x-ray scattering." *Review of Scientific Instruments* 85.11 (2014): 115104.
52. Hayden, S. M., et al. "High-frequency spin waves in $YBa_2Cu_3O_{6.15}$." *Physical Review B* 54.10 (1996): R6905.
53. Ghiringhelli, G., et al. "Resonant inelastic x-ray scattering of MnO: $L_{2,3}$ edge measurements and assessment of their interpretation." *Physical Review B* 73.3 (2006): 035111.
54. Ghiringhelli, G., et al. "Observation of Two Nondispersive Magnetic Excitations in NiO by Resonant Inelastic Soft-X-Ray Scattering." *Physical review letters* 102.2 (2009): 027401.
55. Dallera, C., et al. "Resonant soft-x-ray inelastic scattering from Gd in the $Gd_3Ga_5O_{12}$ garnet with excitation across the M_5 edge." *Physical Review B* 56.3 (1997): 1279.
56. Ishii, K., et al. "Polarization-analyzed resonant inelastic x-ray scattering of the orbital excitations in $KCuF_3$." *Physical Review B* 83.24 (2011): 241101.
57. Gao, Xuan, et al. "Development of a graphite polarization analyzer for resonant inelastic x-ray scattering." *Review of Scientific Instruments* 82.11 (2011): 113108.
58. Braicovich, L., et al. "Spectroscopy of strongly correlated systems: Resonant x-ray scattering without energy resolution in the scattered beam." *Physical Review B* 75.7 (2007): 073104.
59. Schäfers, Franz, et al. "Soft-x-ray polarimeter with multilayer optics: complete analysis of the polarization state of light." *Applied Optics* 38.19 (1999): 4074-4088.
60. Staub, U., et al. "Polarization analysis in soft X-ray diffraction to study magnetic and orbital ordering." *Journal of synchrotron radiation* 15.5 (2008): 469-476.
61. Beale, T. A. W., et al. "RASOR: An advanced instrument for soft x-ray reflectivity and diffraction." *Review of Scientific Instruments* 81.7 (2010): 073904.
62. Morawe, Ch, Ch Borel, and J-Ch Peffen. "The new ESRF multilayer deposition facility." *Optical Engineering+ Applications*. International Society for Optics and Photonics, 2007.
63. Morawe, C., et al. "Graded multilayers for fully polarization resolved resonant inelastic x-ray scattering in the soft x-ray range." *SPIE Optical Engineering+ Applications*. International Society for Optics and Photonics, 2014.
64. Abboud, A., et al. "Sub-pixel resolution of a pnCCD for X-ray white beam ap-

plications." *Journal of Instrumentation* 8.05 (2013): P05005.

65. Miyata, Emi, et al. "Mesh experiment for back-illuminated CCDs in improvement of position resolution." *Nuclear Instruments and Methods in Physics Research Section A: Accelerators, Spectrometers, Detectors and Associated Equipment* 513.1 (2003): 322-326.
66. Soman, M. R., et al. "Improving the spatial resolution of a soft X-ray Charge Coupled Device used for Resonant Inelastic X-ray Scattering." *Journal of Instrumentation* 6.11 (2011): C11021.
67. Hall, D. J., et al. "Improving the resolution in soft X-ray emission spectrometers through photon-counting using an Electron Multiplying CCD." *Journal of Instrumentation* 7.01 (2012): C01063.
68. Soman, M. R., et al. "Improving the spatial resolution of soft X-ray detection using an Electron-Multiplying Charge-Coupled Device." *Journal of instrumentation* 8.01 (2013): C01046.
69. Soman, M. R., et al. "Developing a CCD camera with high spatial resolution for RIXS in the soft X-ray range." *Nuclear Instruments and Methods in Physics Research Section A: Accelerators, Spectrometers, Detectors and Associated Equipment* 731 (2013): 47-52.
70. “Roper Scientific – Princeton Instruments.” http://www.roperscientific.com/.
71. Keimer, B., et al. "From quantum matter to high-temperature superconductivity in copper oxides." *Nature* 518.7538 (2015): 179-186.
72. Scalapino, Douglas J. "A common thread: The pairing interaction for unconventional superconductors." *Reviews of Modern Physics* 84.4 (2012): 1383.
73. Miyake, K., S. Schmitt-Rink, and C. M. Varma. "Spin-fluctuation-mediated even-parity pairing in heavy-fermion superconductors." *Physical Review B* 34.9 (1986): 6554.
74. Béal-Monod, M. T., C. Bourbonnais, and V. J. Emery. "Possible superconductivity in nearly antiferromagnetic itinerant fermion systems." *Physical Review B* 34.11 (1986): 7716.
75. Minola, M., et al. "Magnetic and ligand field properties of copper at the interfaces of (CaCuO 2) n/(SrTiO 3) n superlattices." *Physical Review B* 85.23 (2012): 235138.
76. Guarise, M., et al. "Measurement of magnetic excitations in the two-dimensional antiferromagnetic $Sr_2CuO_2Cl_2$ insulator using resonant X-ray scattering: evidence for extended interactions." *Physical review letters* 105.15 (2010): 157006.
77. Dean, M. P. M., et al. "High-energy magnetic excitations in the cuprate su-

perconductor $Bi_2Sr_2CaCu_2O_{8+\delta}$: towards a unified description of its electronic and magnetic degrees of freedom." *Physical review letters* 110.14 (2013): 147001.

78. Coldea, R., et al. "Spin waves and electronic interactions in La_2CuO_4." *Physical review letters* 86.23 (2001): 5377.
79. Headings, N. S., et al. "Anomalous high-energy spin excitations in the high-T_c superconductor-parent antiferromagnet La_2CuO_4." *Physical review letters* 105.24 (2010): 247001.
80. Bisogni, V., et al. "Bimagnon studies in cuprates with resonant inelastic x-ray scattering at the O-K edge. I. Assessment on La_2CuO_4 and comparison with the excitation at Cu-L_3 and Cu-K edges." *Physical Review B* 85.21 (2012): 214527.
81. Zhang, F. C., and T. M. Rice. "Effective Hamiltonian for the superconducting Cu oxides." *Physical Review B* 37.7 (1988): 3759.
82. Braicovich, L., et al. "Magnetic excitations and phase separation in the underdoped $La_{2-x}Sr_xCuO_4$ superconductor measured by resonant inelastic X-ray scattering." *Physical review letters* 104.7 (2010): 077002.
83. Dean, M. P. M., et al. "Magnetic excitations in stripe-ordered $La_{1.87}5Ba_{0.125}CuO_4$ studied using resonant inelastic x-ray scattering." *Physical Review B* 88.2 (2013): 020403.
84. Hinkov, V., et al. "Spin dynamics in the pseudogap state of a high-temperature superconductor." *Nature Physics* 3.11 (2007): 780-785.
85. Haverkort, M. W. "Theory of resonant inelastic X-ray scattering by collective magnetic excitations." *Physical review letters* 105.16 (2010): 167404.
86. Benjamin, David, Israel Klich, and Eugene Demler. "Single-Band Model of Resonant Inelastic X-Ray Scattering by Quasiparticles in High-T c Cuprate Superconductors." P*hysical review letters* 112.24 (2014): 247002.
87. Igarashi, Jun-ichi, and Tatsuya Nagao. "Magnetic excitations in L-edge resonant inelastic x-ray scattering from cuprate compounds." *Phys. Rev. B* 85, 064421 (2012).
88. Minola, M., et al. "Collective nature of spin excitations in superconducting cuprates probed by resonant inelastic x-ray scattering." *Physical Review Letters* 114.21 (2015): 217003.
89. Peng, Y. Y., et al. "Magnetic excitations and phonons simultaneously studied by resonant inelastic x-ray scattering in optimally doped $Bi_{1.5}Pb_{0.55}Sr_{1.6}La_{0.4}CuO_{6+\delta}$." *Phys. Rev. B* 92, 064517 (2015).
90. Le Tacon, M., et al. "Dispersive spin excitations in highly overdoped cuprates

revealed by resonant inelastic x-ray scattering." *Physical Review B* 88.2 (2013): 020501.

91. Ghiringhelli, G., and L. Braicovich. "Magnetic excitations of layered cuprates studied by RIXS at Cu-L_3 edge." *Journal of Electron Spectroscopy and Related Phenomena* 188 (2013): 26-31.
92. Braicovich, L., et al. "Towards full polarisation control in resonant inelastic soft X-ray scattering." *ESRF spotlight.* http://www.esrf.eu/news/spotlight/spotlight140/index_html.
93. Bourges, Ph, et al. "The spin excitation spectrum in superconducting $YBa_2Cu_3O_{6.85}$." *Science* 288.5469 (2000): 1234-1237.
94. Tranquada, J. M., et al. "Quantum magnetic excitations from stripes in copper oxide superconductors." *Nature* 429.6991 (2004): 534-538.
95. Hayden, S. M., et al. "The structure of the high-energy spin excitations in a high-transition-temperature superconductor." *Nature* 429.6991 (2004): 531-534.
96. Vignolle, B., et al. "Two energy scales in the spin excitations of the high-temperature superconductor $La_{2-x}Sr_xCuO_4$." *Nature Physics* 3.3 (2007): 163-167.
97. Xu, Guangyong, et al. "Testing the itinerancy of spin dynamics in superconducting $Bi_2Sr_2CaCu_2O_{8+\delta}$." *Nature Physics* 5.9 (2009): 642-646.
98. Wakimoto, S., et al. "Direct relation between the low-energy spin excitations and superconductivity of overdoped high-T_c superconductors." *Physical review letters* 92.21 (2004): 217004.
99. Wakimoto, S., et al. "Disappearance of antiferromagnetic spin excitations in overdoped $La_{2-x}Sr_xCuO_4$." *Physical review letters* 98.24 (2007): 247003.
100. Fujita, Masaki, et al. "Progress in neutron scattering studies of spin excitations in high-T_c cuprates." *Journal of the Physical Society of Japan* 81.1 (2011): 011007.
101. Keimer, Belk, et al. "Magnetic excitations in pure, lightly doped, and weakly metallic La_2CuO_4." *Physical Review B* 46.21 (1992): 14034.
102. Ghiringhelli, Giacomo, et al. "Low energy electronic excitations in the layered cuprates studied by copper L_3 resonant inelastic X-ray scattering." *Physical review letters* 92.11 (2004): 117406.
103. Wakimoto, S., et al. "High-energy magnetic excitations in overdoped $La_{2-x}Sr_xCuO_4$ studied by neutron and resonant inelastic x-ray scattering." *Physical Review B* 91.18 (2015): 184513.
104. Guarise, M., et al. "Anisotropic softening of magnetic excitations along the nodal direction in superconducting cuprates." *Nature communications* 5

(2014).
105. Dean, M. P. M., et al. "Itinerant effects and enhanced magnetic interactions in Bi-based multilayer cuprates." *Physical Review B* 90.22 (2014): 220506.
106. Emergent phenomena at oxide interfaces.
107. Gozar, A., and G. Logvenov. "Fitting Kourkoutis, L., Bollinger, AT, Giannuzzi, LA, Muller, DA, Bozovic, I." *Nature* 455 (2008): 782.
108. Bozovic, I., et al. "Epitaxial Strain and Superconductivity in $La_{2-x}Sr_xCuO_4$ Thin Films." *Physical review letters* 89.10 (2002): 107001.
109. Chakhalian, J., et al. "Orbital reconstruction and covalent bonding at an oxide interface." *Science* 318.5853 (2007): 1114-1117.
110. Minola, M., et al. "Measurement of the effect of lattice strain on magnetic interactions and orbital splitting in $CaCuO_2$ using resonant inelastic x-ray scattering." *Physical Review B* 87.8 (2013): 085124.
111. Arpaia, Riccardo, et al. "Improved nanopatterning for YBCO nanowires approaching the depairing current." *Applied Superconductivity, IEEE Transactions on* 23.3 (2013): 1101505-1101505.
112. Nawaz, Shahid, et al. "Microwave Response of Superconducting $YBa_2Cu_3O_{7-\delta}$ Nanowire Bridges Sustaining the Critical Depairing Current: Evidence of Josephson-like Behavior." *Physical review letters* 110.16 (2013): 167004.
113. Nawaz, Shahid, et al. "Approaching the theoretical depairing current in $YBa_2Cu_3O_{7-x}$ nanowires." *Physica C: Superconductivity* 495 (2013): 33-38.
114. Arpaia, Riccardo, et al. "Resistive state triggered by vortex entry in $YBa_2Cu_3O_{7-\delta}$ nanostructures." *Physica C: Superconductivity and its Applications* 506 (2014): 165-168.
115. Baghdadi, Reza, et al. "Fabricating Nanogaps in $YBa_2Cu_3O_{7-\delta}$ for Hybrid Proximity-Based Josephson Junctions." *Physical Review Applied* 4.1 (2015): 014022.
116. Kastner, M. A., et al. "Magnetic, transport, and optical properties of monolayer copper oxides." *Reviews of Modern Physics* 70.3 (1998): 897.
117. Takagi, H., S. Uchida, and Y. Tokura. "Superconductivity Produced by Electron Doping in CuO_2-Layered Compounds." *Ten Years of Superconductivity: 1980–1990*. Springer Netherlands, 1993. 274-277.
118. Yamada, K., et al. "Commensurate spin dynamics in the superconducting state of an electron-doped cuprate superconductor." *Physical review letters* 90.13 (2003): 137004.
119. Wilson, Stephen D., et al. "High Energy Spin Excitations in Electron-Doped Superconducting $Pr_{0.88}LaCe_{0.12}CuO_{4-\delta}$ with T_c = 21 K." *Phys. Rev. Lett.* 96,

157001 (2006).

120. Armitage, N. P., P. Fournier, and R. L. Greene. "Progress and perspectives on electron-doped cuprates." *Reviews of Modern Physics* 82.3 (2010): 2421.
121. Fujita, Masaki, et al. "Novel spin excitations in optimally electron-doped $Pr_{0.89}LaCe_{0.11}CuO_4$." *Journal of the Physical Society of Japan* 75.9 (2006): 093704.
122. Ishii, K., et al. "High-energy spin and charge excitations in electron-doped copper oxide superconductors." *Nature communications* 5 (2014).
123. Onose, Y., et al. "Charge dynamics in underdoped $Nd_{2-x}Ce_xCuO_4$: pseudogap and related phenomena." *Physical Review B* 69.2 (2004): 024504.
124. Ishii, K., et al. "Momentum dependence of charge excitations in the electron-doped superconductor $Nd_{1.85}Ce_{0.15}CuO_4$: a resonant inelastic x-ray scattering study." *Physical review letters* 94.20 (2005): 207003.
125. Jia, C. J., et al. "Uncovering selective excitations using the resonant profile of indirect inelastic x-ray scattering in correlated materials: observing two-magnon scattering and relation to the dynamical structure factor." *New Journal of Physics* 14.11 (2012): 113038.
126. Lee, W. S., et al. "Asymmetry of collective excitations in electron-and hole-doped cuprate superconductors." Nature Physics (2014).
127. da Silva Neto, Eduardo H., et al. "Charge ordering in the electron-doped superconductor $Nd_{2-x}Ce_xCuO_4$." *Science* 347.6219 (2015): 282-285.
128. Karimoto, Shin-ichi, et al. "Single-crystalline superconducting thin films of electron-doped infinite-layer compounds grown by molecular-beam epitaxy." *Applied Physics Letters* 79 (2001): 2767.
129. Tomaschko, Jochen, et al. "Properties of the electron-doped infinite-layer superconductor $Sr_{1-x}La_xCuO_2$ epitaxially grown by pulsed laser deposition." *Physical Review B* 85.2 (2012): 024519.
130. Balestrino, G., et al. "Dependence of the critical temperature on n in $(BaCuO_2)_2/(CaCuO_2)_n$ superlattices." *Physical Review B* 58.14 (1998): R8925.
131. Gozar, A., et al. "High-temperature interface superconductivity between metallic and insulating copper oxides." *Nature* 455.7214 (2008): 782-785.
132. Di Castro, D., et al. "Occurrence of a high-temperature superconducting phase in $(CaCuO_2)_n/(SrTiO_3)_m$ superlattices." *Physical Review B* 86.13 (2012): 134524.
133. Maritato, L., et al. "Layer-by-layer shuttered molecular-beam epitaxial growth of superconducting $Sr_{1-x}La_xCuO_2$ thin films." *Journal of applied physics* 113.5 (2013): 053911.
134. Harter, John W., et al. "Nodeless Superconducting Phase Arising from a

Strong (π, π) Antiferromagnetic Phase in the Infinite-Layer Electron-Doped $Sr_{1-x}La_xCuO_2$ Compound." *Physical review letters* 109.26 (2012): 267001.

135. Comin, Riccardo, and Andrea Damascelli. "Resonant x-ray scattering studies of charge order in cuprates." *arXiv preprint arXiv:1509.03313* (2015).
136. Tranquada, J. M., et al. "Evidence for stripe correlations of spins and holes in copper oxide superconductors." *Nature* 375.6532 (1995): 561-563.
137. Fink, Jörg, et al. "Charge ordering in $La_{1.8-x}Eu_{0.2}Sr_xCuO_4$ studied by resonant soft X-ray diffraction." *Physical Review B* 79.10 (2009): 100502.
138. Fink, Jörg, et al. "Phase diagram of charge order in $La_{1.8-x}Eu_{0.2}Sr_xCuO_4$ from resonant soft x-ray diffraction." *Physical Review B* 83.9 (2011): 092503.
139. Hücker, M., et al. "Stripe order in superconducting $La_{2-x}Ba_xCuO_4$ (0. 095⩽ x⩽ 0. 155)." *Physical Review B* 83.10 (2011): 104506.
140. Hücker, M., et al. "Enhanced charge stripe order of superconducting $La_{2-x}Ba_xCuO_4$ in a magnetic field." *Physical Review B* 87.1 (2013): 014501.
141. Wilkins, S. B., et al. "Comparison of stripe modulations in $La_{1.875}Ba_{0.125}CuO_4$ and $La_{1.48}Nd_{0.4}Sr_{0.12}CuO_4$." *Physical Review B* 84.19 (2011): 195101.
142. Kivelson, Steven A., et al. "How to detect fluctuating stripes in the high-temperature superconductors." *Reviews of Modern Physics* 75.4 (2003): 1201.
143. Vojta, Matthias. "Lattice symmetry breaking in cuprate superconductors: stripes, nematics, and superconductivity." *Advances in Physics* 58.6 (2009): 699-820.
144. Wu, Tao, et al. "Emergence of charge order from the vortex state of a high-temperature superconductor." *Nature communications* 4 (2013).
145. Wu, Tao, et al. "Magnetic-field-induced charge-stripe order in the high-temperature superconductor $YBa_2Cu_3O_y$." *Nature* 477.7363 (2011): 191-194.
146. Achkar, A. J., et al. "Distinct charge orders in the planes and chains of ortho-III-ordered $YBa_2Cu_3O_{6+\delta}$ superconductors identified by resonant elastic x-ray scattering." *Physical review letters* 109.16 (2012): 167001.
147. Blanco-Canosa, S., et al. "Momentum-dependent charge correlations in $YBa_2Cu_3O_{6+\delta}$ superconductors probed by resonant X-ray scattering: Evidence for three competing phases." *Physical review letters* 110.18 (2013): 187001.
148. Chang, J., et al. "Direct observation of competition between superconductivity and charge density wave order in $YBa_2Cu_3O_6$. 67." *Nature Physics* 8.12 (2012): 871-876.
149. Blackburn, E., et al. "X-ray diffraction observations of a charge-density-wave order in superconducting ortho-II $YBa_2Cu_3O_{6.54}$ single crystals in zero mag-

netic field." *Physical review letters* 110.13 (2013): 137004.

150. Comin, R., et al. "Charge order driven by Fermi-arc instability in $Bi_2Sr_{2-x}La_xCuO_{6+\delta}$." *Science* 343.6169 (2014): 390-392.
151. Hoffman, J. E., et al. "A four unit cell periodic pattern of quasi-particle states surrounding vortex cores in $Bi_2Sr_2CaCu_2O_{8+\delta}$." *Science* 295.5554 (2002): 466-469.
152. Lawler, M. J., et al. "Intra-unit-cell electronic nematicity of the high-T_c copper-oxide pseudogap states." *Nature* 466.7304 (2010): 347-351.
153. Blanco-Canosa, S., et al. "Resonant x-ray scattering study of charge-density wave correlations in $YBa_2Cu_3O_{6+x}$." *Physical Review B* 90.5 (2014): 054513.
154. Lanzara, A., et al. "Evidence for ubiquitous strong electron–phonon coupling in high-temperature superconductors." *Nature* 412.6846 (2001): 510-514.
155. Johnston, S., et al. "Systematic study of electron-phonon coupling to oxygen modes across the cuprates." *Physical Review B* 82.6 (2010): 064513.
156. Sugai, S., et al. "Carrier-density-dependent momentum shift of the coherent peak and the LO phonon mode in p-type high-T_c superconductors." *Physical Review B* 68.18 (2003): 184504.
157. Graf, Jeff, et al. "Bond stretching phonon softening and kinks in the angle-resolved photoemission spectra of optimally doped $Bi_2Sr_{1.6}La_{0.4}Cu_2O_{6+\delta}$ superconductors." *Physical Review Letters* 100.22 (2008): 227002.
158. Ying-Ying, Peng, et al. "Doping Evolution of Nodal Band Renormalization in $Bi_2Sr_2CuO_{6+\delta}$ Superconductor Revealed by Laser-Based Angle-Resolved Photoemission Spectroscopy." *Chinese Physics Letters* 30.6 (2013): 067402.
159. Reznik, D. "Phonon anomalies and dynamic stripes." *Physica C: Superconductivity* 481 (2012): 75-92.
160. Le Tacon, M., et al. "Inelastic X-ray scattering in $YBa_2Cu_3O_{6.6}$ reveals giant phonon anomalies and elastic central peak due to charge-density-wave formation." *Nature Physics* 10.1 (2014): 52-58.
161. Blackburn, Elizabeth, et al. "Inelastic x-ray study of phonon broadening and charge-density wave formation in ortho-II-ordered $YBa_2Cu_3O_{6.54}$." *Physical Review B* 88.5 (2013): 054506.

Publications list

1. **M. P. M. Dean**, G. Dellea, M. Minola, S. B. Wilkins, R. M. Konik, G. D. Gu, M. Le Tacon, N. B. Brookes, F. Yakhou-Harris, K. Kummer, J. P. Hill, L. Braicovich and G. Ghiringhelli, "*Magnetic excitations in stripe-ordered $La_{1.875}Ba_{0.125}CuO_4$ studied using resonant inelastic x-ray scattering",* ***Phys. Rev. B*** **88, 020403(R) (2013)**.

2. **M. P. M. Dean**, G. Dellea, R. S. Springell, F. Yakhou-Harris, K. Kummer, N. B. Brookes, X. Liu, Y-J. Sun, J. Strle, T. Schmitt, L. Braicovich, G. Ghiringhelli, I. Božović and J. P. Hill, **"***Persistence of magnetic excitations in $La_{2-x}Sr_xCuO_4$ from the undoped insulator to the heavily overdoped non-superconducting metal",* ***Nature Materials*** **12, 1019-1023 (2013)**.

3. **M. Le Tacon**, A. Bosak, S. M. Souliou, G. Dellea, T. Loew, R.Heid, K.-P. Bohnen, G. Ghiringhelli, M. Krisch and B. Keimer, "*Inelastic X-ray scattering in $YBa_2Cu_3O6.6$ reveals giant phonon anomalies and elastic central peak due to charge-density-wave formation",* ***Nature Physics*** **10, 52-58 (2014)**.

4. **K. Ishii**, M. Fujita, T. Sasaki, M. Minola, G. Dellea, C. Mazzoli, K. Kummer, G. Ghiringhelli, L. Braicovich, T. Tohyama, K. Tsutsumi, K. Sato, R. Kajimoto, K. Ikeuchi, K. Yamada, M. Yoshida, M. Kurooka and J. Mizuki, *"High-energy spin and charge excitations in electron-doped copper oxide superconductors"*, ***Nat. Commun.*** **5:3714 (2014).**

5. **M. Hashimoto**, G. Ghiringhelli, W.-S. Lee, G. Dellea, A. Amorese, C. Mazzoli, K. Kummer, N. B. Brookes, B. Moritz, Y. Yoshida, H. Eisaki, Z. Hussain, T. P. Devereaux, Z.-X. Shen and L. Braicovich, "*Direct observation of bulk charge modulations in optimally-doped* $Bi_{1.5}Pb_{0.6}Sr_{1.54}CaCu_2O_{8+\delta}$*"*, ***Phys. Rev. B*** **89, 220511(R) (2014)**.

6. **L. Braicovich**, M. Minola, G. Dellea, M. Le Tacon, M. Moretti Sala, C. Morawe, J-Ch. Peffen, R. Supruangnet, F. Yakhou, G. Ghiringhelli and N. B. Brookes, *"The simultaneous measurement of energy and linear polarization of the scattered radiation in resonant inelastic soft x-ray scattering"*, ***Rev. Sci. Instrum.*** **85, 115104 (2014).**

7. **W. Tabis**, Y. Li, M. Le Tacon, L. Braicovich, A. Kreyssig, M. Minola, G. Dellea, E. Weschke, M. J. Veit, M. Ramazanoglu, A. I. Goldman, T. Schmitt, G. Ghiringhelli, N. Barišić, M. K. Chan, C. J. Dorow, G. Yu, X. Zhao, B. Keimer, M. Greven, "*Charge order and its connection with Fermi-liquid charge transport in a pristine high-*T_c *cuprate"*, ***Nat. Commun.*** **5:5875 (2014).**

8. **A. Amorese**, G. Dellea, L. Braicovich and G. Ghiringhelli, *"Enhancing spatial resolution of soft x-ray CCD detectors by single-photon centroid determination"*, ***arXiv:*****1410.1587** ***(2014)***.

9. **M. Minola**, G. Dellea, H. Gretarsson, Y. Y. Peng, Y. Lu, J. Porras, T. Loew, F. Yakhou, N. B. Brookes, Y. Huang, J. Pelliciari, T. Schmitt, G. Ghiringhelli, B. Keimer, L. Braicovich and M. Le Tacon, *"Collective nature of spin excitations in superconducting cuprates probed by resonant inelastic x-ray scattering"*, ***Phys. Rev. Lett.*** **114, 217003 (2015).**

10. **S. Wakimoto**, K. Ishii, H. Kimura, M. Fujita, G. Dellea, K. Kummer, L. Braicovich, G. Ghiringhelli, L. M. Debeer-Schmitt and G. E. Granroth, *"High energy magnetic excitations in overdoped $La_{2-x}Sr_xCuO_4$ studied by neutron and resonant inelastic x-ray scattering"*, ***Phys. Rev. B* 91, 184513 (2015).**

11. **Y. Y. Peng**, M. Hashimoto, M. Moretti Sala, A. Amorese, N. B. Brookes, G. Dellea, W.-S. Lee, M. Minola, T. Schmitt, Y. Yoshida, K.-J. Zhou, H. Eisaki, T. P. Devereaux, Z.-X. Shen, L. Braicovich and G. Ghiringhelli, *"Anomalous spectral dispersion of magnetic excitations in optimally doped $Bi_{1.5}Pb_{0.55}Sr_{1.54}Ca_xCu_2O_{8+\delta}$"*, ***Phys. Rev. B* 92, 064517 (2015)**.

12. **G. Dellea**, M. Minola, C. Mazzoli, L. Braicovich,L. Maritato, A. Galdi, P. Orgiani, D. G. Schlom, D. Di Castro, A. Tebano, G. Balestrino, C. Aruta, M. Moretti Sala, N. B. Brookes, C. J. Jia, B. Moritz, T. P. Devereaux and G. Ghiringhelli, *"Charge and magnetic excitations in hole- and electron-doped infinite layer cuprate superconductors",* ***in preparation (2015).***